NORTH CASPIAN BASIN:
2D ELASTIC MODELING
FOR SEISMIC IMAGING OF SALT AND SUBSALT

A Thesis

by

ZHANAR ALPYSBAEVNA BAILEY

Submitted to the Office of Graduate Studies of
Texas A&M University
in partial fulfillment of the requirements for the degree of

MASTER OF SCIENCE

December 2004

Major Subject: Geophysics

NORTH CASPIAN BASIN:
2D ELASTIC MODELING
FOR SEISMIC IMAGING OF SALT AND SUBSALT

A Thesis

by

ZHANAR ALPYSBAEVNA BAILEY

Submitted to Texas A&M University
in partial fulfillment of the requirements
for the degree of

MASTER OF SCIENCE

Approved as to style and content by:

Luc T. Ikelle
(Chair of Committee)

Hongbin Zhan
(Member)

Daulat D. Mamora
(Member)

Richard L. Carlson
(Head of Department)

December 2004

Major Subject: Geophysics

ABSTRACT

North Caspian Basin: 2D Elastic Modeling for Seismic Imaging
of Salt and Subsalt. (December 2004)
Zhanar Alpysbaevna Bailey,
Diploma, Kazakh National Technical University
Chair of Advisory Committee: Dr. Luc T. Ikelle

The North Caspian Basin (NCB) contains a significant number of major oil fields, some of which are yet to be put into production. The reason why some of these fields are not yet put into production is the exploration challenge that the NCB poses. In particular, the complex geological structure of this region makes it quite difficult to image its oil fields with conventional seismic techniques. This thesis sheds more light on difficulties associated with acquiring and processing seismic data in the NCB. The two central tools for investigation of these imaging challenges were the construction of a geological model of the NCB and the use of an accurate elastic wave-propagation technique to analyze the capability of seismic to illuminate the geological structures of the NCB. Using all available regional and local studies and my knowledge gained with oil companies, where I worked on subsalt and suprasalt 2D and 3D seismic data from the North Caspian Basin, I constructed a 2D elastic isotropic 10-by-6 km geological model of a typical oil field located on the shelf of the Caspian Sea in the southeastern part of the North Caspian Basin, which has the largest oil fields. We have propagated seismic waves through this model. The technique we used to compute wave propagation is known as the Finite-Difference Modeling (FDM) technique. Generating 314 shot gathers with stationary multicomponent OBS receivers that were spread over 10 km took two weeks of CPU time using two parallel computers (8 CPU V880 Sun Microsystems and 24 CPU Sun Enterprise). We have made the data available to the public. The dataset can be uploaded at http://casp.tamu.edu in the SEGY format. The key conclusions of the analysis of these data are as follows:

- Combined usage of P- and S-waves allows us to illuminate subsalt reef, clastics and complex salt structures despite the 4-km overburden.
- Free-surface multiples and guided waves are one of the key processing challenges in NCB, despite relatively shallow (less than 15 m) shelf water.

ACKNOWLEDGMENTS

I thank Dr. Luc Ikelle for his teaching. His progressive thought, ingenuity, and creative energy inspired this work.

I also would like to express my gratitude to my committee members, Dr. Hongbin Zhan and Dr. Daulat Mamora, for their insightful comments and support.

I am thankful also to all former and current CASP members, who provided technical support and fond memories, as well as the sponsors of the CASP project that made this and other research possible.

TABLE OF CONTENTS

Page

ABSTRACT iii

ACKNOWLEDGMENTS v

TABLE OF CONTENTS vi

LIST OF FIGURES viii

LIST OF TABLES xiv

CHAPTER

I INTRODUCTION 1

II CONSTRUCTING THE GEOLOGICAL MODEL 9

- Geological structures 9
- Elastic properties of rocks 19

III FINITE-DIFFERENCE MODELING 34

- Equations for wave propagation in elastic media 34
- Discretization of equations of wave propagation on a staggered grid . 35
- Stability condition 38
- Grid dispersion 38
- Boundary conditions 39
- Discretization of the geological model 40
- Parameters of seismic acquisition 40

IV ANALYSIS OF RAW DATA 44

- Dataset 44
- Definition of key reflectors 44
- Quality of imaging of subsalt targets 46
    - The effect of the overburden 46
    - Guided waves 64
    - Multiple waves 67
    - Turning waves 67
    - Multicomponent waves 77

CHAPTER Page

V CONCLUSIONS 95

REFERENCES 100

VITA 103

LIST OF FIGURES

FIGURE Page

1 The location of the North Caspian Basin and its southeastern part (modified from UT Libraries, 2004)…..……………………...….……......1

2 Satellite image of the Caspian Sea region. (NASA, 2004)……..…….…….…2

3 The North Caspian Basin from space. (NASA, 2004) ...………………......3

4 The North Caspian Sea is frozen 6 months a year. (NASA, 2004) …..……3

5 Seismic depth section of the eastern slope of the Tengiz paleoatoll (part of seismic line #669). (Pavlov, 1988)………………………..…….…...12

6 Seismic depth section of the western slope of the Tengiz paleoatoll (part of seismic line #669). (Pavlov, 1988)……………….………...…....13

7 Map of salt structures of the North Caspian Basin (onshore only). (modified from Volozh et al. 1989). The green zone represents salt domes and diapirs with overhangs ..……………….………………….….…14

8 Cross-section from the seismic profile in the Fugure 7. (modified from Volozh et al. 1989)…………..……………………..…16

9 East-west cross section towards the center of NCB. (modified from Volozh et al. 2003) ………...……..……..…………..…..16

10 Post Stack Depth Migration results from the NCB (modified from Barde et al. 2002)…………………..……………….……17

11 2D geological model of the southeastern North Caspian Basin………..….18

12 Distribution of shear wave velocities in the geological model……………30

13 Distribution of compressional wave velocities in the geological model….30

14 Distribution of shear modulus in the geological model.……………….……31

FIGURE Page

15 Distribution of densities in the geological model..……...…..……..……. 31

16 Distribution of [λ + 2μ] in the geological model……………….…..……32

17 Distribution of compressional wave impedance in the geological model.. 32

18 Distribution of shear wave impedance in the geological model ..…….….…33

19 Distribution of bulk modulus in the geological model……..……...…. …33

20 Illustration of the staggered grid technique (Ikelle and Amundsen, 2004)……………………………………………………………..……...36

21 Finite-difference method allows us to see the propagation of waves in the subsurface ………………………………………………………43

22 A geomodel showing geological ages of formations. Black continuous arrows indicate tops of a subsalt reservoir; dark blue arrows indicate near salt possible oil and gas accumulations; black dashed arrows indicate possible suprasalt accumulations of hydrocarbons. E – salt dome, M and B are salt diapirs, A – anhydrites ..……….….……45

23 Snapshot of shot #11. We have enough energy to reach the carbonate reservoir and beyond despite the fact that the reservoir is under a salt dome……………………………………………………………….....48

24 Snapshot of the shot #136 showing that we have enough energy to reach the subsalt except under anhydrites when the wavefront has to propagate, first, through the diapir, second, through anhydrites to reach the target reflector…………………………………………..…....49

25 Snapshot of shot #151 demonstrates that we have enough energy to reach subsalt reservoirs everywhere except under the anhydrites when the wavefront has to propagate, first, through diapir, second, through anhydrites to reach the target reflector. ……………………..…..50

26 Snapshot of shot #222 demonstrates that we have enough energy to reach subsalt reservoirs everywhere, even under the anhydrite, because this time the wave propagates through clastics, not a salt diapir, to reach anhydrites. ………………………………………………51

FIGURE Page

27 Snapshot of shot #282 demonstrates that we have enough energy to reach subsalt reservoirs everywhere, even under anhydrite, because this time the wave propagates through clastics, not a salt diapir, to reach anhydrites. ……………………………………..52

28 Shot 001, pressure. Exp. Gain, AGC=90. Reflections from top P1a2 and C2-D3 target formations are indicated………………………………..53

29 Shot 081, pressure. Exp. Gain, AGC=90. Reflections from top P1a2 and C2-D3 target formations are indicated..…………………….……..…54

30 Shot 121, pressure. Exp. Gain, AGC=90. We can see only one target horizon P1a2……………………………………………………….…….…......55

31 Shot 161, pressure. Exp. Gain, AGC=90. Only P1a2 target horizon is visible. ………………………………………………………………….…56

32 Shot 222, pressure. Exp. Gain, AGC=90. Our target reflectors P1a2 and C2-D3 are not seen well on the shot gathers from the right half of our model (shots 150 through 314). ……………………………...……57

33 Shot 241, pressure. Exp. Gain, AGC=90. Our target reflectors P1a2 and C2-D3 are not seen well on the shot gathers from the right half of our model (shots 150 through 314). …………………………...…….58

34 Shot 281, pressure. Exp. Gain, AGC=90. Our target reflectors P1a2 and C2-D3 are not seen well on the shot gathers from the right half of our model (shots 150 through 314)……………………………….……59

35 Shot 301, pressure. Exp. Gain, AGC=90. Our target reflectors P1a2 and C2-D3 are not seen well on the shot gathers from the right half of our model (shots 150 through 314)…………………………………..…60

36 Snapshot where reflected P and S waves from top P1a2 clastics display relative conformity with the reflector shape…………………...…61

37 Snapshot demonstrating P-wave wavefront distortion of P1a2 reflection in salt. We do not see S-wave reflection. ……….……………..62

FIGURE Page

38 Snapshot showing top P1a2 clastics P-wave reflection. There is no S-wave P1a2 reflection……………………………………….…63

39 Shot 001, pressure, AGC=99. The extent and intensity of guided waves obstructing useful reflections. Compare with the figure 40, where guided waves were removed.…………………...……………..…65

40 Shot 001, pressure, absorbing free surface, AGC=99. Guided waves are removed……………………….……….…….…….……66

41 Shot 001, pressure. Exp. Gain, AGC=90. Shot gather with free surface and near surface multiples of target reflectors P1a2 and C2-D3……………………………………………………...….…68

42 Shot 001, pressure. Exp. Gain, AGC=90. Shot gather with removed free surface and near surface multiples of target reflectors P1a2 and C2-D3…………………………………………..….69

43 Shot 081, pressure. Exp. Gain, AGC=90. Shot gather with free and near surface multiples………………………………...……………...70

44 Shot 081, pressure. Exp. Gain, AGC=90. Shot gather without free surface and near surface multiples. Notice how much easier it is to see target reflectors P1a2 and C2-D3……………….…………….....71

45 Shot 121, pressure. Exp. Gain, AGC=90. Shot gather with free surface and near surface multiples. ……………………………………..…72

46 Shot 121, pressure. Exp. Gain, AGC=90. Shot gather with removed free surface near surface multiples. ……………………………...…73

47 Snapshot at timestep 85. Free surface multiples interfering with reflections from target reflectors P1a2 and C2-D3………………………..74

48 Snapshot at timestep 85 without free surface multiples shows clearly the target P and S reflections…………………………….……………..…75

49 Shot 121, vertical component of velocity. Multiples and S-waves are not suppressed. Shooting near salt allows us to see reflectors pinching out at the stem of a salt diapir………………………...………76

FIGURE Page

50 Shot 001, pressure. Exp. Gain, AGC=90, absorbing top boundary. Vs=0. P-wave amplitudes in salt are severely diminished………………..78

51 Shot 001, pressure. Exp. Gain, AGC=90, absorbing top boundary. S-wave amplitudes are not diminished in salt as P-wave amplitudes….....79

52 Shot 161, pressure. Exp. Gain, AGC=90, absorbing top boundary. Vs=0. Very low amplitudes of P-wave in salt diapir……………….……..80

53 Shot 161, pressure. Exp. Gain, AGC=90, absorbing top. S-waves are abundant in salt……………………………………………….…...81

54 Shot 041, vertical component of velocity. Exp. Gain, AGC=90. S waves generated by salt diapirs………………………………….…..82

55 Shot 001, pressure. Exp. Gain, AGC=90. Top of salt P and S reflections…………………………………………………………....85

56 Shot 081, pressure. Exp. Gain, AGC=90. Top of salt P and S reflections…………………………………..…………………..…86

57 Shot 121, pressure. Exp. Gain, AGC=90. Top of salt P and S reflections…………………………………...…………………..…87

58 Shot 161, pressure. Exp. Gain, AGC=90. Top of salt P and S reflections…………………………………...…………………..…88

59 Shot 201, pressure. Exp. Gain, AGC=90. P and S reflections from top of salt…………………………….……………………….…….…89

60 Shot 241, pressure. Exp. Gain, AGC=90, absorbing top boundary. Top of anhydrites P reflection ………………………..………………90

61 Shot 041, vertical velocity component. Exp. Gain, AGC=90. Example of an S-wave generated by salt, where it can be mistaken for a P- wave bright spot ………...……………………………………..91

62 Snapshot showing clear delineation of steep salt diapir slopes by shear waves……………………………………………………………92

63 Snapshot with P waves only, which has no reflections from salt diapir steep slopes……………………………………………...…93

FIGURE Page

64 Snapshot of vertical geophone data, shot 222, absorbing top. Near vertical wavefront of the S-wave from a near vertical salt stem is approaching the geophone and being recorded as a vertical component of velocity. ……………………………………………........…94

LIST OF TABLES

TABLE Page

1 Elastic rock properties 23

2 Modeling parameters 41

CHAPTER I

INTRODUCTION

The area of our study is the southeastern part of the North Caspian Basin (NCB). It is located in Kazakhstan (Figure 1). High-resolution satellite images of the Caspian Sea and NCB are on Figures 2, 3, and 4.

Figure 1. The location of the North Caspian Basin and its southeastern part. (modified from UT Libraries, 2004)

This thesis follows the style and format of Geophysics.

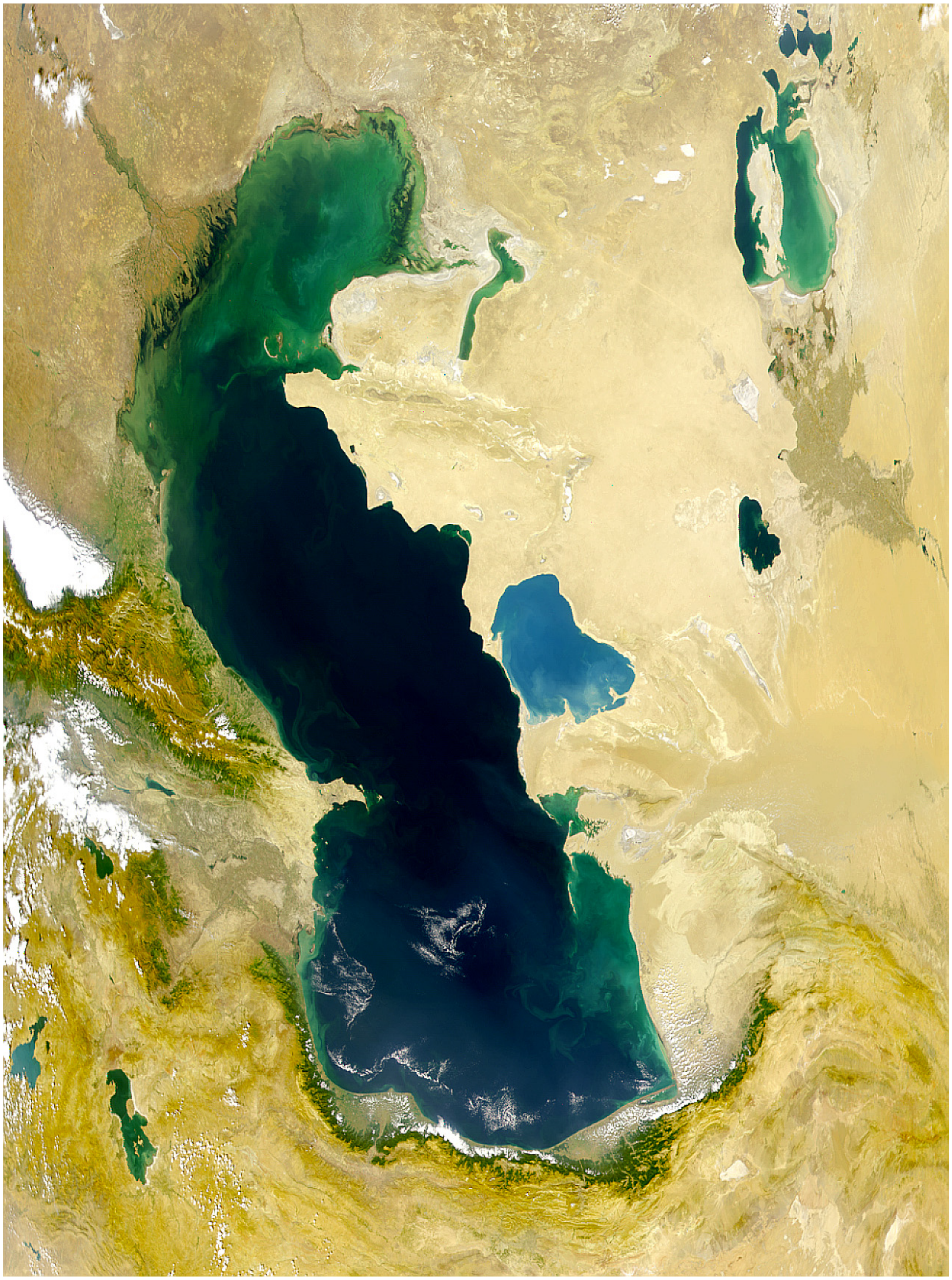

Figure 2. Satellite image of the Caspian Sea region. (NASA, 2004)

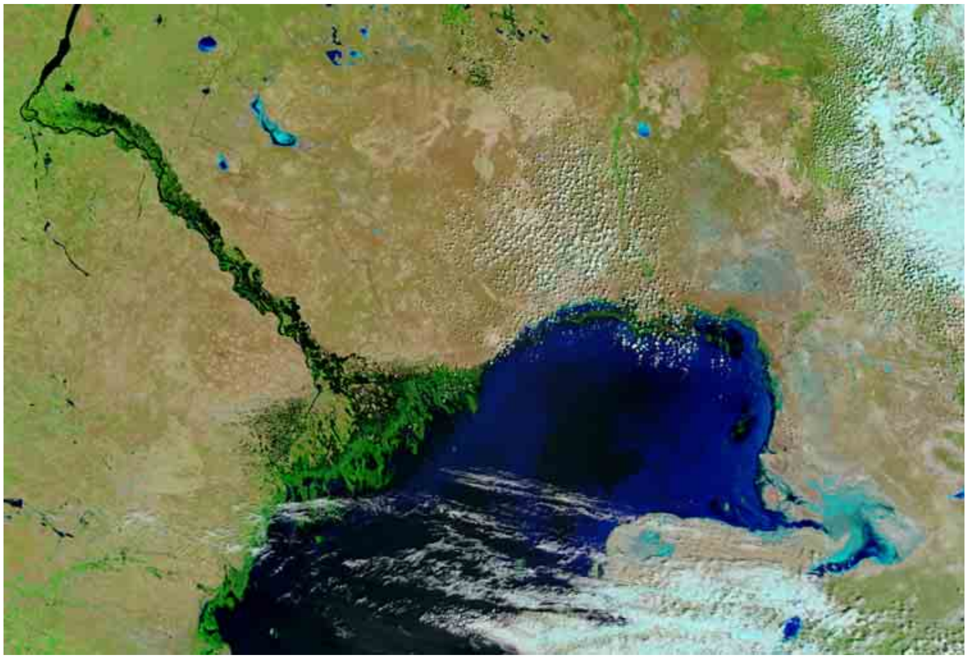

Figure 3. The North Caspian Basin from space. (NASA, 2004)

Figure 4. The North Caspian Sea is frozen 6 months a year. (NASA, 2004)

The area of the basin is about 500,000 square kilometers; the depth of sedimentary section is 20 km.

The southeastern area was chosen because the largest oil fields of the Basin (Kashagan, Kashagan-SW, Tengiz, Kairan, Aktoty) are located there. Seismic exploration discovered over 100 potentially petroliferous structures on the shelf of the Caspian Sea in the North Caspian Basin.

US DOE Energy Information Agency estimates the total oil reserves of Kazakhstan at 110 billions of barrels. There is a 50% probability of doubling this number in future explorations. (US DOE EIA, 2002). The US-Kazakhstan Business Association states that Tengiz has 13.5 billion extractable barrels of oil, and Kashagan is three times larger than Tengiz (U.S. – Kazakhstan Business Association, 2004). The area of the Kashagan reservoir, for example, is 80 by 40 km; the area size of Tengiz reservoir is 30 by 20 km.

Our ability to see oil and gas in the subsurface, to estimate the volume of reserves, the degree of extraction difficulty, and the success of the venture depends on our ability to image subsurface geological structures. The North Caspian Basin’s geological structures are quite challenging for exploration: On the Caspian region scale we have complex and dynamic plate tectonics; on the NCB scale we have shelf and slope carbonates, paleoatoll and barrier reefs; over carbonates and reefs we have salt tectonics and prograding sediments of Volga river and Ural mountains; on the field scale we have subsalt reef and carbonate overpressured reservoirs, salt domes and diapirs (halite and anhydrite) complicated with overhangs and canopies, and clastic reservoirs around and over salt structures. Hereafter the word “reef” here will be used interchangeably with the word “carbonate.”

In this study we will seek answers to the following questions affecting our ability to seismically image NCB subsalt, suprasalt, and nearsalt reservoirs:

- Can we see subsalt clastic and carbonate (reef) reservoirs through thick overburden?
- How do halites and anhydrites with their complex structure affect our ability to image target reflectors?
- Can we image carbonates (reef) located under salt domes and diapirs?
- Do shallow waters (3-15 m) of the Caspian Sea shelf affect our ability to image reservoirs?

There are other problems affecting our ability to work in the North Caspian Basin:

- Velocities are subject to anomalously high overpressure (87 MPa).
- Salts in the NCB are highly mobile because of the thick overburden that affects long term seismic imaging and drilling.
- Technogenic earthquakes are generated by oil extraction (shift the subsurface structure).
- Hydrogen sulfide and sulphur in oil (17%) present not only technological problems, but also very serious health/life concerns for people.
- The sea level constantly fluctuates (+/- 1.5 m /day).
- Climate (- 40° C in the winter, + 40° C in the summer) impacts acquisition.

- The rising Caspian Sea level generated by local tectonic forces (a long term consideration).

This study addresses problems that a seismic method is likely to encounter in the Caspian Basin. How do we address these problems?

Seismic imaging and interpretation are ill-posed problems having an infinite number of solutions. In order for us to minimize the number of possible seismic imaging results and interpretations we solve a well-posed problem, i.e. a forward problem of seismic. The forward problem of seismic is not soluble analytically for the realistic geological model; therefore we will be solving the wave equation numerically.

We will generate a 2D geological model of the typical NCB oil field and solve the *elastic* wave equation, thus simulating an *elastic* seismic survey. This will generate a dataset on which seismic imaging methods can be applied to better understand *elastic* wave propagation in the complex salt-carbonate geological setting and better image a known geological model of a typical oil field from NCB. Therefore, the scope of this study is to create a geological model, generate data, and analyze the *raw* data.

First, we construct a 2D elastic isotropic 10 by 6 km geological model of the area of interest: on the shelf of the Caspian Sea in the southeastern part of the North Caspian Basin, which has the largest oil fields. We used all available literature of Soviet and Western geoscientists. I have also used my internship experience with oil companies, where I worked on subsalt and suprasalt 2D and 3D seismic data from the North Caspian Basin, Kazakhstan.

The constructed model is large enough to be representative of the typical geology of NCB reservoirs and at the same time is practical in terms of computing time. The model is realistic and sufficiently detailed, but not overburdened with details, as the nature of our problem is more structural than stratigraphic. Rock properties of the model were chosen using well logs, Prestack Depth Migration velocities, existing rock physics empirical equations for Vp/Vs ratio for clastics and carbonates, and results of laboratory measurements on cores with the simulation of in situ PT conditions.

To generate and record a wavefield from our exploration oriented geological model, we discretize in space and time and numerically solve the elastodynamic equations of wave motion for a set of initial and boundary conditions. The discretization technique that we used is known as the "staggered grid scheme" (Graves, 1996). This technique has the advantage of avoiding taking the spatial derivative of the medium. The staggered grid allows us to model a complex heterogeneous subsurface. In summary, we solve these elastodynamic equations using a 2D finite-difference algorithm with 4th order approximation of the spatial derivative and 2nd order approximation of the time derivative. 4th order staggered grid finite-difference modeling allows us to model geology with any Poisson ratio and provides more stability and less grid dispersion than 2nd order FDM.

This scheme for FDM calculates a wavefield for a unit of space from the wavefield of a previous space unit and a previous time step. This formulation allows us to consider a heterogeneous geological model as a set of locally homogeneous layers with constant Vp, Vs, and density and solve N equations corresponding to N homogeneous areas. In addition, the elastic version allows us to generate pressure along with horizontal and vertical components of particle velocity. In other words, we have a very effective technique for our task.

The acquisition technique is 3-component (pressure, Vx, and Vz) Ocean Bottom Seismic (3C OBS). Our resulting dataset is composed of 314 shots with each shot being registered at 601 dual-sensor receivers (paired hydrophone and geophone). Synthetic seismograms are 6 seconds long. They are stored in SEGY format and will be available through the website of CASP (Consortium for Automated Seismic Data Processing) of Texas A&M University for anyone interested in testing their Prestack Depth Migration algorithms.

CHAPTER II

CONSTRUCTING THE GEOLOGICAL MODEL

GEOLOGICAL STRUCTURES

The North Caspian Syneclise (a syneclise is a large intracratonic depression) is an agglomerate of several genetically different types of basins that have evolved at different times. To decipher the history of an area, one has to look at deep seismic, gravity, magnetic fields, heat flow, contemporary structural and stratigraphic features, and the history of an entire continent. I infer that the basin had several stages of development:

First, extension: major rifting in Proterozoic and Paleozoic with volcanism, with and without exposure of an oceanic crust, caused by mantle uprising.

Second, contracting: rift inversion, folding, thrusting, and transform faulting in the Paleozoic, Mesozoic, and Cenozoic caused by collisions of following plates: Eastern European, Turanian, Scythian, Ural-Tobolsk, and, indirectly, the Caucasian, South Caspian, Iranian, and Arabian.

Based on the above rifting history, the North Caspian Syneclise shall contain an intracratonic basin, several rift basins, and foreland basins on its Southern and Eastern previously rifted margins.

The syneclise has completely rifted with exposure of the oceanic crust from the Eastern-European platform, but has not completely rifted from the Turanian and Scythian plates (Zholtaev, 1989, 1996). The Syneclise had an access to Tetis and Ural oceans that allowed the deposition of carbonate atolls and banks from Devonian to Permian times

(Zholtaev, 1989, 1996). In the Permian Kungurian time, the access to oceans was denied by continued collisions. The Kungurian salt was deposited as a result of ocean water evaporation. Since the Permian time, the Syneclise experienced deposition of clastic sediments with the hiatus from the early to middle Jurassic. The thickness of the clastic sedimentary layer is about 4 km on the margins, and 20 km in the center of the Syneclise. Clastic sedimentation gave rise to syn- and postdepositional salt tectonics (Volozh et al. 2003). Salt tectonics in its turn has influenced the sedimentation pattern. Tectonic processes and presalt structures also had a great input on distribution patterns and shapes of salt diapirs.

Hydrocarbons accumulated in the subsalt carbonates, suprasalt clastics, and nearsalt clastics. Nearsalt hydrocarbons are trapped under salt overhangs. Subsalt oil deposits are considered major accumulations (tens of billions of barrels), while suprasalt and nearsalt hydrocarbons are considered minor (hundreds of millions of barrels).

Because the term “Syneclise” is non-existent in Western literature, in this study we substituted “Syneclise” with an exploration and exploitation oriented word: “Basin”.

A typical exploration scenario for oil in the NCB would include a deep carbonate reservoir and a massive mobile salt over the reservoir.

My bibliographical search showed there are very few papers published on the geological structure of Tengiz and none on Kashagan. Our carbonate reservoir is constructed after the supergiant Tengiz oil and gas subsalt field. Pavlov (Pavlov et al. 1988) has studied the Tengiz oil field using data of a seismic survey, which covered 600 square kilometers. Figure 5 shows the seismic section of the eastern slope of the Tengiz.

On Figure 6 is the seismic section of the western slope of the Tengiz. Both seismic sections are from one seismic line # 669. Tengiz reef structure constitutes an ancient atoll appearing in plan view as a horseshoe with a lagoon opening toward the southeast. (Pavlov et al. 1988) Regarding the origin of the reef it is not clear whether we should consider the atoll to sit on top of the volcanic seamount, to be built atop of an oceanic plateau, or as a shelf atoll. The paleoatoll covers 400 square km. The thickness of the atoll is about 3-4 km. The depth of the top reef horizon is about 4 km. It is necessary to drill at least an 8 km deep well in order to find the OWC (oil-water contact). It was found (Pavlov et al. 1988) that there are two major or relatively continuous reflectors seen on seismic: one is representing a base of salt and a top of middle Carboniferous carbonates of the reef, another reflector representing a top middle Devonian clastics and carbonates in the base of reef. The reef is built of Upper Devonian to Middle Carboniferous deposits. On top of the paleoatoll were deposited Lower Permian Upper Artinskian (P1a2) clastics. Thick Kungurian (P1kg) salt was deposited on top of Lower Permian Upper Artinskian (P1a2) clastics and subsequently deformed.

Types of salt structures encountered in the region vary from little pillows on the edges of a basin to domes several kilometers thick in the center of the NCB. Volozh (Volozh et al. 1989) has found 1800 salt structures of different sizes, shapes, and maturities and classified them. Figure 7 shows the map by Volozh (Volozh et al. 1989), where the salt is zoned according to the classification he created. Zone VI (green belt) encompasses the major oil field of the NCB and is the zone of development of diapirs

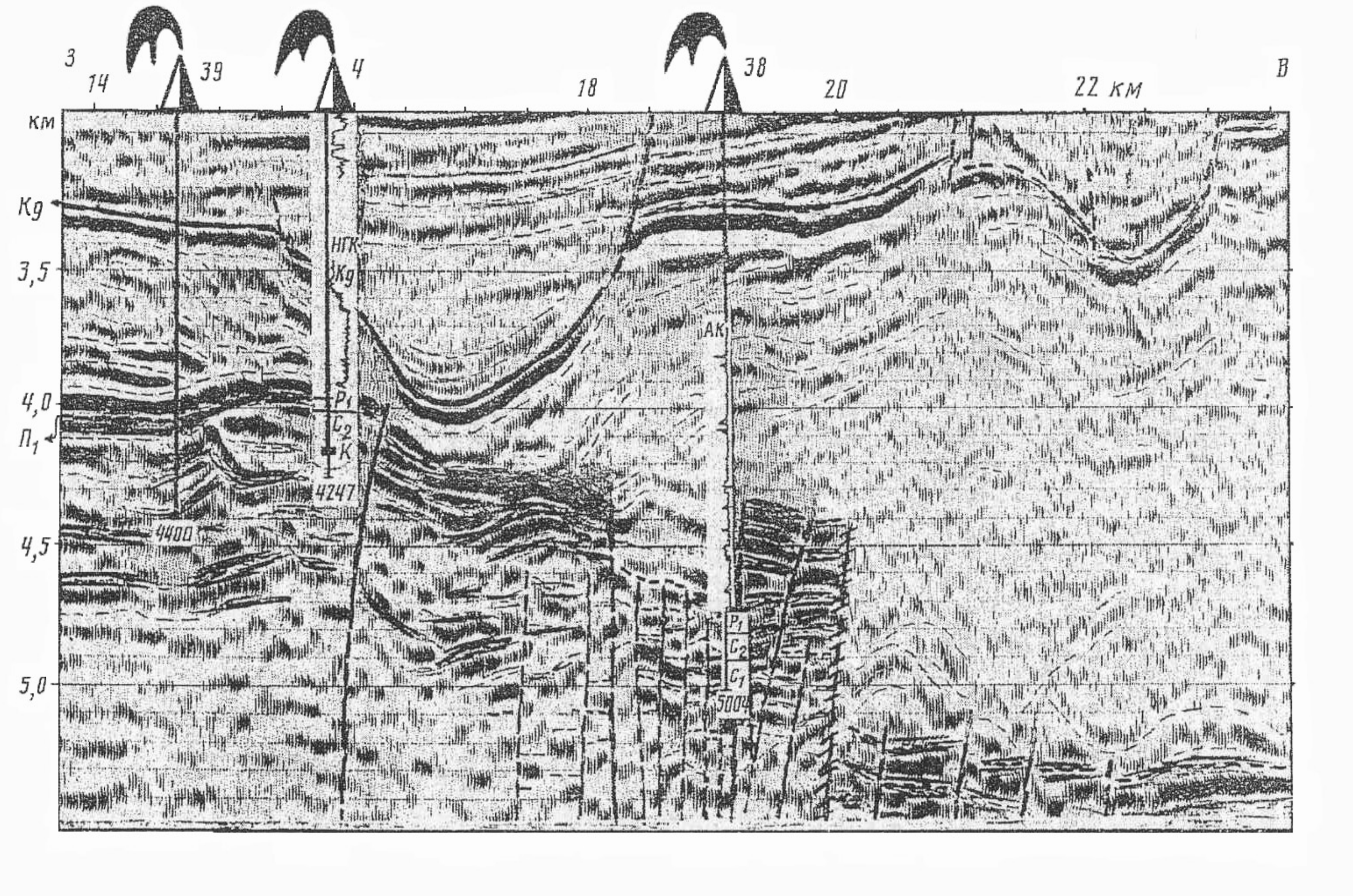

Figure 5. Seismic depth section of the eastern slope of the Tengiz paleoatoll (part of seismic line #669). (Pavlov, 1988)

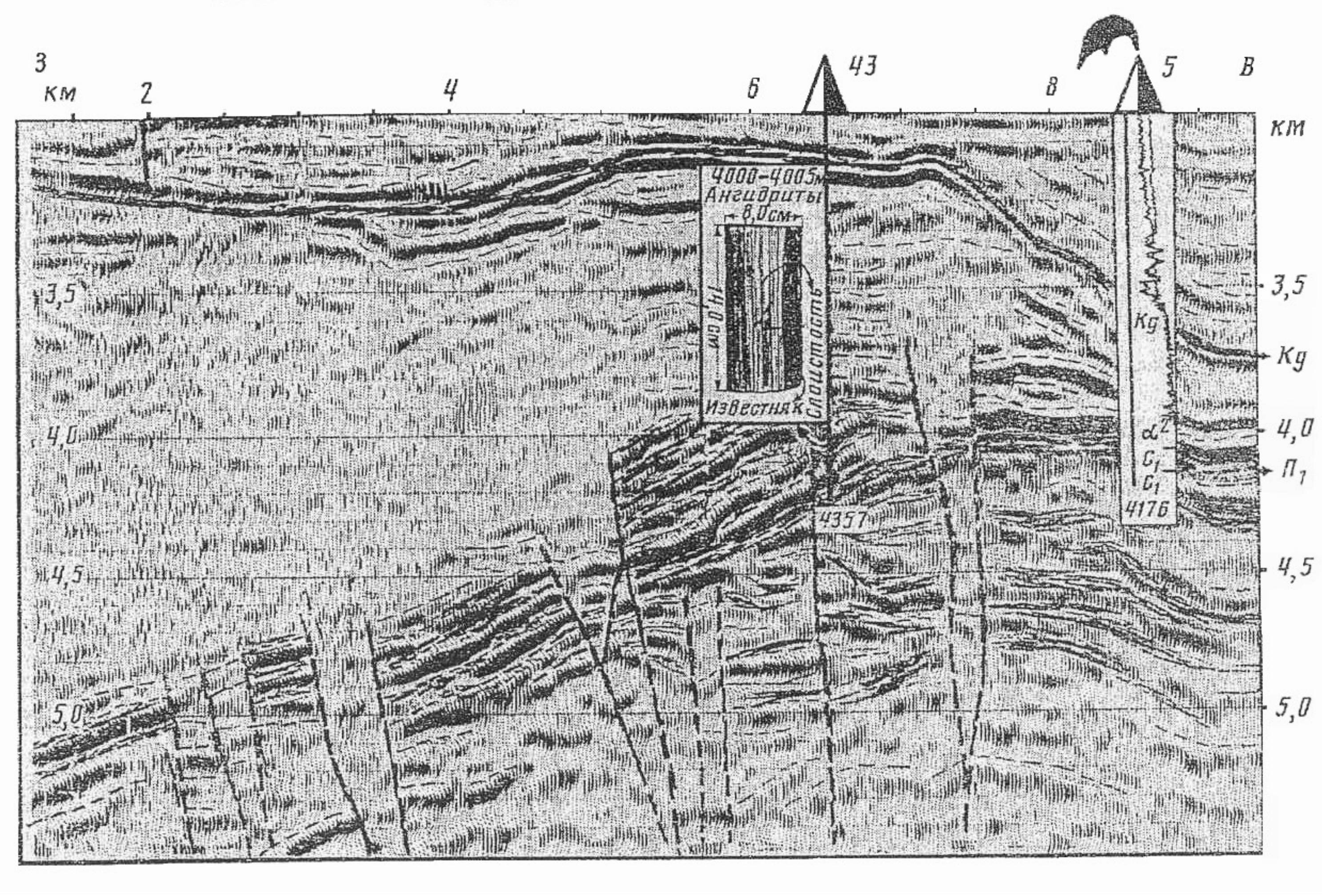

Figure 6. Seismic depth section of the western slope of the Tengiz paleoatoll (part of seismic line #669). (Pavlov, 1988)

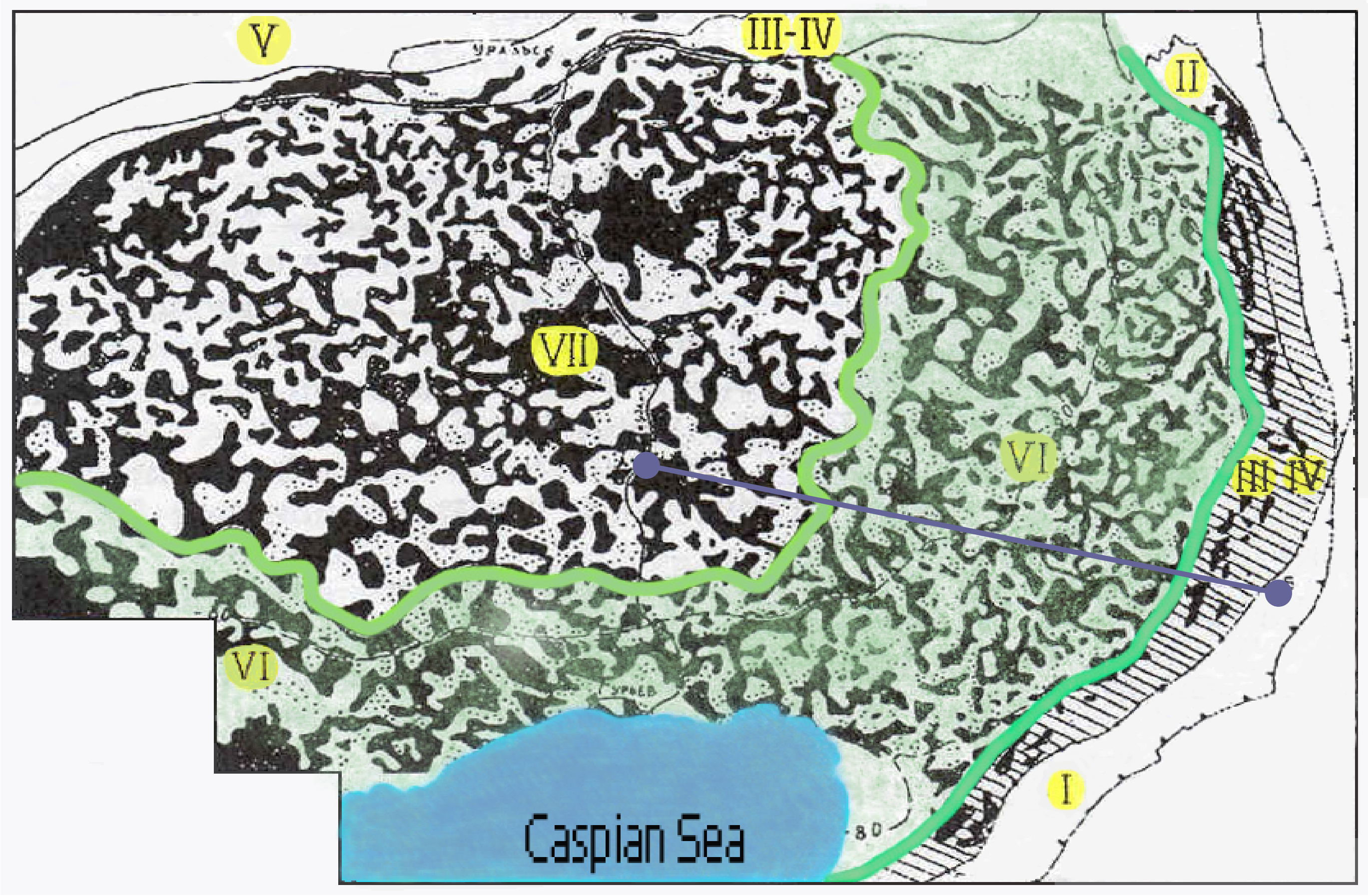

Figure 7. Map of salt structures of the North Caspian Basin (onshore only). (Modified from Volozh et al. 1989). The green zone represents salt domes and diapirs with overhangs.

with overhangs and canopies. A regional cross-section along the blue line is on Figure 8. A relatively recent (Volozh et al. 2003) regional cross section developed by Volozh is on Figure 9. Generally classification of salt structures heavily depends on the imaging powers of a seismic method. Because our area of exploration interest in the NCB is located inside the green zone, we are likely to encounter salt diapirs with canopies and overhangs when exploring in that green zone.

One specific to a leased block seismic study is published by Barde et al. (2002). They uncovered peculiar salt structures (Figure 10) by building a velocity model in the process of prestack depth migration (PreSDM) with the help of well data in the eastern section of the North Caspian Basin, in the block located inside the green belt of salt structures with overhangs and canopies defined by Volozh. Barde et al. (2002) found that salt was intensely deformed with diapirs as tall as 5 km. They also acknowledge that it is difficult to map the presalt (i.e. subsalt) structures because of seismic imaging problems.

The geological model (Figure 11) is a combination of regional (Volozh et al. 1989, 2003) as well as local (Barde et al. 2002) studies of the NCB. Because the most interesting exploration area in the NCB today is on the shelf of the Caspian Sea, we have chosen to include that scenario in our model. The model represents a 10 km portion of a 30 km long 2D seismic depth converted section 669 (Pavlov et al. 1988) of the Eastern slope of the Tengiz paleoatoll (Figure 5), specifically the section from 14 to 23.5 km. However, the depth of my model was extended to 6 km. The morphology of salt

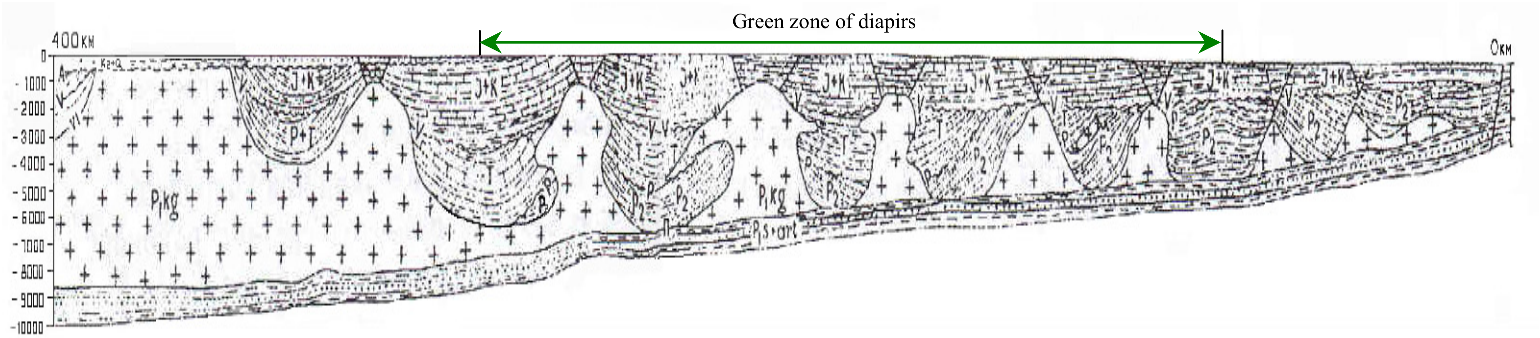

Figure 8. Cross-section from the seismic profile in the Fugure 7. (Modified from Volozh et al. 1989).

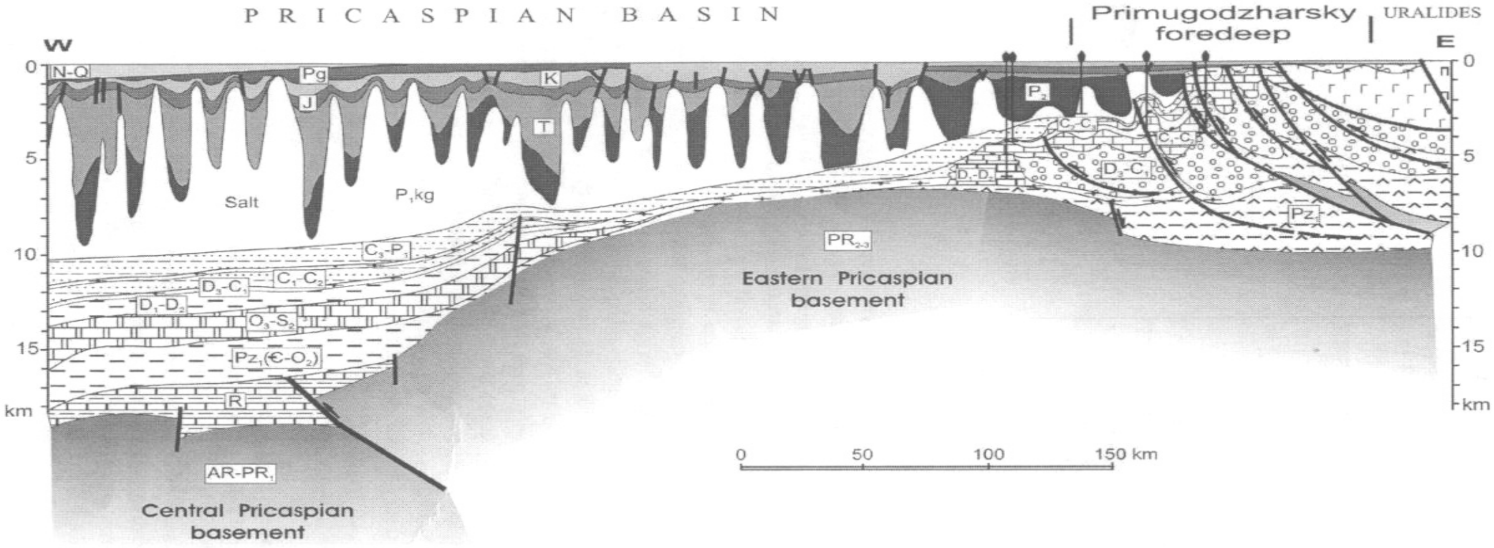

Figure 9. East-west cross section towards the center of the NCB. (modified from Volozh et al. 2003)

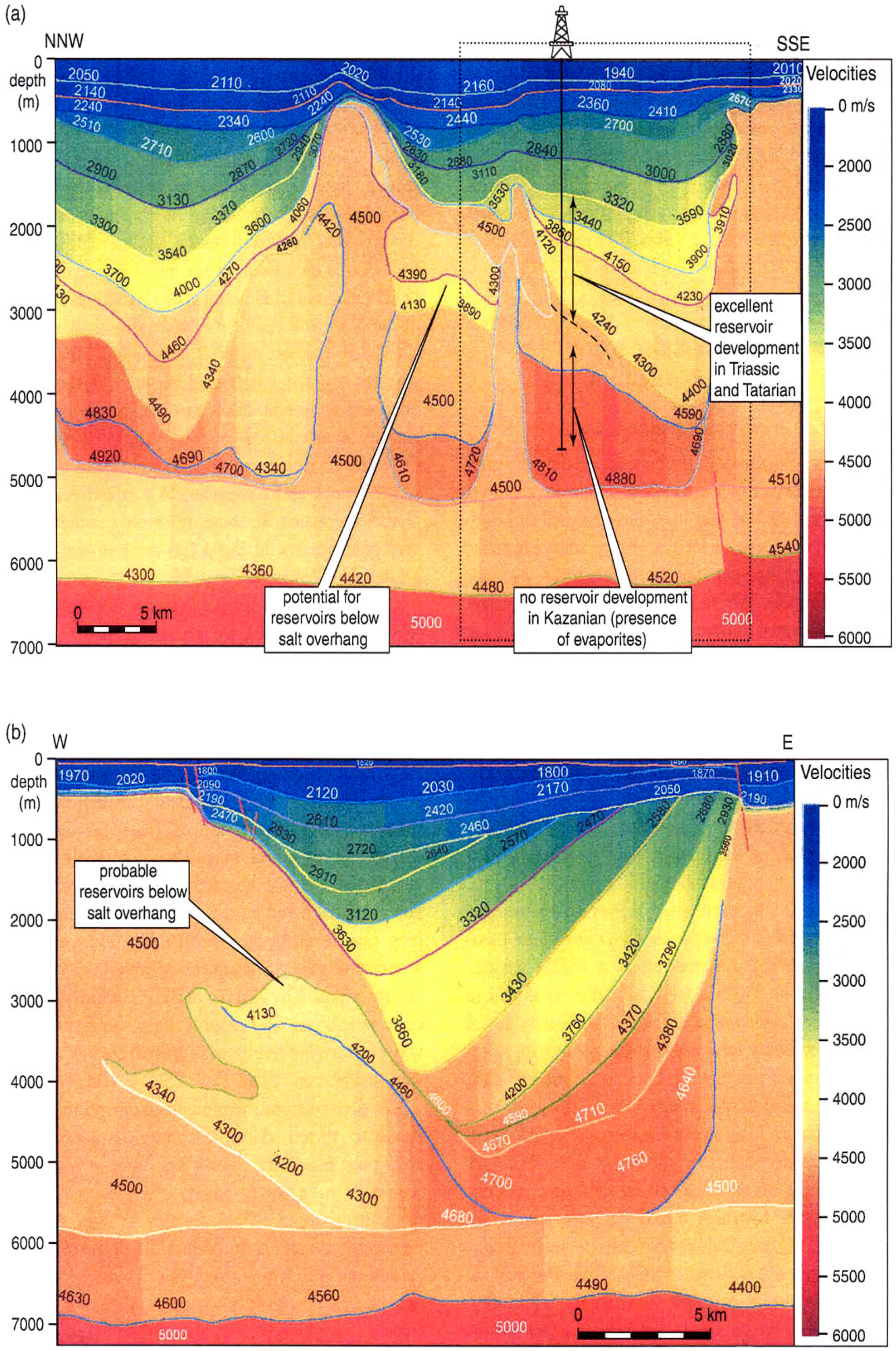

Figure 10. Post Stack Depth Migration results from the NCB (mod. from Barde et al. 2002)

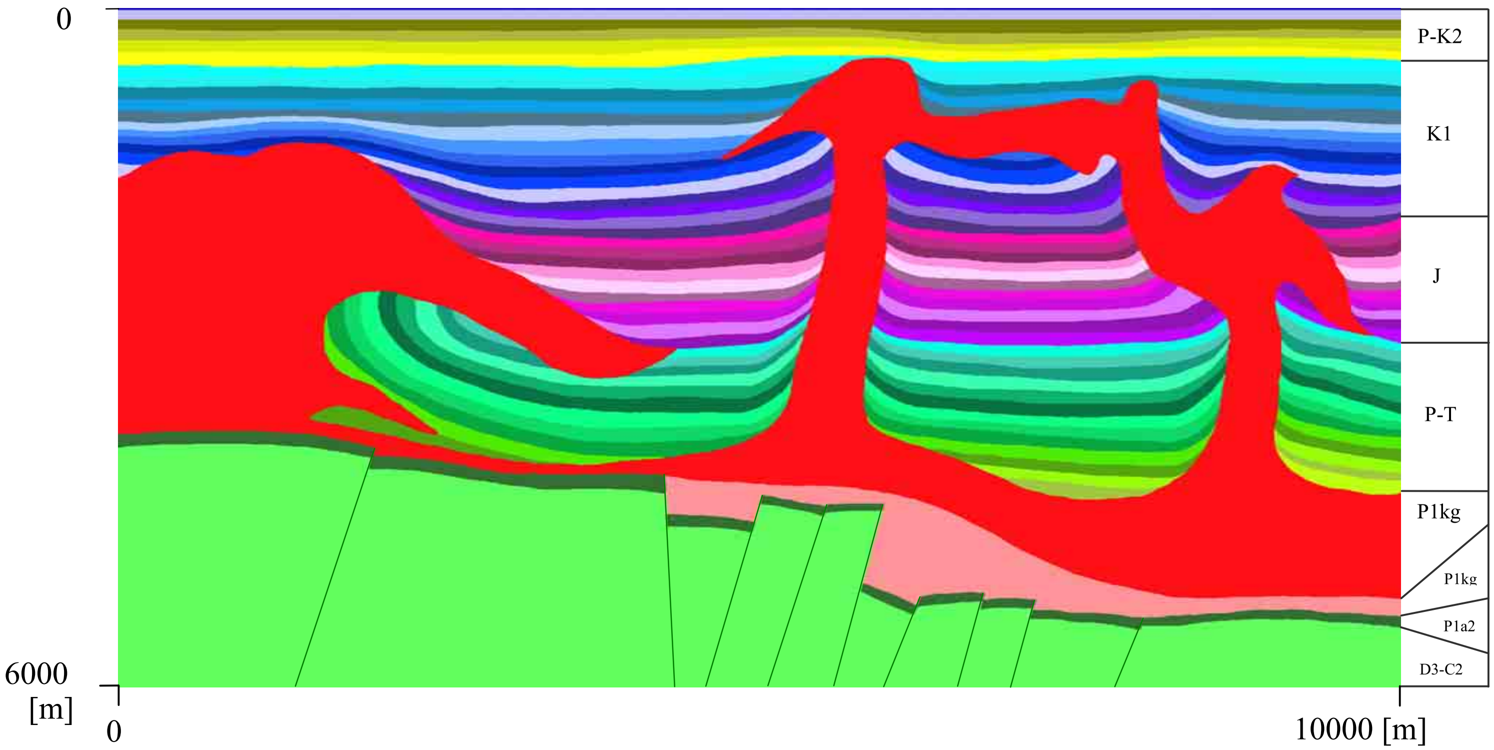

Figure 11. 2D geological model of the southeastern North Caspian Basin.

structures in the PreSDM velocity model by Barde et al. (2002) served as a guide for creating the salt dome and diapirs in my model.

Because the purpose is the investigation of seismic imaging problems for subsalt reservoirs and carbonates, my model is not overburdened with stratigraphic details

ELASTIC PROPERTIES OF ROCKS

There are three major types of rocks within our geological model of the southeastern area of the North Caspian Basin (Tengiz oil field in particular): carbonates of paleoatoll (CaCO3), salts (halite NaCl, anhydrite CaSO4), and clastics (silicates).

By elastic properties of rocks here mean density, velocity of compressional waves, and velocity of shear waves, and, by extension, – all the elastic ratios, coefficients, and moduli. The rock properties of the model are influenced by the anomalously high reservoir pressure (87MPa), high temperature gradient, high porosity and oil saturation in the reef carbonates, and by depth. Rock properties of the North Caspian Basin differ in *suprasalt*, *salt*, and *subsalt*. They are presented here accordingly (Table 1).

Rock elastic properties (Vp, Vs, density) of the southeastern area of the North Caspian Basin (Tengiz oil field in particular) were chosen using:

- well logs (Volozh et al. 2003, Kononkov et al. 1978, Shebaldin et al. 1988, Volarovitch, 1988, Kolosova, 1982, Kunin et al. 1977),
- Prestack Depth Migration velocities and well logs (Barde et al. 2002),
- existing rock physics empirical equations for Vp/Vs ratio (Dvorkin et al. 1999, Li and Downton, 2003, Stoughton, 2001),

- laboratory measurements on cores with the simulation of in situ PT conditions (Fomin et al. 1992, Baiuk and Fomin, 1989, Crain, 2004).

The shear wave values for suprasalt formations were calculated with the Poisson coefficient of 0.4, which made the ratio of compressional to shear wave equal to 2.44. That value of the Poisson ratio is the most probable based on the chart in Dvorkin's paper (Dvorkin et al. 2004), where the increase in the Poisson ratio corresponds to an increase in pore pressure for a water saturated calcite with crack porosity.

Subsalt rocks have anomalously high reservoir pressure (~87 MPa). Therefore, I have obtained their elastic properties with terrigenous and carbonate oil saturated core samples subjected to regular and irregular stresses and temperatures corresponding to those in situ (Fomin et al. 1992). Fomin found that irregular stress (from regional tectonic stress, salt tectonics) increases the permeability and crack porosity of weak, mainly organic, limestones of the Tengiz. Fomin stated that primary values of Vp and the degree of its change with the increasing pressures is defined by the micro cracks, but the Vp in situ reservoir conditions depends on porosity. Therefore, Vp is relatively low for the reservoir conditions of the Tengiz. Anomalously high reservoir pressure in the North Caspian Basin subsurface decreases velocities of our subsalt clastics and carbonates to about 30-40% (Fomin et al. 1992).

I have assumed the carbonates to be one homogeneous formation and have assigned to it densities and compressional velocities averaged over many measurements on oil saturated core samples.

The shear velocities for carbonates were calculated from an empiric formula developed by Li and Downton specifically for carbonates (Li and Downton, 2003). The averaged Vp for a subsalt terrigenous P1a2 overpressured formation was obtained from works of Volozh and Kunin.

Notice that we have included error bars for velocities and densities in Table 1. This error bars are quite small, in most cases less than 5%. We know that seismic image starts getting affected by errors in velocities and densities when they are above 5%. More specifically, migration is unaffected by changes of less than 5% in velocity. AVO is only affected by changes in velocity of 10% or above. Therefore, the error bars in Table 1, which are generally less than 5%, can be ignored without affecting the conclusions that we will make in the last chapter about processing and imaging challenges in North Caspian Basin. Therefore, the values of velocities and densities in Table 1 will be used in a numerical modeling in Chapter III without the error bar.

I have constructed a realistic and sufficiently detailed 2D geological model with elastic rock properties based on the many regional and local studies of the Former USSR and Western researchers, taking into account the peculiarities of the Tengiz oil field rock properties derived from well logs, experiments on cores, prestack depth migration, and empirical rock physics equations. The distribution of elastic properties in the model are computed and presented in Figures 12-19.

Detailed and realistic, at the same time our geological model is a generalized and simplified geological model of the North Caspian Basin. This allows us to better concentrate on the main imaging problem and to generalize results of our seismic modeling effort over the entire southeastern area of the North Caspian Basin. We could endlessly add geological features and details to the model, but this would make our synthetic seismograms too complex and difficult to interpret. Future modeling efforts shall include more stratigraphy and heterogeneity, because after this modeling it will be known how principle geological structures look on seismic. New modeling efforts should also include the effect of overpressure, oil and gas saturation, and anisotropy, and be 3D.

In the next chapter, we describe the finite difference method of numerical modeling for wave propagation in the subsurface. We also describe the parameters of our numerical seismic survey.

.

Table 1.Elastic rock properties. Notice that we have included the error bars (i.e. |ΔVp|, |ΔVs|, |Δρ|) to velocities and densities values. However, in subsequent numerical modeling in Chapter III we will se these values without error bars.

Category	**Layer**	**Vp, m/s**	**|ΔVp|, m/s**	**Vs, m/s**	**|ΔVs|, m/s**	**ρ, kg/m3**	**|Δρ|, kg/m3**	**References for Vp**	**References for Vs**	**References for ρ**
	water	1500		0		1000				
suprasalt	terrig P-K2	1940	58.2	795	34.060	2100	52.50	Barde et al. 2002	Dvorkin et al. 2004	Kononkov et al. 1978
suprasalt	terrig P-K2	2000	60.0	820	35.080	2100	52.50	Barde et al. 2002	Dvorkin et al. 2004	Kononkov et al. 1978
suprasalt	terrig P-K2	2050	61.5	840	35.998	2120	53.00	Barde et al. 2002	Dvorkin et al. 2004	Kononkov et al. 1978
suprasalt	terrig P-K2	2340	70.2	959	41.076	2130	53.25	Barde et al. 2002	Dvorkin et al. 2004	Kononkov et al. 1978
suprasalt	terrig K1	2410	72.3	988	42.280	2110	52.75	Barde et al. 2002	Dvorkin et al. 2004	Kononkov et al. 1978
suprasalt	terrig K1	2500	75.0	1025	43.851	2116	52.90	Barde et al. 2002	Dvorkin et al. 2004	Kononkov et al. 1978
suprasalt	terrig K1	2590	77.7	1061	45.502	2122	53.05	Barde et al. 2002	Dvorkin et al. 2004	Kononkov et al. 1978
suprasalt	terrig K1	2680	80.4	1098	47.072	2129	53.23	Barde et al. 2002	Dvorkin et al. 2004	Kononkov et al. 1978
suprasalt	terrig K1	2770	83.1	1135	48.643	2135	53.38	Barde et al. 2002	Dvorkin et al. 2004	Kononkov et al. 1978

Table 1. Continued

Category	**Layer**	**Vp, m/s**	**$\lvert\Delta Vp\rvert$, m/s**	**Vs, m/s**	**$\lvert\Delta Vs\rvert$, m/s**	**ρ, kg/m3**	**$\lvert\Delta\rho\rvert$, kg/m3**	**References for Vp**	**References for Vs**	**References for ρ**
suprasalt	terrig K1	2860	85.8	1172	50.213	2142	53.55	Barde et al. 2002	Dvorkin et al. 2004	Kononkov et al. 1978
suprasalt	terrig K1	2950	88.5	1209	51.784	2148	53.70	Barde et al. 2002	Dvorkin et al. 2004	Kononkov et al. 1978
suprasalt	terrig K1	3040	91.2	1246	53.354	2154	53.85	Barde et al. 2002	Dvorkin et al. 2004	Kononkov et al. 1978
suprasalt	terrig K1	3130	93.9	1283	54.925	2161	54.03	Barde et al. 2002	Dvorkin et al. 2004	Kononkov et al. 1978
suprasalt	terrig K1	3220	96.6	1320	56.496	2167	54.18	Barde et al. 2002	Dvorkin et al. 2004	Kononkov et al. 1978
suprasalt	terrig K1	3310	99.3	1357	58.066	2174	54.35	Barde et al. 2002	Dvorkin et al. 2004	Kononkov et al. 1978
suprasalt	terrig K1	3400	102.0	1393	59.717	2180	54.50	Barde et al. 2002	Dvorkin et al. 2004	Kononkov et al. 1978
suprasalt	terrig K1	3490	104.7	1430	61.288	2187	54.68	Barde et al. 2002	Dvorkin et al. 2004	Kononkov et al. 1978
suprasalt	terrig K1	3580	107.4	1467	62.858	2193	54.83	Barde et al. 2002	Dvorkin et al. 2004	Kononkov et al. 1978
suprasalt	terrig K1	3670	110.1	1504	64.429	2199	54.98	Barde et al. 2002	Dvorkin et al. 2004	Kononkov et al. 1978

Table 1. Continued

Category	**Layer**	**Vp, m/s**	**|ΔVp|, m/s**	**Vs, m/s**	**|ΔVs|, m/s**	**ρ, kg/m^3**	**|Δρ|, kg/m^3**	**References for Vp**	**References for Vs**	**References for ρ**
suprasalt	terrig J	3700	37.0	1516	64.979	2200	66.00	Volarovitch, 1988	Dvorkin et al. 2004	Shebaldin et al. 1988
suprasalt	terrig J	3744	37.4	1534	65.754	2210	66.30	Volarovitch, 1988	Dvorkin et al. 2004	Shebaldin et al. 1988v
suprasalt	terrig J	3788	37.9	1552	66.529	2220	66.60	Volarovitch, 1988	Dvorkin et al. 2004	Shebaldin et al. 1988
suprasalt	terrig J	3832	38.3	1570	67.304	2230	66.90	Volarovitch, 1988	Dvorkin et al. 2004	Shebaldin et al. 1988
suprasalt	terrig J	3876	38.8	1589	67.999	2240	67.20	Volarovitch, 1988	Dvorkin et al. 2004	Shebaldin et al. 1988
suprasalt	terrig J	3920	39.2	1607	68.774	2250	67.50	Volarovitch, 1988	Dvorkin et al. 2004	Shebaldin et al. 1988
suprasalt	terrig J	3964	39.6	1625	69.549	2260	67.80	Volarovitch, 1988	Dvorkin et al. 2004	Shebaldin et al. 1988
suprasalt	terrig J	4008	40.1	1643	70.324	2270	68.10	Volarovitch, 1988	Dvorkin et al. 2004	Shebaldin et al. 1988
suprasalt	terrig J	4052	40.5	1661	71.099	2280	68.40	Volarovitch, 1988	Dvorkin et al. 2004	Shebaldin et al. 1988
suprasalt	terrig J	4096	41.0	1679	71.874	2290	68.70	Volarovitch, 1988	Dvorkin et al. 2004	Shebaldin et al. 1988

Table 1. Continued

Category	Layer	Vp, m/s	|ΔVp|, m/s	Vs, m/s	|ΔVs|, m/s	ρ, kg/m3	|Δρ|, kg/m3	References for Vp	References for Vs	References for ρ
suprasalt	terrig J	4140	41.4	1697	72.649	2300	69.00	Volarovitch, 1988	Dvorkin et al. 2004	Shebaldin et al. 1988
suprasalt	terrig P1-Tr	2500	75.0	1025	43.851	2350	82.25	Barde et al. 2002	Dvorkin et al. 2004	Shebaldin et al. 1988 Kononkov et al. 1978 Barde et al. 2002
suprasalt	terrig P1-Tr	2720	81.6	1115	47.726	2361	82.64	Barde et al. 2002	Dvorkin et al. 2004	Shebaldin et al. 1988 Kononkov et al. 1978 Barde et al. 2002
suprasalt	terrig P1-Tr	2940	88.2	1205	51.600	2373	83.06	Barde et al. 2002	Dvorkin et al. 2004	Shebaldin et al. 1988 Kononkov et al. 1978 Barde et al. 2002
suprasalt	terrig P1-Tr	3160	94.8	1295	55.475	2384	83.44	Barde et al. 2002	Dvorkin et al. 2004	Shebaldin et al. 1988 Kononkov et al. 1978 Barde et al. 2002

Table 1. Continued

Category	Layer	Vp, m/s	|ΔVp|, m/s	Vs, m/s	|ΔVs|, m/s	ρ, kg/m3	|Δρ|, kg/m3	References for Vp	References for Vs	References for ρ
suprasalt	terrig P1-Tr	3380	101.4	1385	59.350	2396	83.86	Barde et al. 2002	Dvorkin et al. 2004	Shebaldin et al. 1988 Kononkov et al. 1978 Barde et al. 2002
suprasalt	terrig P1-Tr	3500	105.0	1434	61.471	2407	84.25	Barde et al. 2002	Dvorkin et al. 2004	Shebaldin et al. 1988 Kononkov et al. 1978 Barde et al. 2002
suprasalt	terrig P1-Tr	3600	108.0	1475	63.225	2419	84.67	Barde et al. 2002	Dvorkin et al. 2004	Shebaldin et al. 1988 Kononkov et al. 1978 Barde et al. 2002
suprasalt	terrig P1-Tr	3800	114.0	1557	66.733	2430	85.05	Barde et al. 2002	Dvorkin et al. 2004	Shebaldin et al. 1988 Kononkov et al. 1978 Barde et al. 2002
suprasalt	terrig P1-Tr	4000	120.0	1639	70.241	2442	85.47	Barde et al. 2002	Dvorkin et al. 2004	Shebaldin et al. 1988 Kononkov et al. 1978 Barde et al. 2002

Table 1. Continued

Category	**Layer**	**Vp, m/s**	**|ΔVp|, m/s**	**Vs, m/s**	**|ΔVs|, m/s**	**ρ, kg/m3**	**|Δρ|, kg/m3**	**References for Vp**	**References for Vs**	**References for ρ**
suprasalt	terrig P1-Tr	4200	126.0	1721	73.749	2453	85.86	Barde et al. 2002	Dvorkin et al. 2004	Shebaldin et al. 1988 Kononkov et al. 1978 Barde et al. 2002
suprasalt	terrig P1-Tr	4400	132.0	1803	77.257	2465	86.28	Barde et al. 2002	Dvorkin et al. 2004	Shebaldin et al. 1988 Kononkov et al. 1978 Barde et al. 2002
suprasalt	terrig P1-Tr	4600	138.0	1885	80.765	2476	86.66	Barde et al. 2002	Dvorkin et al. 2004	Shebaldin et al. 1988 Kononkov et al. 1978 Barde et al. 2002
suprasalt	terrig P1-Tr	4700	141.0	1926	82.520	2488	87.08	Barde et al. 2002	Dvorkin et al. 2004	Shebaldin et al. 1988 Kononkov et al. 1978 Barde et al. 2002
suprasalt	terrig P1-Tr	4800	144.0	1967	84.274	2500	87.50	Barde et al. 2002	Dvorkin et al. 2004	Shebaldin et al. 1988 Kononkov et al. 1978 Barde et al. 2002

Table 1. Continued

Category	**Layer**	**Vp, m/s**	**$\lvert\Delta Vp\rvert$, m/s**	**Vs, m/s**	**$\lvert\Delta Vs\rvert$, m/s**	**ρ, kg/m3**	**$\lvert\Delta\rho\rvert$, kg/m3**	**References for Vp**	**References for Vs**	**References for ρ**
salt	Halite P1kg	4500	45.0	2602	21.825	2200	77.00	Kolosova, 1982	Stoughton, 2001	Shebaldin et al. 1988
salt	Anhydrite P1kg	6000	120.0	3200	58.982	2970	59.40	Volozh et al. 2003, Kolosova, 1982	Li and Downton, 2003,	Grain's Petroph. Handbook, 2004
subsalt	terrig P1a2	2800	28.0	1148	49.113	2550	51.00	Volozh et al. 2003 overpress, terr, subsalt	Dvorkin et al. 2004	Kunin et al. 1977
subsalt	Reef D3-C2	4300	43.0	2327	32.376	2200	22.00	Fomin et al. 1992, Baiuk and Fomin, 1989 oil saturated, overpressured, PT, lab	Li and Downton, 2003,	Fomin et al.1992, Baiuk and Fomin, 1989 in situ lab, oil saturated, 1992

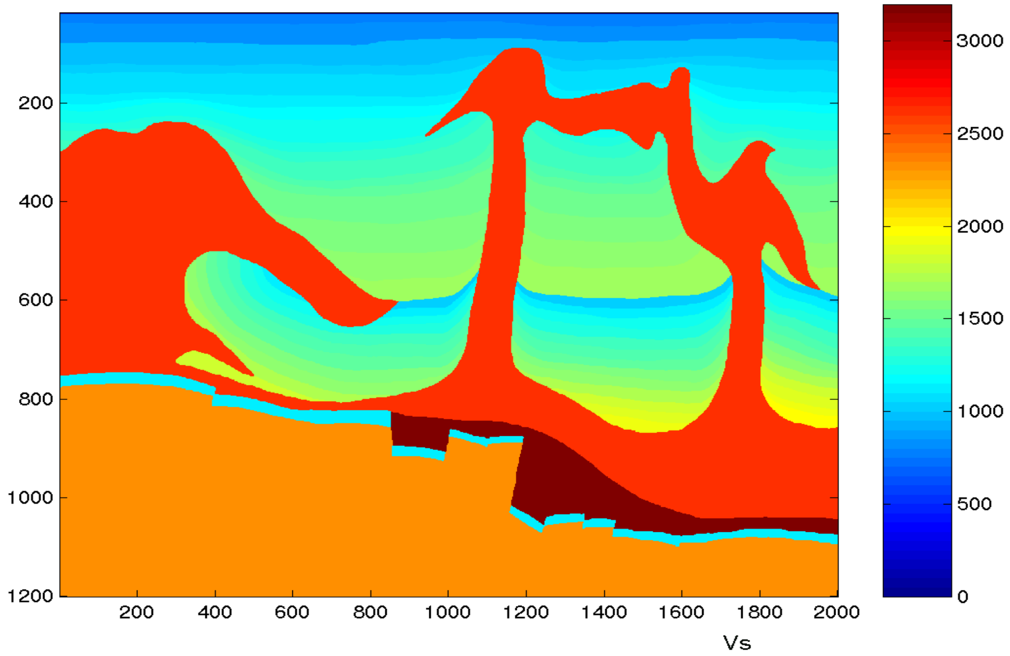

Figure 12. Distribution of shear wave velocities in the geological model.

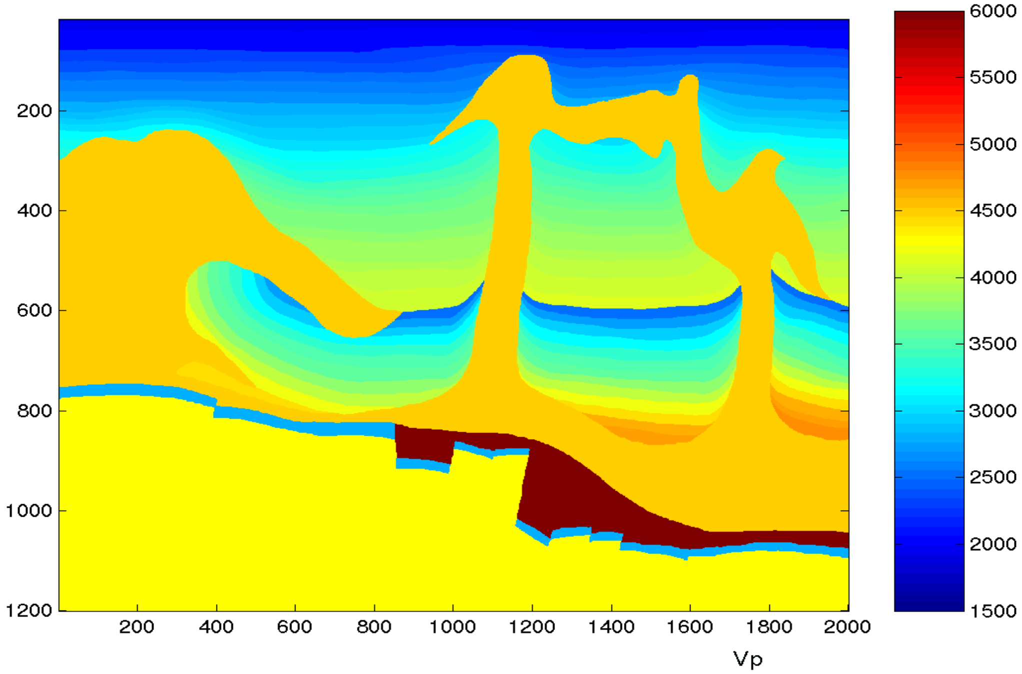

Figure 13. Distribution of compressional wave velocities in the geological model.

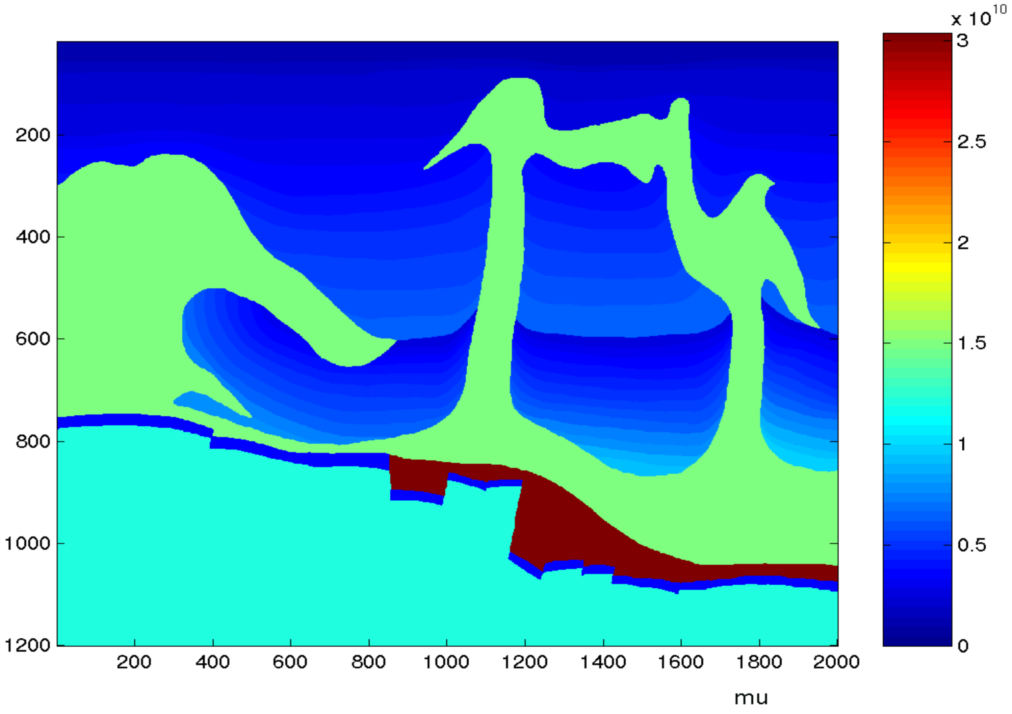

Figure 14. Distribution of shear modulus in the geological model.

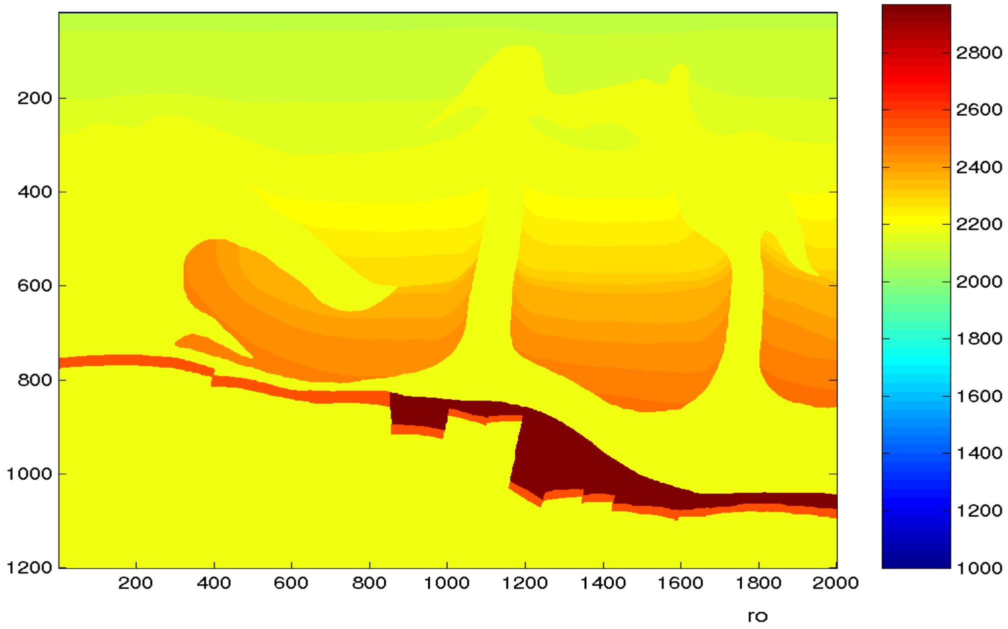

Figure 15. Distribution of densities in the geological model.

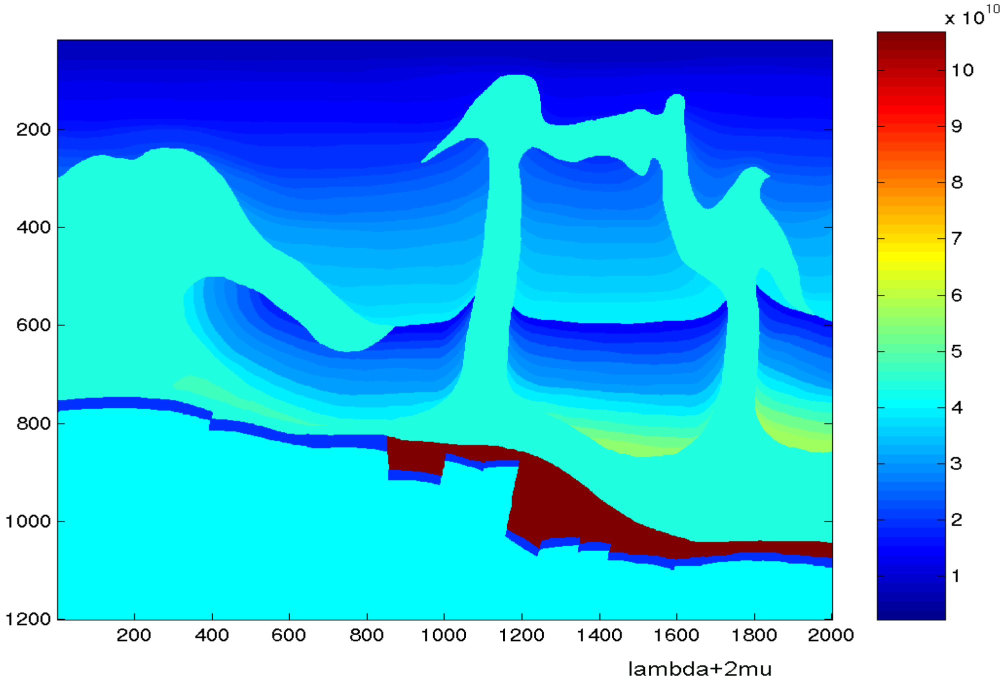

Figure 16. Distribution of [λ + 2μ] in the geological model.

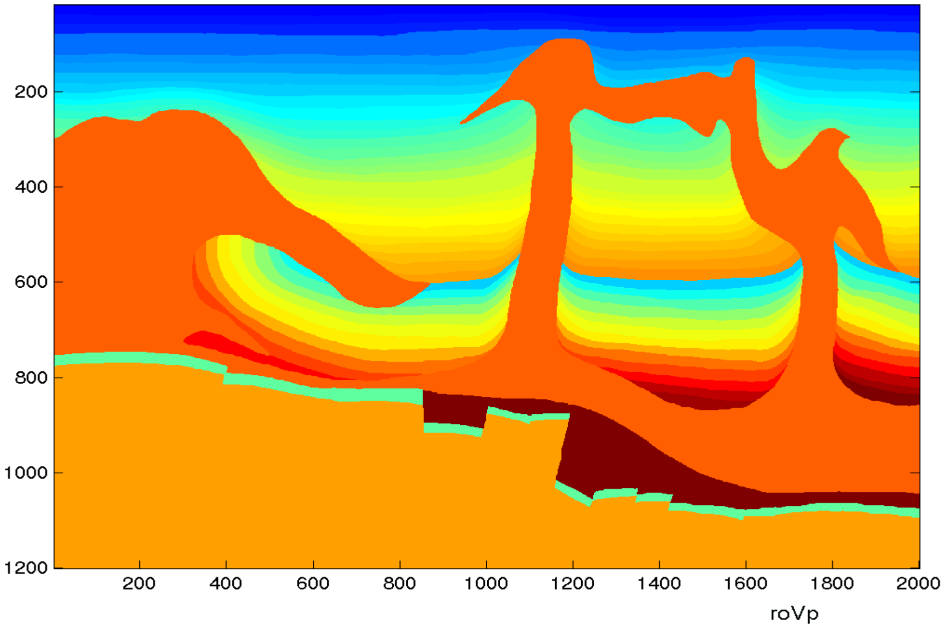

Figure 17. Distribution of compressional wave impedance in the geological model.

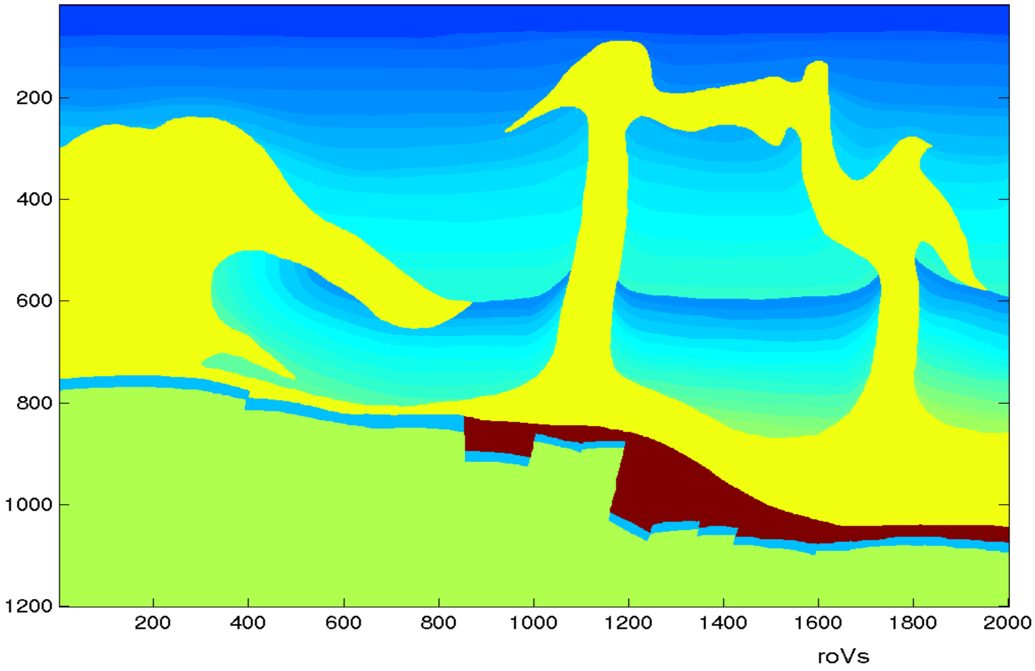

Figure 18. Distribution of shear wave impedance in the geological model.

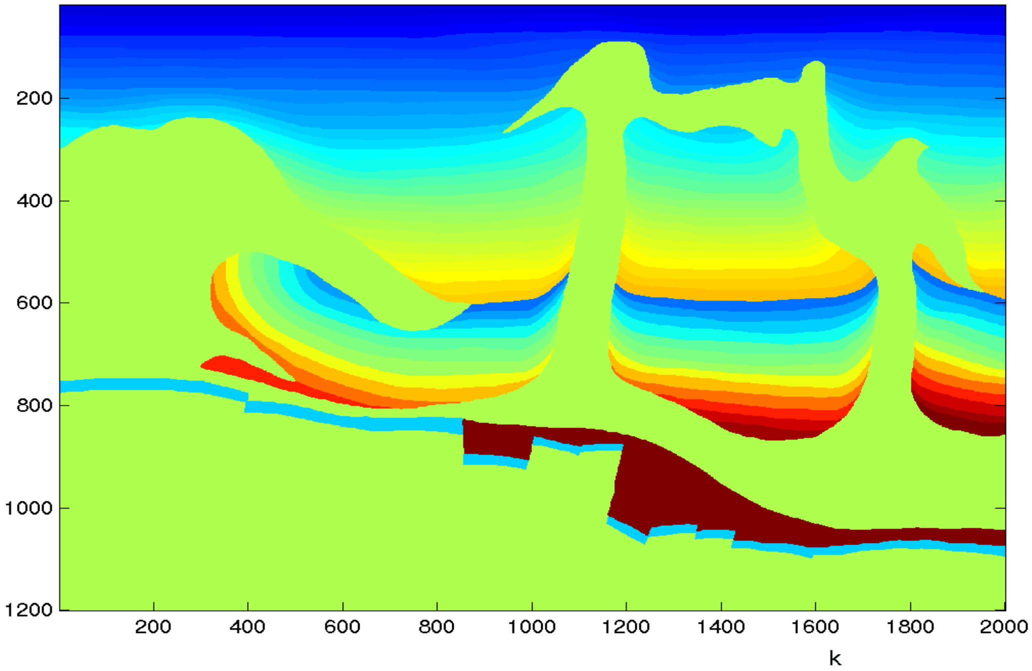

Figure 19. Distribution of bulk modulus in the geological model.

CHAPTER III

FINITE-DIFFERENCE MODELING

EQUATIONS FOR WAVE PROPAGATION IN ELASTIC MEDIA

We consider a heterogeneous geological model as a set of locally homogeneous layers with constant Vp, Vs, and density and solve N equations corresponding to N homogeneous areas. Incorporating elasticity allows us to generate and record horizontal and vertical components of a wavefield along with pressure.

1. 2D homogeneous formulation for equations of momentum conservation (Ikelle and Amundsen, 2004):

$$\rho(\mathbf{x})\partial_t v_x(\mathbf{x},t) - \{\partial_x \tau_{xx}(\mathbf{x},t) + \partial_z \tau_{xz}(\mathbf{x},t)\} = f_x(\mathbf{x},t) \ , \tag{1}$$

$$\rho(\mathbf{x})\partial_t v_z(\mathbf{x},t) - \{\partial_x \tau_{xz}(\mathbf{x},t) + \partial_z \tau_{zz}(\mathbf{x},t)\} = f_z(\mathbf{x},t) \ . \tag{2}$$

Here $\mathbf{v} = (v_x, v_z)$ is particle velocity,

$\boldsymbol{\tau} = (\tau_{xx}, \tau_{zz}, \tau_{xz})$ is stress, and

$\mathbf{f} = (f_x, f_z)$ is body force.

2. Relations of stress and strain for the isotropic elastic media:

$$\partial_t \tau_{xx}(\mathbf{x},t) = [\lambda(\mathbf{x}) + 2\mu(\mathbf{x})]\,\partial_x v_x(\mathbf{x},t) + \lambda(\mathbf{x})\partial_z v_z(\mathbf{x},t) + I_{xx}(\mathbf{x},t) \ , \tag{3}$$

$$\partial_t \tau_{zz}(\mathbf{x},t) = [\lambda(\mathbf{x}) + 2\mu(\mathbf{x})]\,\partial_z v_z(\mathbf{x},t) + \lambda(\mathbf{x})\partial_x v_x(\mathbf{x},t) + I_{zz}(\mathbf{x},t) \ , \tag{4}$$

$$\partial_t \tau_{xz}(\mathbf{x},t) = \mu(\mathbf{x})\,[\partial_z v_x(\mathbf{x},t) + \partial_x v_z(\mathbf{x},t)] + I_{xz}(\mathbf{x},t) \ . \tag{5}$$

Here $\mathbf{I} = (I_{xx}, I_{zz}, I_{xz})$ is stress force, for the wave motion to satisfy first-order coupled differential equations (1) – (5).

3. Initial conditions such that the stress, particle velocities, and their time derivatives are equal to zero before firing of the source of wave propagation:

$$\mathbf{v} = \partial_t \mathbf{v} = \mathbf{0} \ , \ \ t \leq 0 \ ,$$

$$\boldsymbol{\tau} = \partial_t \boldsymbol{\tau} = \mathbf{0} \ , \ \ t \leq 0 \ . \tag{6}$$

4. Boundary conditions are for air-water free surface planar boundary at depth z = 0:

$$\tau_{zz}(x, z=0, t) = \tau_{xz}(x, z=0, t) = 0 \ , \text{ or} \tag{7}$$

$$[\lambda(\mathbf{x})) + 2\mu(\mathbf{x})]\,\partial_z v_z(x, z=0, t) + \lambda(\mathbf{x})\partial_x v_x(x, z=0, t) =$$

$$= \mu(\mathbf{x})\,[\partial_z v_x(x, z=0, t) + \partial_x v_z(x, z=0, t)] = 0 \ . \tag{8}$$

DISCRETIZATION OF EQUATIONS OF WAVE PROPAGATION ON A STAGGERED GRID

To solve our wave equations for elastic isotropic media numerically we discretize (Graves, 1996) equations along with their boundary conditions and in time and space:

$$t = n\Delta t \ , \ \ n = 0, 1, 2, ..., N \ \ ,$$

$$x = i\Delta x \ , \ \ i = 0, 1, 2, ..., I \ \ ,$$

$$z = k\Delta x \ , \ \ k = 0, 1, 2, ..., K \ \ . \tag{9}$$

The discretization changes the format of functions in the equations (1) – (5), for example:

$$\lambda(x,z) = \lambda(i\Delta x, k\Delta x) = \lambda_{i,k}$$

$$\tau_{xz}(x,z,t) = \tau_{xz}(i\Delta x, k\Delta x, n\Delta t) = [\tau_{xx}]^n_{i,k} \tag{10}$$

The picture below (Figure 20) is an example of a staggered grid technique (discussed further), where we see that some values are gridded at the point of the reference grid defined by (9), but other values are gridded at half a grid point from the reference grid points.

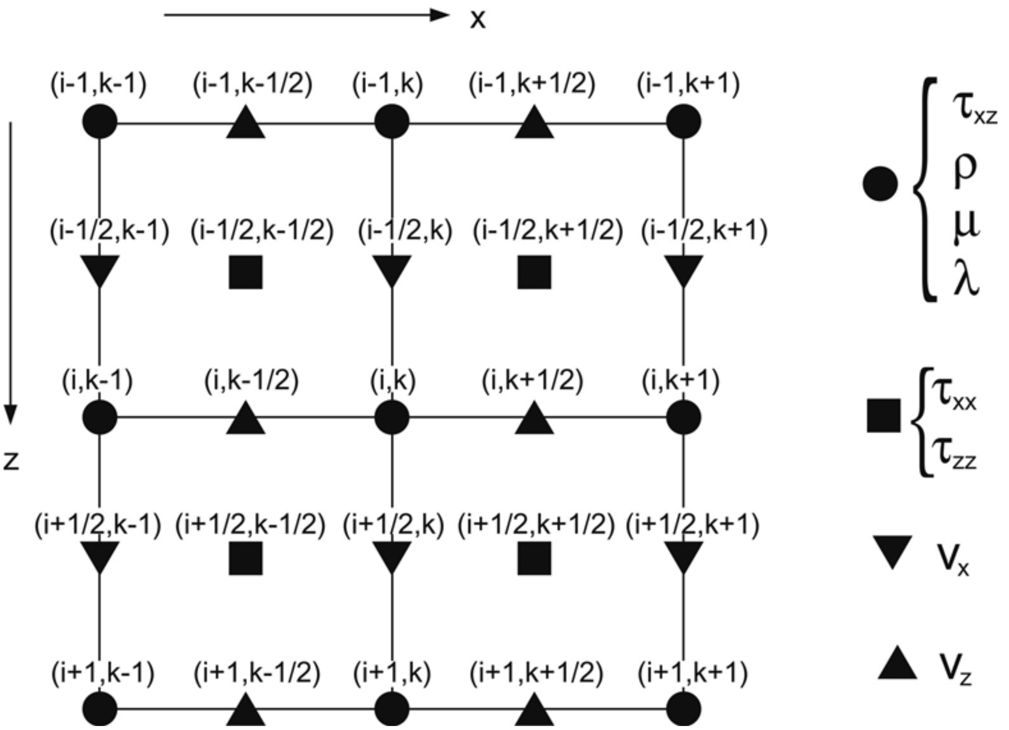

Figure 20. Illustration of the staggered grid technique (Ikelle and Amundsen, 2004).

The explicit scheme for FDM calculates the wavefield for a unit of space from the wavefield of a previous space unit and a previous time step. The staggered grid method allows to model complex heterogeneous geological models. Equations (1) – (5) were discretized (Ikelle and Amundsen, 2004) using the staggered grid technique:

$$[v_x]_{i,k+1/2}^{n+1/2} = [v_x]_{i,k+1/2}^{n-1/2} + [\Delta t b_x \left(D_x \tau_{xx} + D_z \tau_{xz} + F_x\right)]_{i,k+1/2}^{n} \tag{11}$$

$$[v_z]_{i+1/2,k}^{n+1/2} = [v_x]_{i+1/2,k}^{n-1/2} + [\Delta t b_z \left(D_x \tau_{xz} + D_z \tau_{zz} + F_z\right)]_{i+1/2,k}^{n} \tag{12}$$

$$[\tau_{xx}]_{i+1/2,k+1/2}^{n+1} = [\tau_{xx}]_{i+1/2,k+1/2}^{n} + \Delta t \left[(\lambda + 2\mu) D_x v_x + \lambda D_z v_z\right]_{i+1/2,k+1/2}^{n+1/2} \tag{13}$$

$$[\tau_{zz}]_{i+1/2,k+1/2}^{n+1} = [\tau_{zz}]_{i+1/2,k+1/2}^{n} + \Delta t \left[(\lambda + 2\mu) D_z v_z + \lambda D_x v_x\right]_{i+1/2,k+1/2}^{n+1/2} \tag{14}$$

$$[\tau_{xz}]_{i,k}^{n+1} = [\tau_{xz}]_{i,k}^{n} + \Delta t \left[\mu_{xz} \left(D_z v_x + D_x v_z\right)\right]_{i,k}^{n+1/2} \tag{15}$$

where

$$b_x = \frac{1}{2}\left[b_{i,k} + b_{i-1,k}\right], \tag{16}$$

$$b_z = \frac{1}{2}\left[b_{i,k} + b_{i,k-1}\right] \tag{17}$$

are effective media parameters for the reciprocal of density;

$$\mu_{xz} = 4\left[\frac{1}{\mu_{i,k}} + \frac{1}{\mu_{i-1,k}} + \frac{1}{\mu_{i,k-1}} + \frac{1}{\mu_{i-1,k-1}}\right]^{-1} \tag{18}$$

is the effective media parameter for the rigidity;

D_x and D_z are operators denoting the first-order spatial derivative for x and z respectively.

Forth-order order approximation of spatial derivatives allows us to model geology with any Poisson ratio and provides more stability and less grid dispersion than 2nd order FDM. This is the formulation for the forth-order finite-difference approximation for the operator D_x :

$$D_x g_{i,k} \approx \frac{1}{\Delta x}\left[\frac{9}{8}\left(g_{i+1/2,k} - g_{i-1/2,k}\right) + \frac{1}{24}\left(g_{i+3/2,k} - g_{i-3/2,k}\right)\right] . \qquad (19)$$

The forth order finite-difference approximation requires a minimum sampling of five grid points per wavelength.

STABILITY CONDITION

Stability ensures that the numerical solution is not departing too far from the analytical solution as time progresses. For the stability of our forth-order locally homogeneous FDM with the maximum velocity of V_{max}, extremely fine time sampling is necessary and the sampling rate must obey the following constraint:

$$\Delta t < 0.606 \frac{\Delta x}{V_{max}} \qquad (20)$$

GRID DISPERSION

Approximation of spatial derivatives creates the grid dispersion, which is the variation of velocity with frequency, when high frequencies are delayed relative to low frequencies, producing tailing of the signal. The larger the grid, the more the dispersion. Therefore, in our case it is necessary to have at least five grid points per wavelength.

BOUNDARY CONDITIONS

In addition to (7) we add the conditions

$$[\tau_{xz}]^{n+1}_{i,k=0} = 0 \ , \ [\tau_{xz}]^{n+1}_{i,k=-1} = -[\tau_{xz}]^{n+1}_{i,k=1} \tag{21}$$

$$[\tau_{zz}]^{n+1}_{i+1/2,k=-1/2} = -[\tau_{zz}]^{n+1}_{i+1/2,k=1/2} \tag{22}$$

$$[\tau_{zz}]^{n+1}_{i+1/2,k=-3/2} = -[\tau_{zz}]^{n+1}_{i+1/2,k=3/2} \tag{23}$$

These conditions are necessary for the vertical spatial derivative to be possible on a staggered grid. Two grid points are added above the free surface and antisymmetry for the stress components at the free surface is assumed. The rest of the medium is considered unbounded and surrounded by a strip of grids, which “absorbs” the waves. For that condition we multiply stress and particle velocity fields by the factor

$$G(i) = \exp\left\{-\left[\frac{0.3}{iabmax}(iabmax - i)\right]\right\}, \tag{24}$$

where $1 \leq i \leq iabmax$ and $iabmax$ is the strip width in the number of grid points.

This FDM scheme is implemented in its multishooting version in a Fortran code by Dr. Luc T. Ikelle, director of CASP (Consortium for Automated Seismic Processing) at Texas A&M University.

DISCRETIZATION OF THE GEOLOGICAL MODEL

- 10 by 6 km geological model in meters was created,
- discretization with 5 m grid size was decided, thus calculation of the wavefield are carried out on the nodes 5 by 5 meters,
- 2000 by 1200 pixels model was drawn in Adobe Photoshop in 24-bit colormap,
- run gmod2.m in Matlab to create input.modelM,
- compile and run gmod.f on input.modelM to create map.model
- plot map.model in Matlab
- save as .tiff

PARAMETERS OF SEISMIC ACQUISITION

Our geological model has only 15 m of water depth, therefore it was decided to have (3C OBS acquisition with double sensors (hydrophones and geophones), that is, one sensor is for pressure in the water, another – for horizontal and vertical components of particle velocity in the ground. A double sensor survey is beneficial as it collects multicomponent data (P and S wave arrival times and amplitudes). Recordings from both hydrophones and geophones are also used for removal of water reverberations (guided waves) and receiver ghosts by summation of data from two sensors (Ikelle, 1999a). It allows for PS migration, which will help to better image salt and significantly overpressured carbonates in the subsalt, and attenuation of free surface multiples through combination of streamer and OBS data. Stationary horizontal line of receivers is positioned from 500 m to 9500 m. Spacing of receivers is 15 m. Shot positions are from 500 m to 9890 m. Spacing of shots is 30 m. For all modeling parameters see Table 2.

Table 2. Modeling parameters.

Width of the model	10000 m
Depth of the model	6000 m
dx (grid size)	5 m
dt (FDM sampling rate)	0.2 ms
Shot spacing	30 m
Source wavelet	25 Hz Ricker
Receiver spacing	15 m
Water depth	15 m
Shot depth	10 m
Hydrophone depth	10 m
Geophone depth	20 m
Number of shots	314
First and last shot positions	500 m and 9890 m
Number of dual-sensor receivers	601
Shooting technique	Multishooting (Ikelle, 2003)
Listening time	6 sec
Sampling rate on record	4 ms
Maximum velocity in the model	6000 m/s
Run time	2 weeks
Computing resources	38 CPUs, 700 MHz. One shot per CPU

For the purpose of interpreting events correctly and identifying our imaging challenges, in addition to our three-component dataset with free surface boundary, we generated several versions of three component snapshots and shot gathers without free surface boundary (applying absorbing boundary conditions), and with and without converted waves, with and without carbonates and clastics, and their combinations.

This Finite-Difference Modeling scheme is implemented in its multishooting version in a Fortran code by Dr. Luc T. Ikelle – Director of Consortium for Automated Seismic Processing (CASP) at Texas A&M University.

On the next page (Figure 21) is one snapshot of wave propagation in the realistic subsurface, generated by the CASP FDM algorithm.

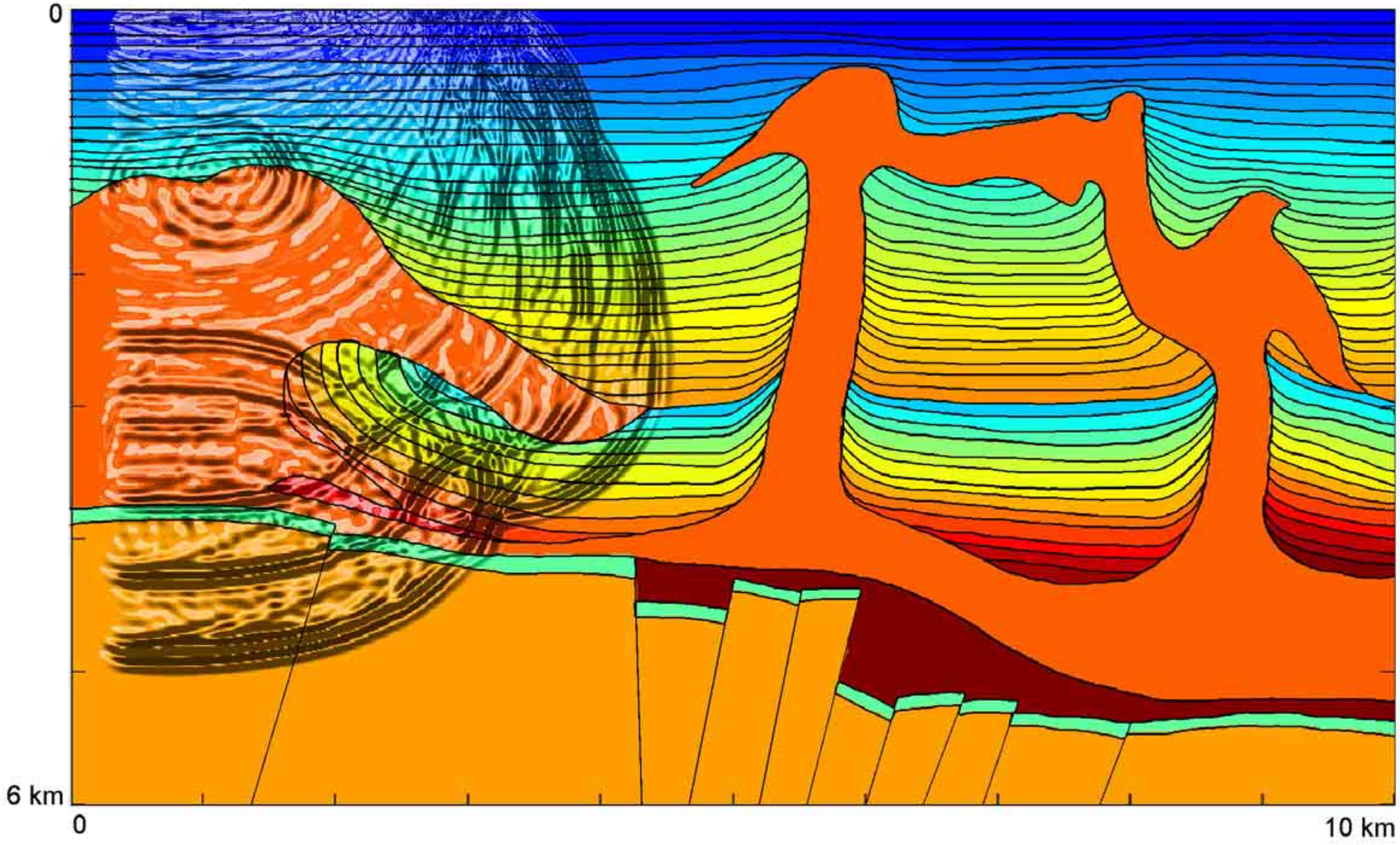

Figure 21. Finite-difference method allows us to see the propagation of waves in the subsurface..

CHAPTER IV

ANALYSIS OF RAW DATA

DATASET

Our resulting dataset is composed of 314 shots. 601 dual sensors, i.e. a geophone and a hydrophone, record each shot. Then the hydrophone produces pressure data; geophone produces two traces: the vertical and horizontal component of particle velocity. The acquisition technique therefore is 3-component Ocean Bottom Seismic (3C OBS). The listening time is 6 seconds.

The synthetic dataset is stored in SEGY format and will be available on the website of CASP consortium (http://casp.tamu.edu) for anyone who would like to test their Prestack Migration algorithms.

DEFINITION OF KEY REFLECTORS

Hydrocarbons in the North Caspian Basin are accumulated in *subsalt* paleoatoll carbonates and clastics, *suprasalt* clastics, and *nearsalt* clastics (Figure 22). Nearsalt hydrocarbons are trapped under salt overhangs. Subsalt oil deposits in carbonates are considered major accumulations (tens of billions of barrels), while suprasalt and nearsalt hydrocarbons are considered minor (hundreds of millions of barrels). Therefore subsalt paleoatoll carbonates are considered the main exploration targets. Accordingly, in this work we are focusing in the quality of imaging of subsalt carbonates and clastics overlaying carbonates. The age of carbonates is Middle Carboniferous to Upper

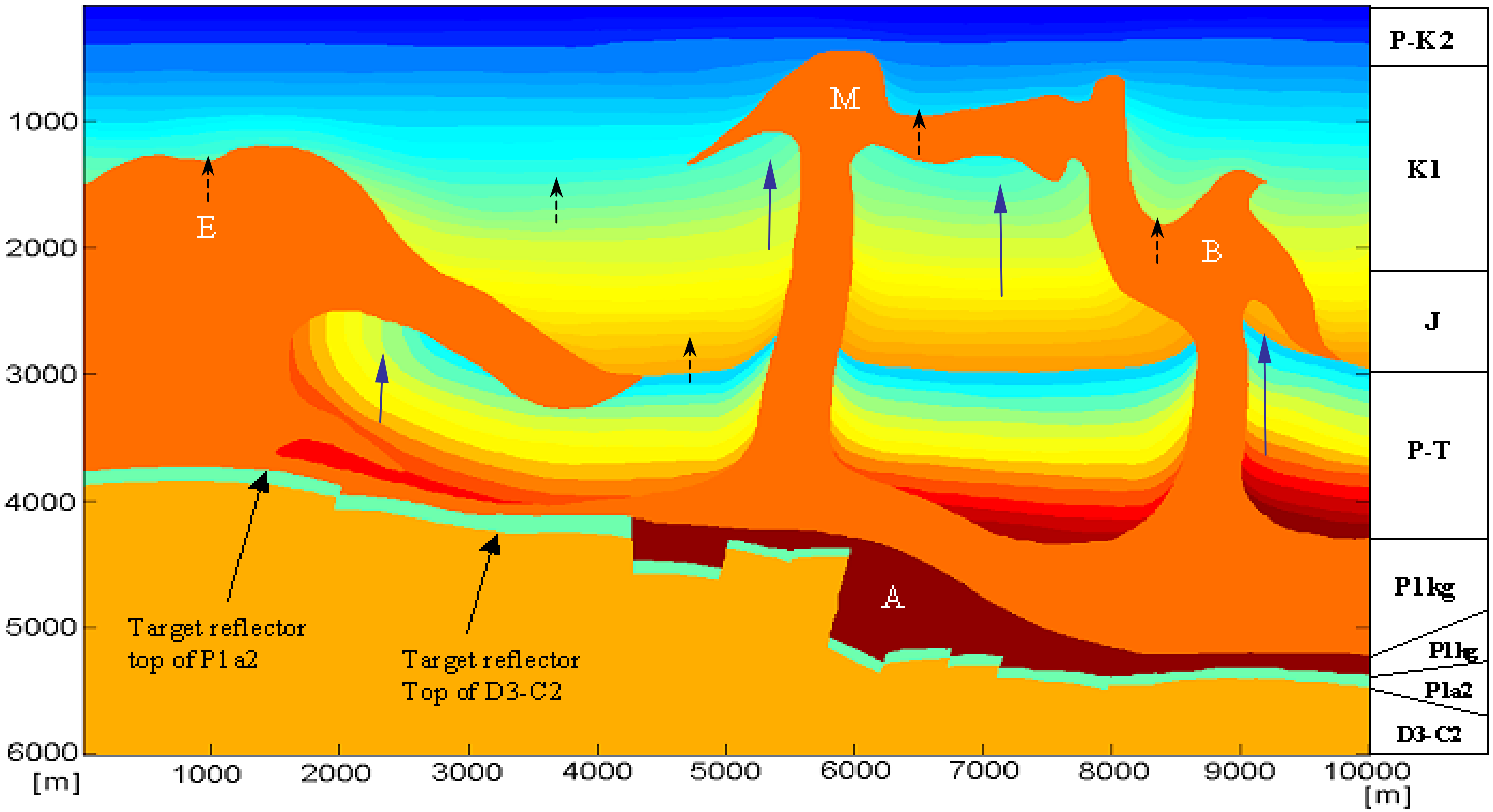

Figure 22. A geomodel showing geological ages of formations. Black continuous arrows indicate tops of a subsalt reservoir; dark blue arrows indicate near salt possible oil and gas accumulations; black dashed arrows indicate possible suprasalt accumulations of hydrocarbons. E – salt dome, M and B are salt diapirs, A – anhydrites.

Devonian (D3-C2). The age of clastics on top of carbonates is Lower Permian Upper Artinskian (P_1a^2). Further we call them target reflectors D3-C2 and P_1a^2 (Figure 23).

QUALITY OF IMAGING OF SUBSALT TARGETS

The effect of the overburden

The overburden can affect our ability to illuminate the target horizons. There is about 4 km thick overburden over our target reflectors D3-C2 and P1a2. Two questions can be posed: Do seismic waves have enough energy to reach the 4km deep exploration target? And do they have enough energy to get the information about the exploration target back to the surface?

Let us answer the first question first. Do seismic waves have enough energy to reach the 4km deep exploration target? One way of answering this question is to look at snapshots of wave propagation in the subsurface. Let us look at 5 snapshots made at different shot positions (Figures 23-27). They demonstrate that seismic waves indeed have enough energy at the depth of 4km and they do reach target horizons everywhere except under anhydrites in areas where anhydrites are under a halite diapir. The energy of seismic waves is decreasing dramatically when the wavefront goes through anhydrites to the reservoir rocks, which means that anhydrites are seriously affecting the quality of our target reflectors. We see that wavelength is substantially increasing in the halite (Figures 24-28). In the same figures we see the dramatic increase of wavelength in anhydrites, which causes it to not notice the top of carbonates.

The second question is: Do seismic waves have enough energy to get back to the surface? Let us look at shot gathers (shots 001, 081, 121, 161, 222, 241, 281, and 301). Reflections from tops of P_1a^2 and C_2-D_3 are indicated on shot gathers (Figures 29-36) Reflected energy is relatively low, therefore we applied automatic gain control and exponential amplitude gain. Our target reflectors P_1a^2 and C_2-D_3 are not seen well on the shot gathers from the right half of our model (shots from 150 through 314). There are two causes: deposits of anhydrites complicated with halite diapir on top of anhydrites and the interference with numerous events originated at the walls of halite diapirs (reflections, refractions, diffractions, converted waves, and their multiples).

It is also important to know that in the areas of development of salt diapirs and domes complicated with overhangs, we have not only diminished energy but also significant distortion of wavefronts. Snapshots (Figures 36-38) show that the morphology of salt diapirs and domes changes the shape and orientation of wavefronts reflected from top anhydrites and top Lower Permian clastics located between walls of two halite diapirs, distorting wavefronts beyond recognition. Figure 36 shows the shape of a wavefront at the point when it reached the target reflector and Figures 37 and 38 show the shape of the same event when it passed all the salt bodies on its way back. Interference of upcoming C_2-D_3 and P_1a^2 reflections from carbonates with both PP and PS diffractions and refractions from neighboring salt diapirs and domes is also distorting the image of subsalt clastics and carbonate deposits. The conclusion here is that in the subsalt we can predict the existence of a reflector, but cannot predict its shape. In other words we are likely to have a distorted image of a subsalt reflector.

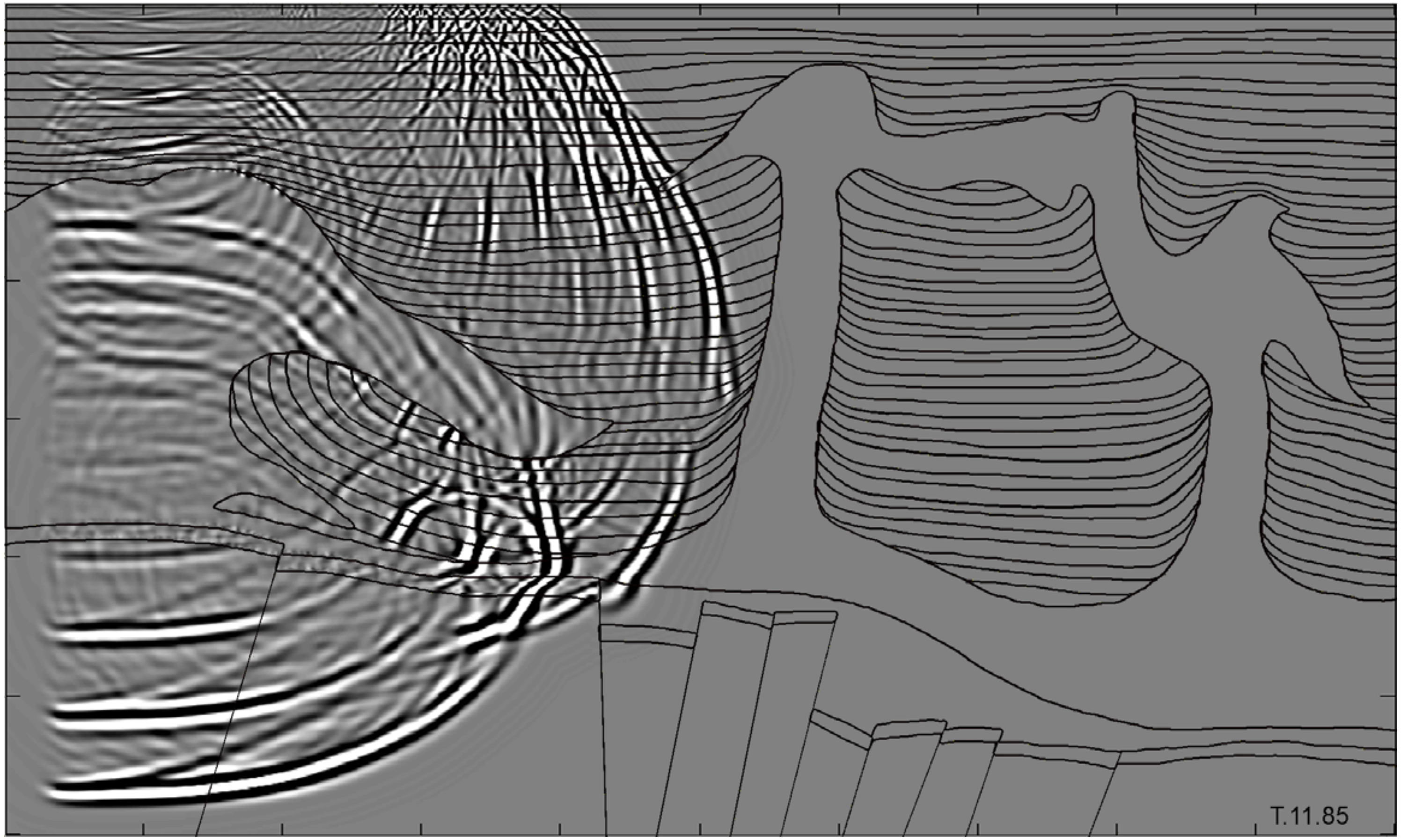

Figure 23. Snapshot of shot #11. We have enough energy to reach the carbonate reservoir and beyond despite the fact that reservoir is under a salt dome.

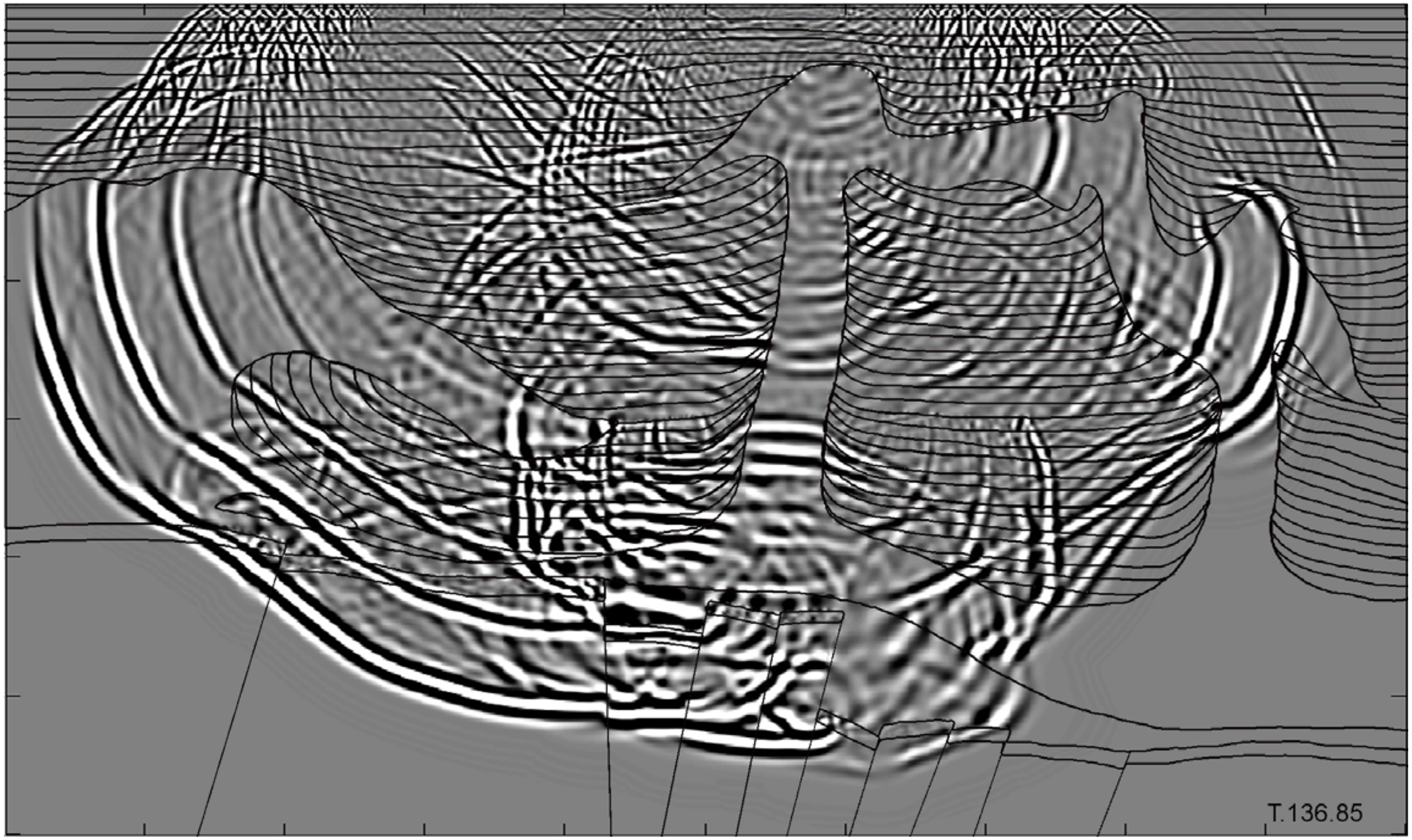

Figure 24. Snapshot of the shot #136 showing that we have enough energy to reach the subsalt except under anhydrites when the wavefront has to propagate, first, through the diapir, second, through anhydrites to reach the target reflector.

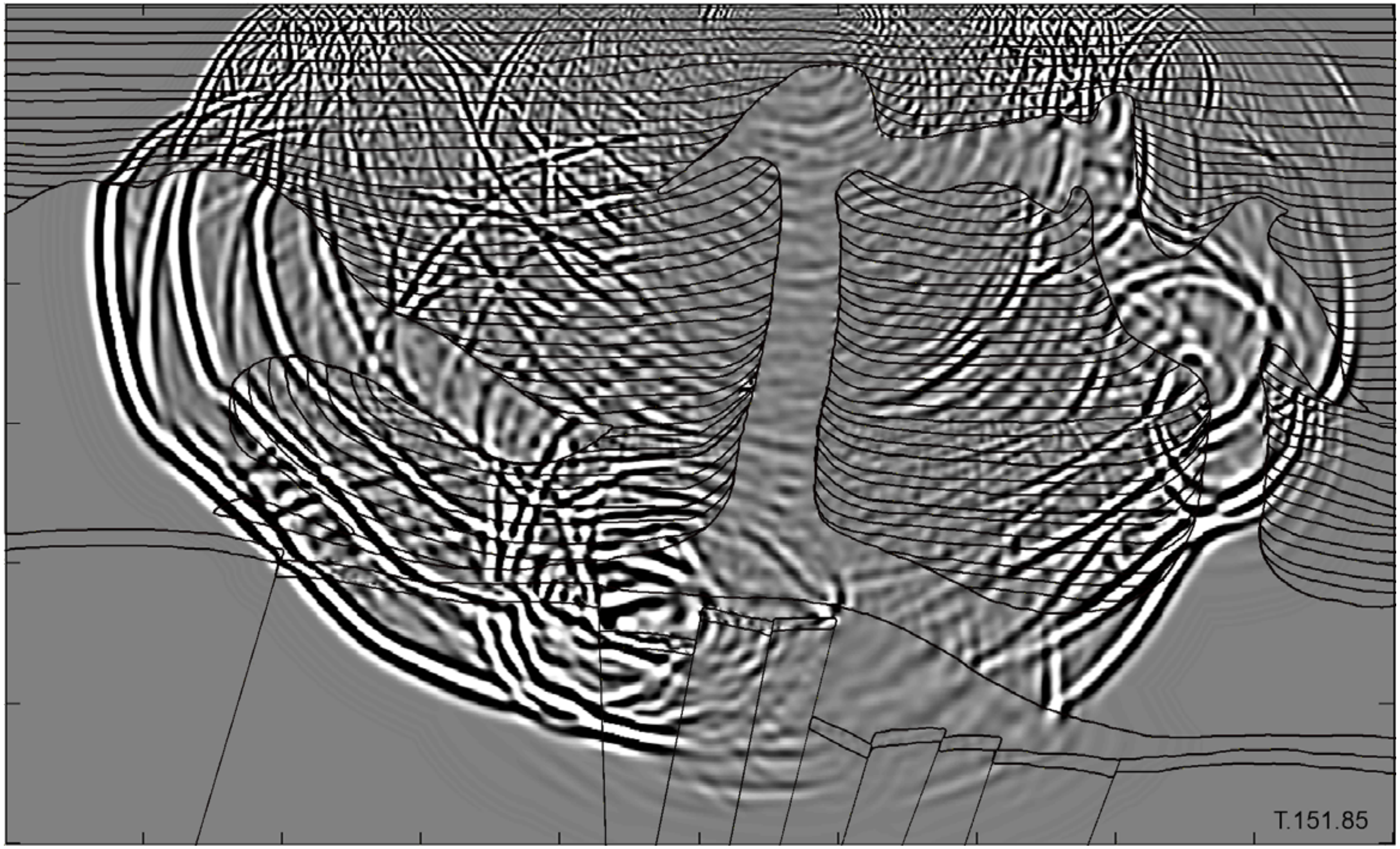

Figure 25. Snapshot of shot #151 demonstrates that we have enough energy to reach subsalt reservoirs everywhere except under the anhydrites when the wavefront has to propagate, first, through the diapir, second, through anhydrites to reach the target reflector.

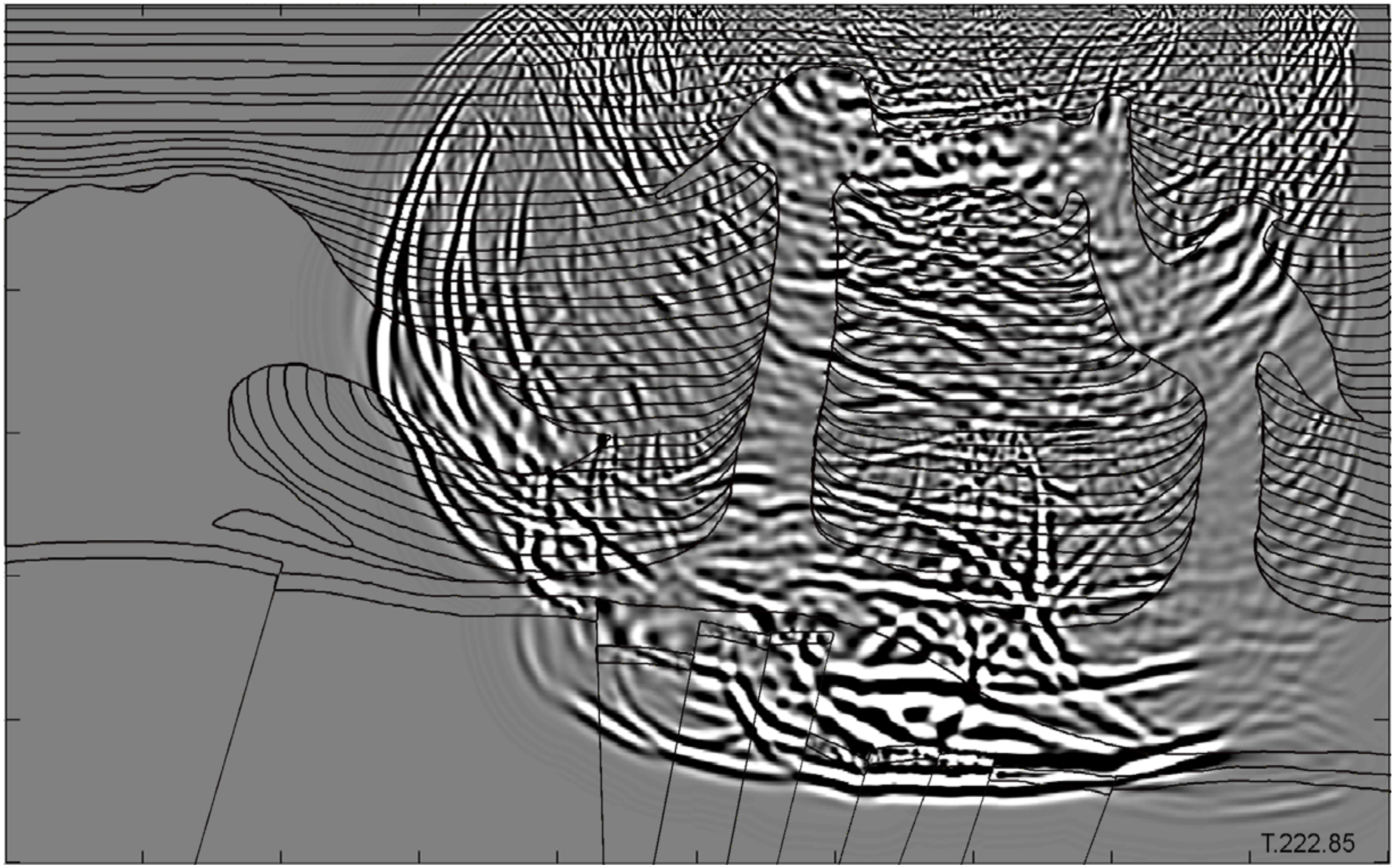

Figure 26. Snapshot of shot #222 demonstrates that we have enough energy to reach subsalt reservoirs everywhere, even under the anhydrite, because this time the wave propagates through clastics, not a salt diapir, to reach anhydrites.

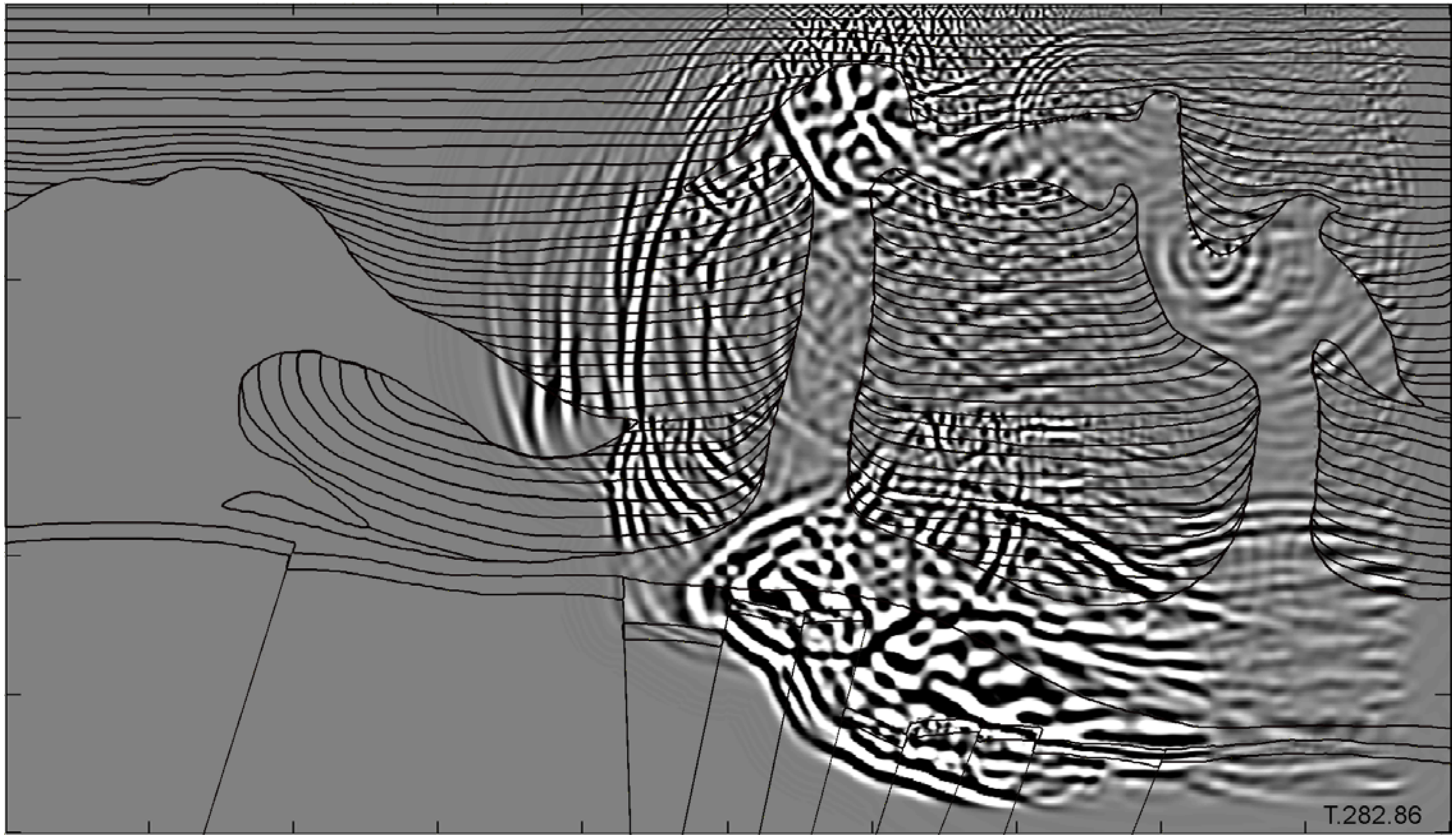

Figure 27. Snapshot of shot #282 demonstrates that we have enough energy to reach subsalt reservoirs everywhere, even under anhydrite, because this time the wave propagates through clastics, not a salt diapir, to reach the anhydrites.

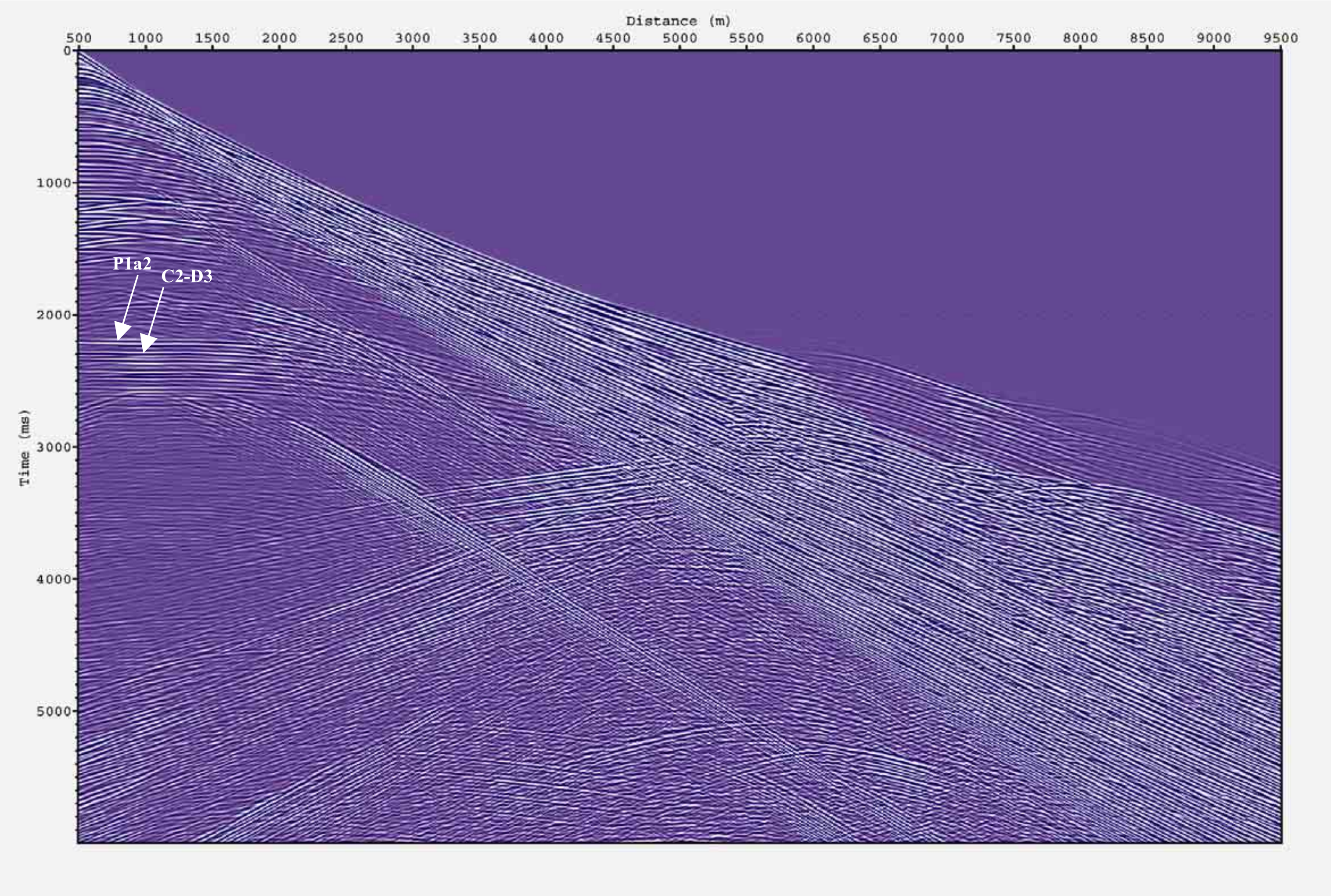

Figure 28. Shot 001, pressure. Exp. Gain, AGC=90. Reflections from top P1a2 and C2-D3 target formations are indicated.

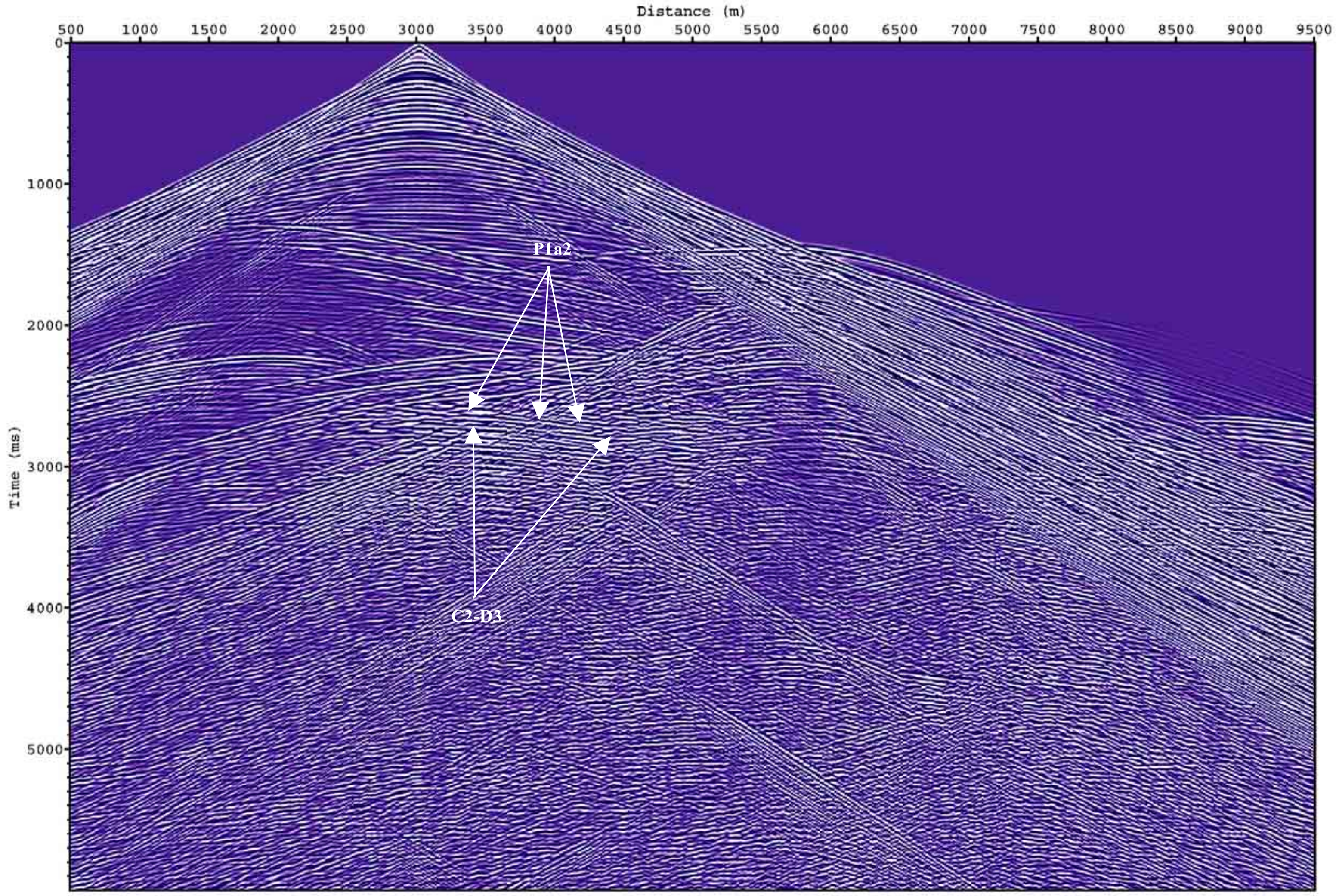

Figure 29. Shot 081, pressure. Exp. Gain, AGC=90. Reflections from top P1a2 and C2-D3 target formations are indicated.

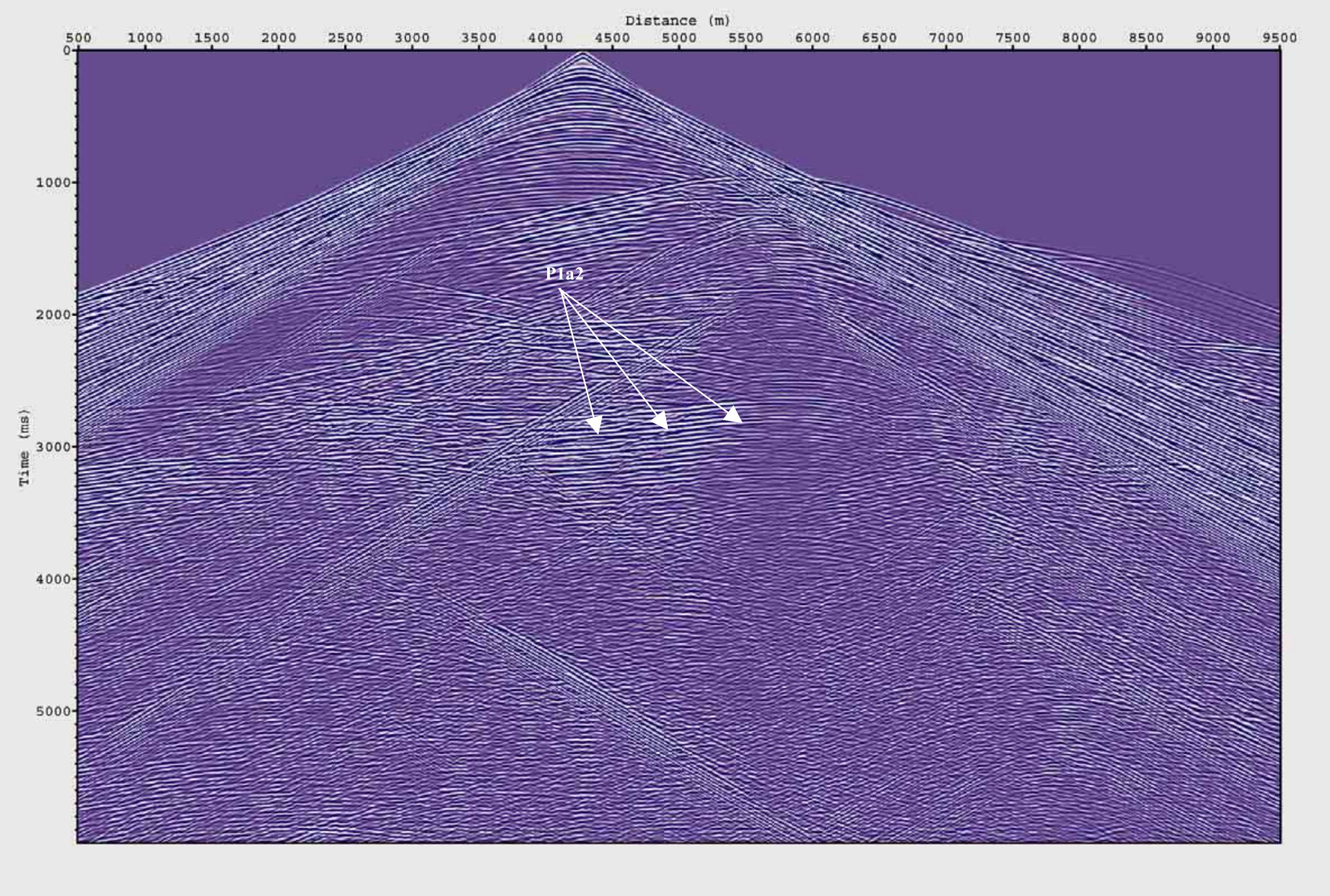

Figure 30. Shot 121, pressure. Exp. Gain, AGC=90. We can see only one target horizon P1a2.

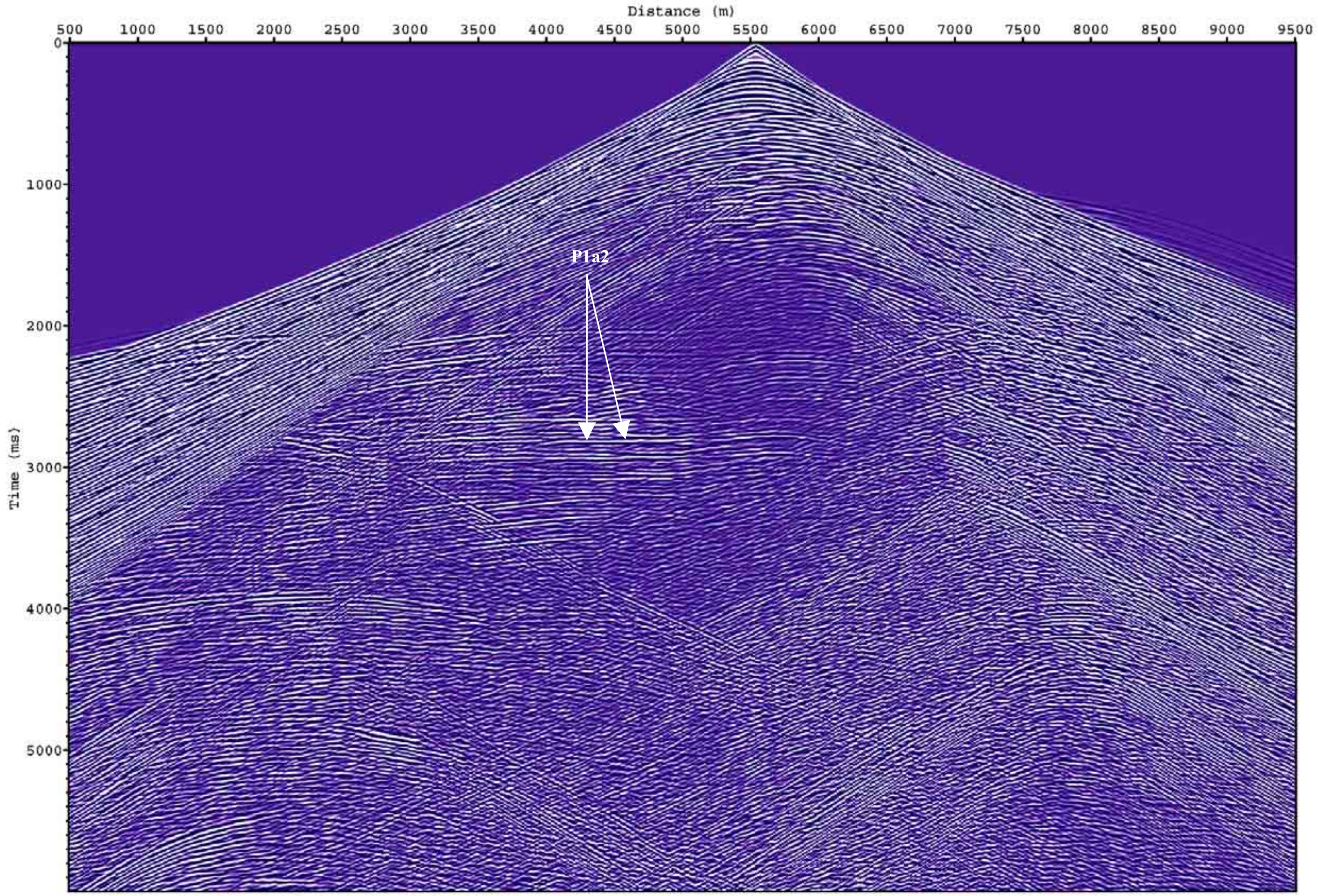

Figure 31. Shot 161, pressure. Exp. Gain, AGC=90. Only P1a2 target horizon is visible.

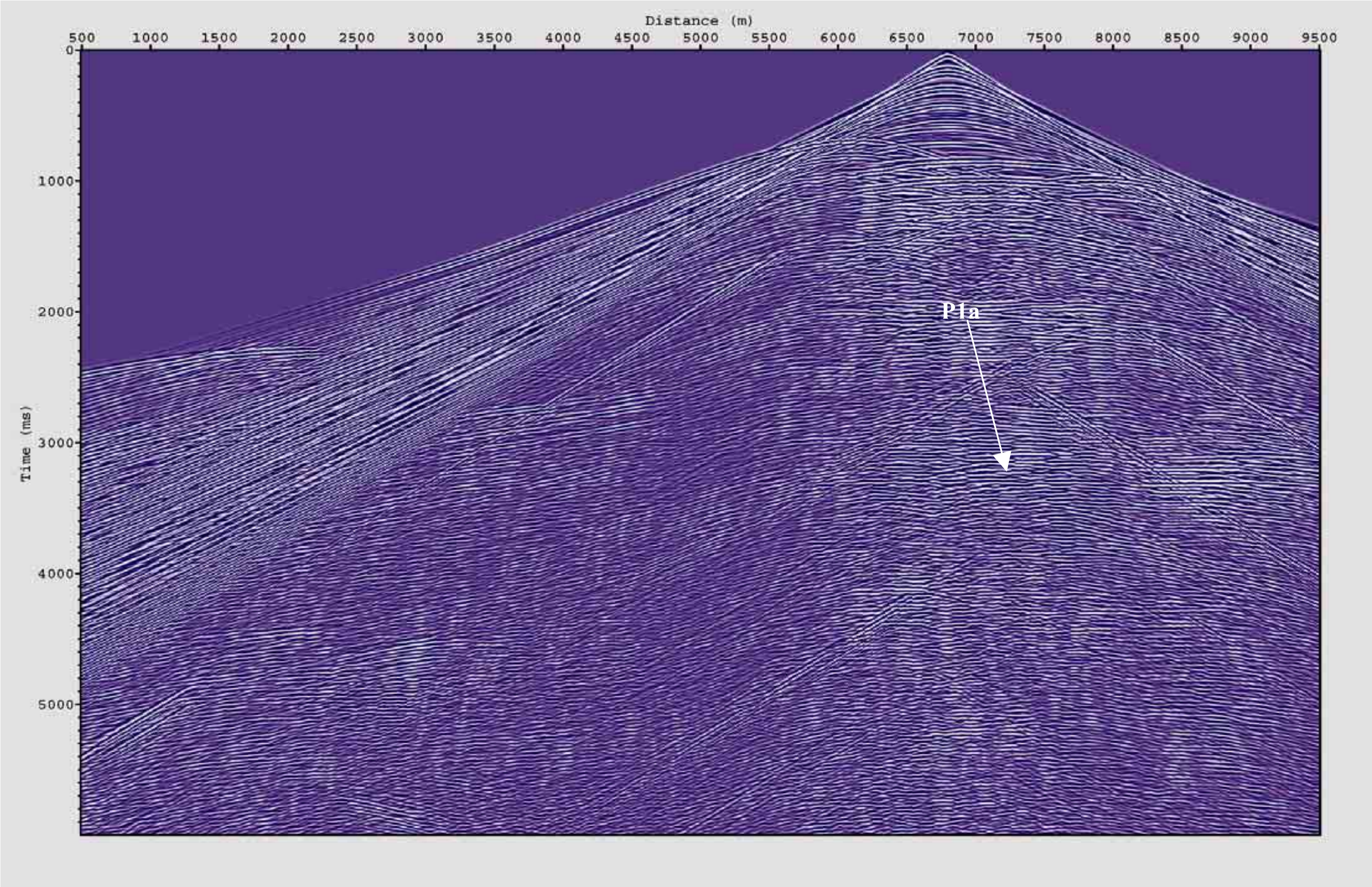

Figure 32. Shot 222, pressure. Exp. Gain, AGC=90. Our target reflectors P1a2 and C2-D3 are not seen well on the shot gathers from the right half of our model (shots 150 through 314).

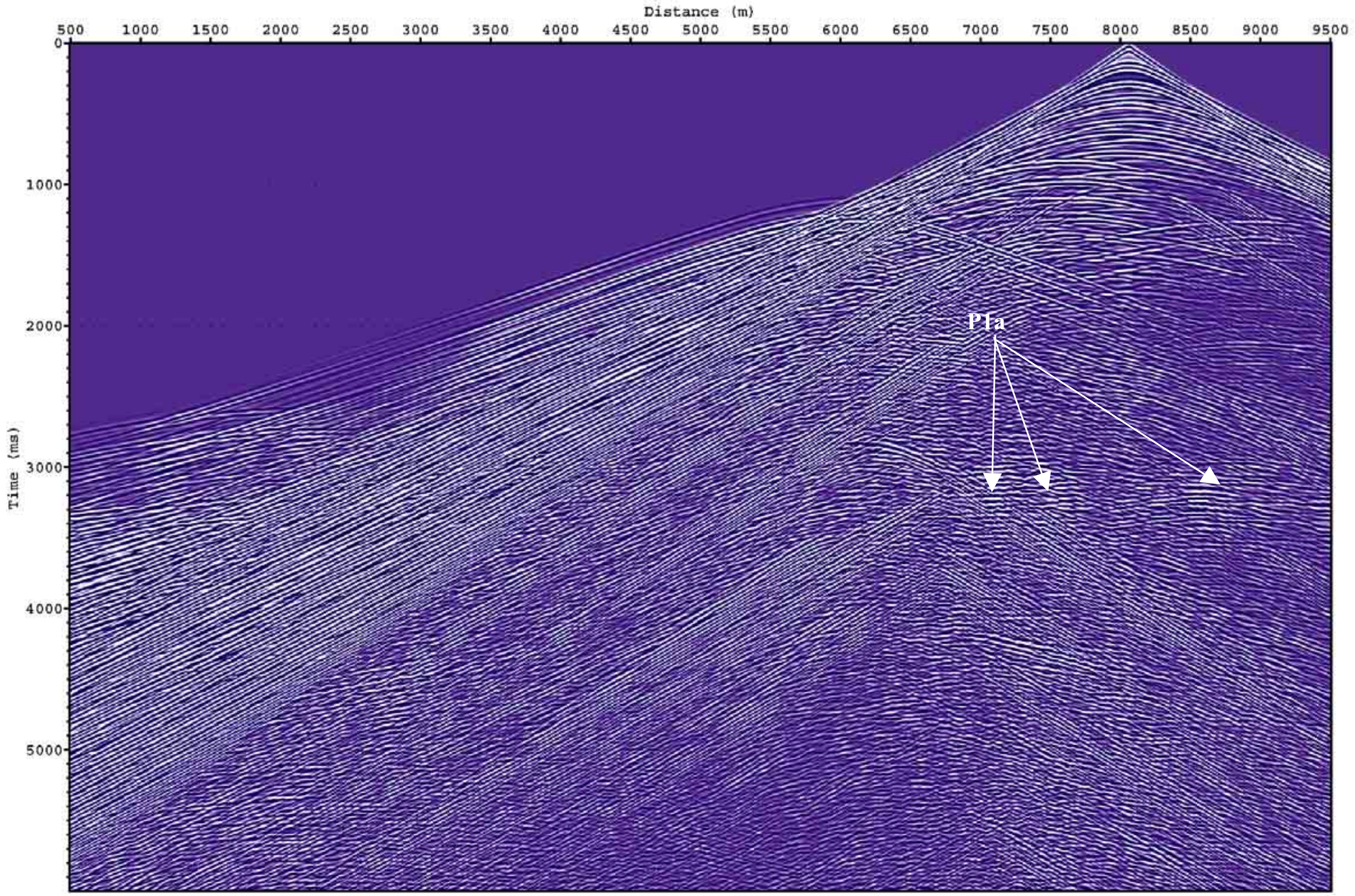

Figure 33. Shot 241, pressure. Exp. Gain, AGC=90. Our target reflectors P1a2 and C2-D3 are not seen well on the shot gathers from the right half of our model (shots 150 through 314).

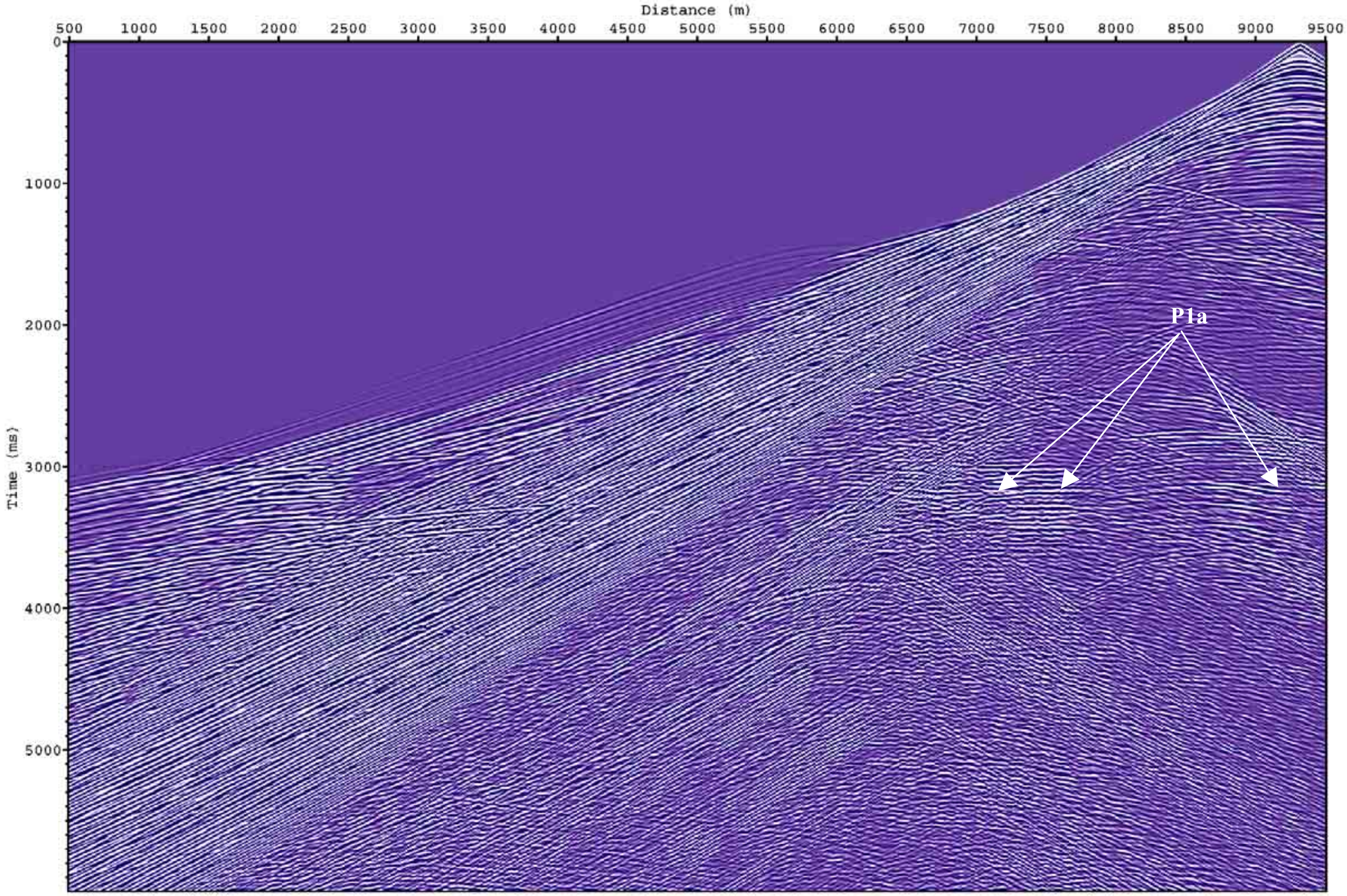

Figure 34. Shot 281, pressure. Exp. Gain, AGC=90. Our target reflectors P1a2 and C2-D3 are not seen well on the shot gathers from the right half of our model (shots 150 through 314).

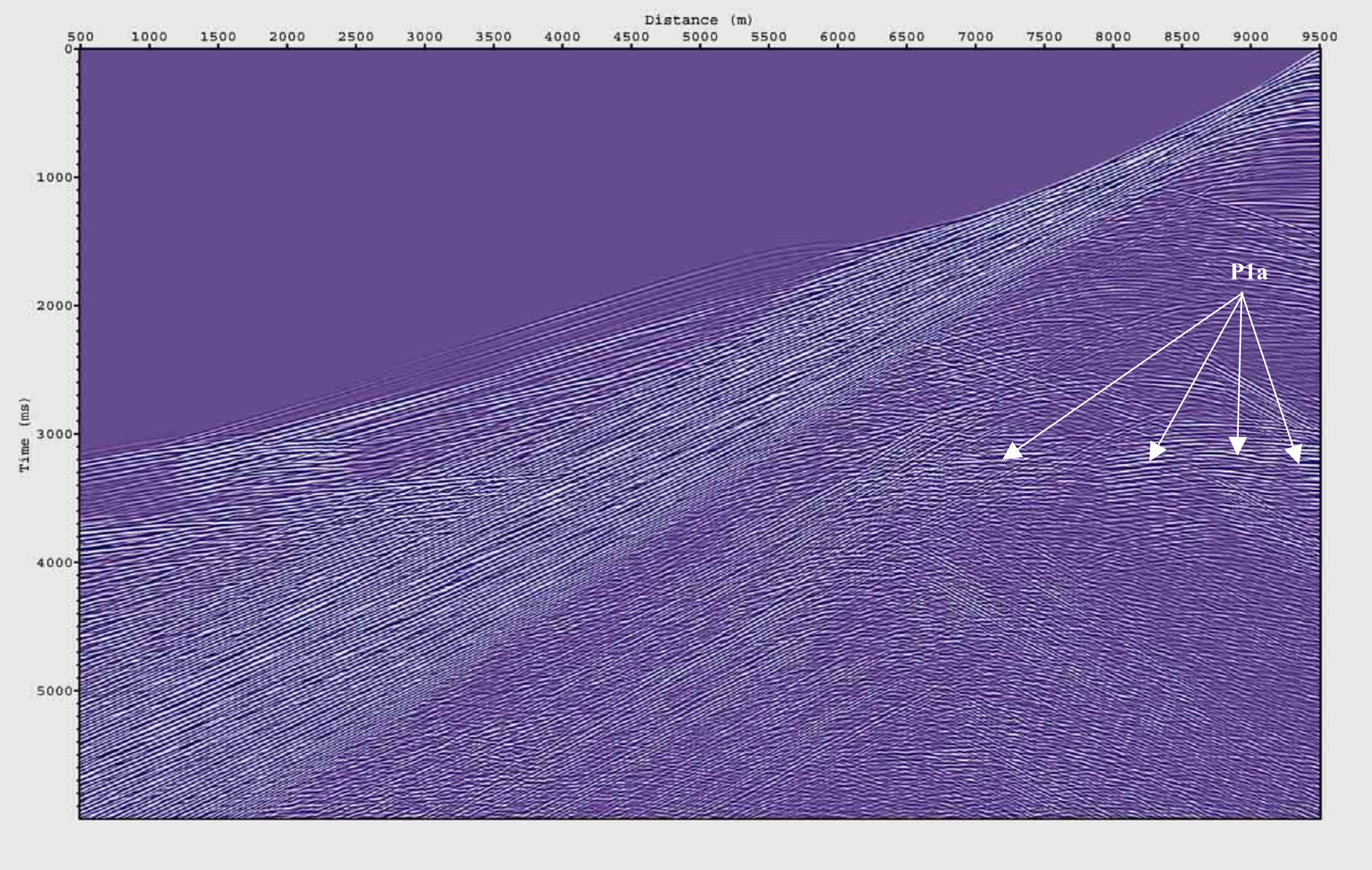

Figure 35. Shot 301, pressure. Exp. Gain, AGC=90. Our target reflectors P1a2 and C2-D3 are not seen well on the shot gathers from the right half of our model (shots 150 through 314).

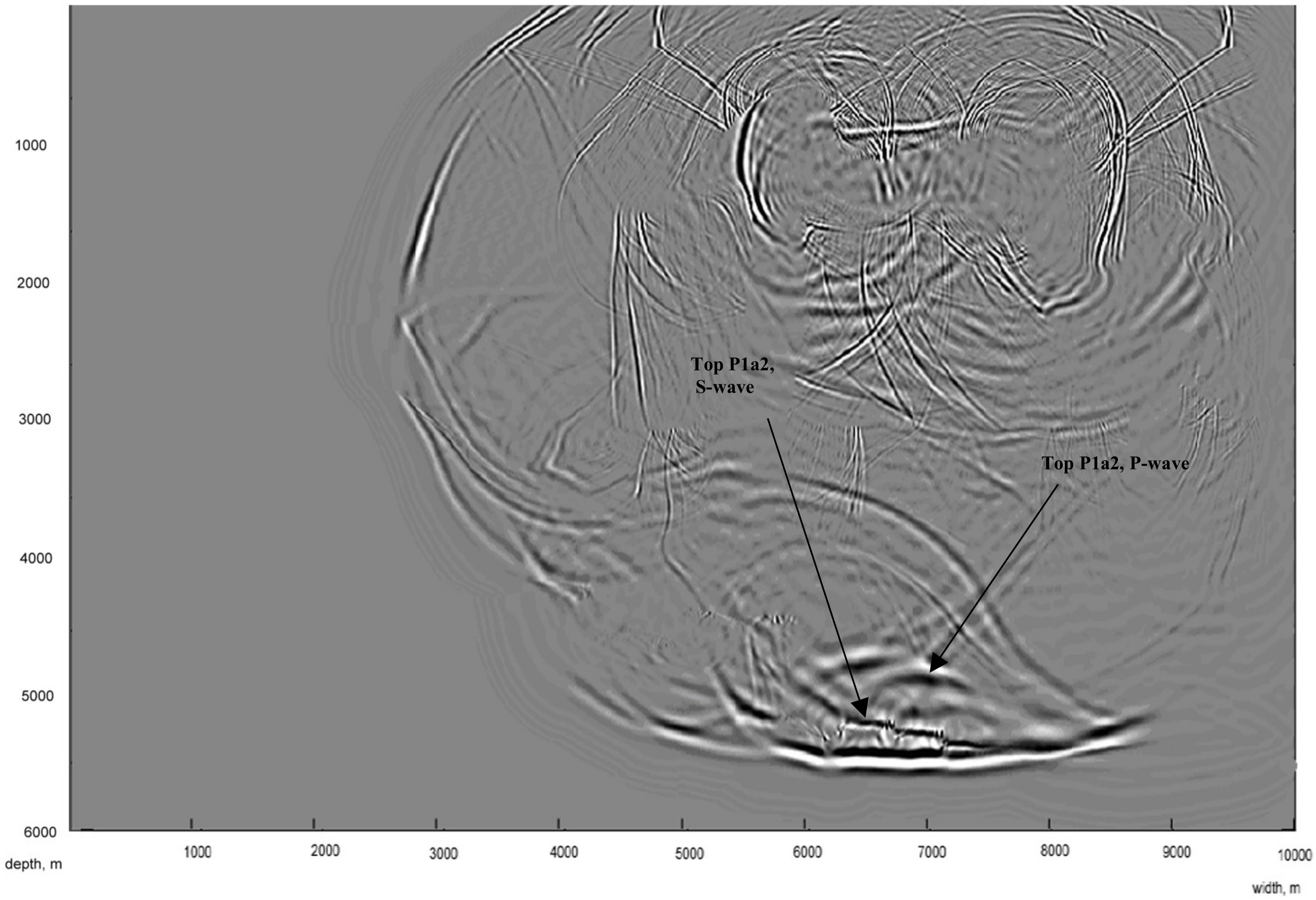

Figure 36. Snapshot where reflected P and S waves from top P1a2 clastics display relative conformity with the reflector shape.

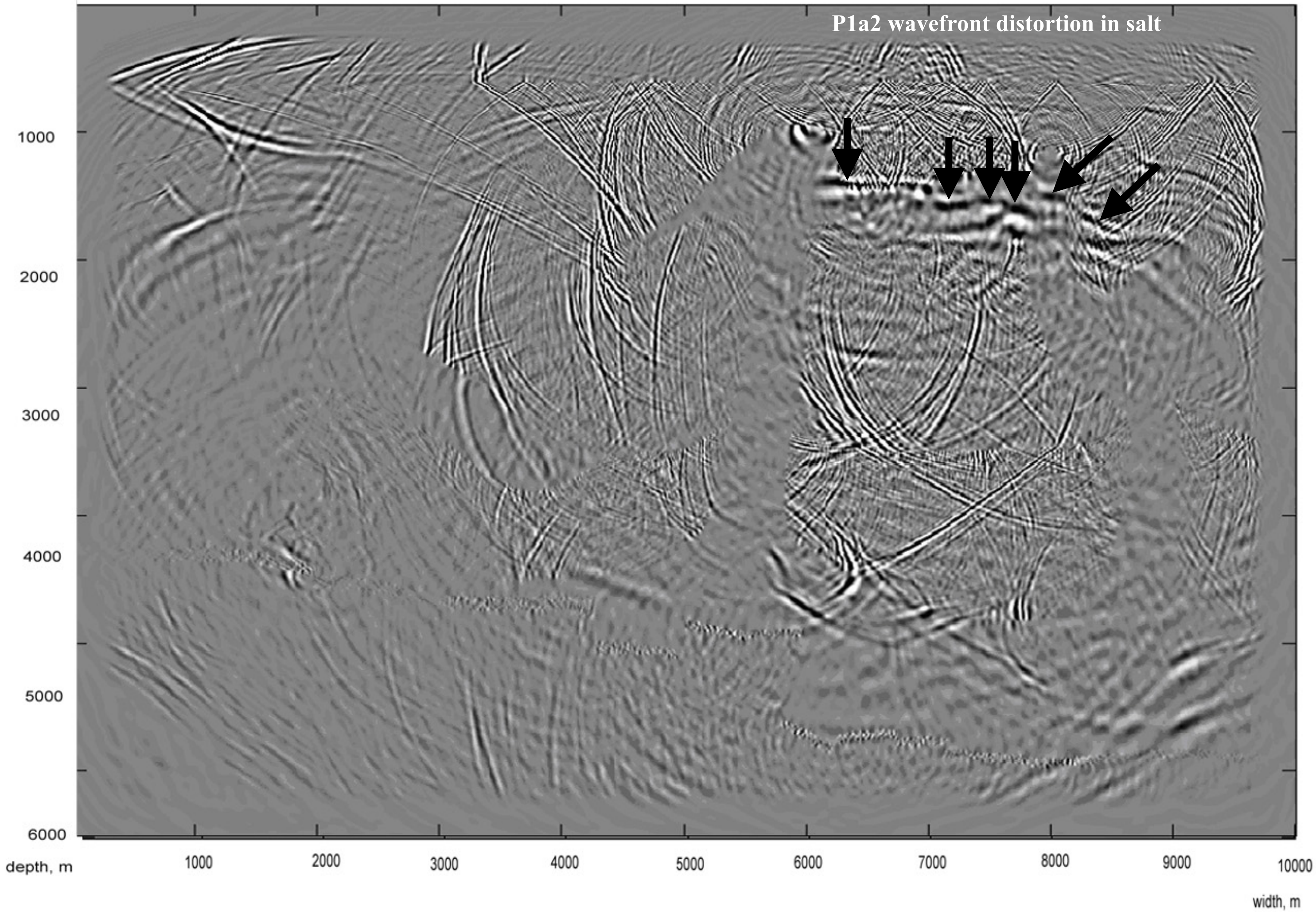

Figure 37. Snapshot demonstrating P-wave wavefront distortion of P1a2 reflection in salt. We do not see S-wave reflection.

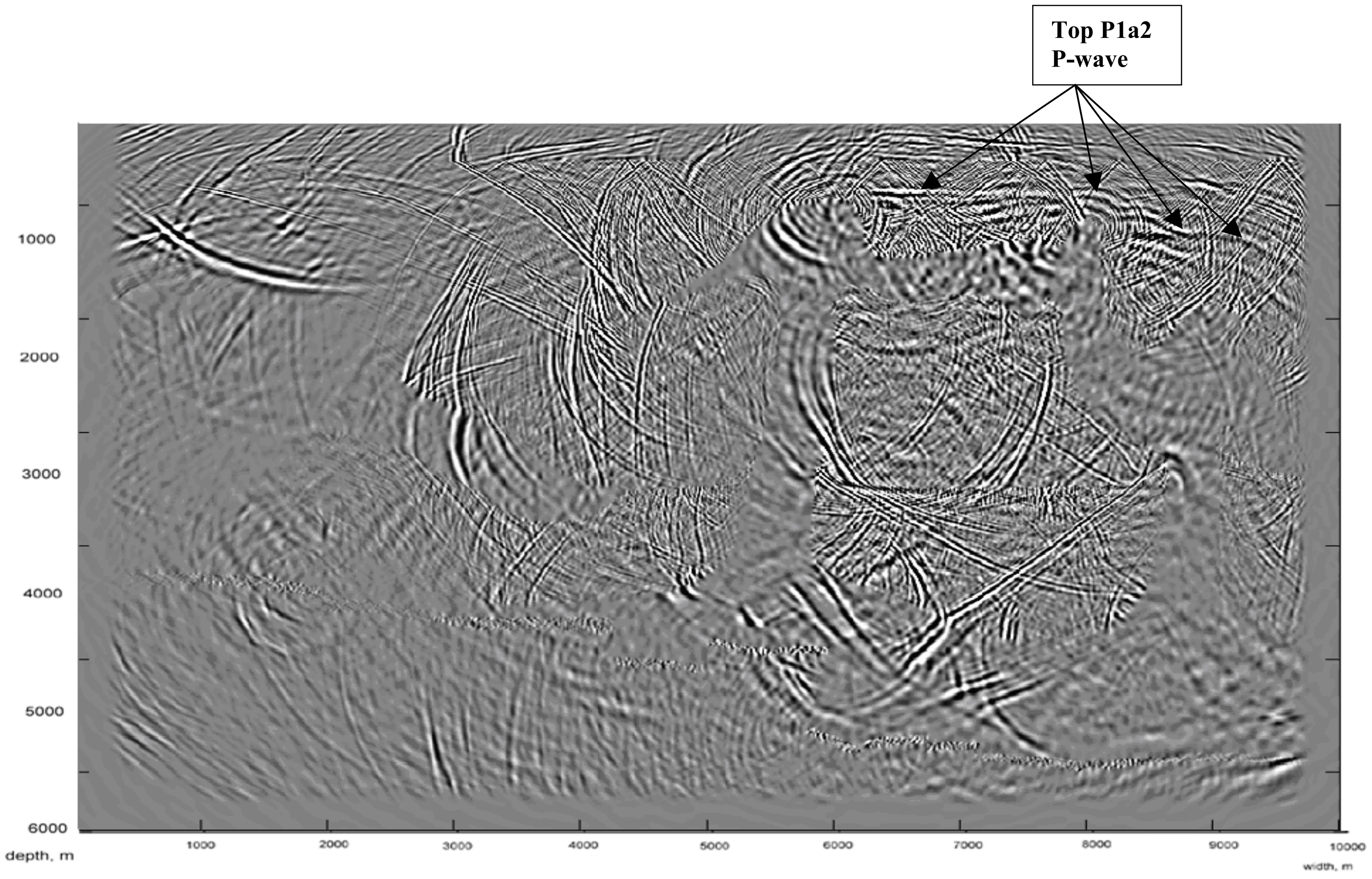

Figure 38. Snapshot showing top P1a2 clastics P-wave reflection. There is no S-wave P1a2 reflection.

Guided waves

Strong guided waves are produced mostly by the water layer. They result from a very shallow source in the water that allows rays to reach the critical angle very quickly. Figure 39 shows the extent of guided waves in the shallow water layer and shallow clastic layers. Figure 40 shows the same shot gather after shallow water guided waves were removed. In Figure 40 we do not apply exponential amplitude gain or AGC because the guided waves in our case are very intense. Our target reflectors are weak because guided waves trap substantial amounts of energy.

Near offset is critical for imaging our structures. But far offset is also significant, because it also carries information about the subsurface. Far offset becomes vital when we have a salt dome or a diapir in the near offset. That necessitates the removal of guided waves.

AVO analysis also requires information from large offsets, again necessitating the removal of guided waves. When we remove guided waves and, subsequently, the multiples our target reflectors are defined better and have more energy. Compare figures, which have guided waves with figures where guided waves were removed.

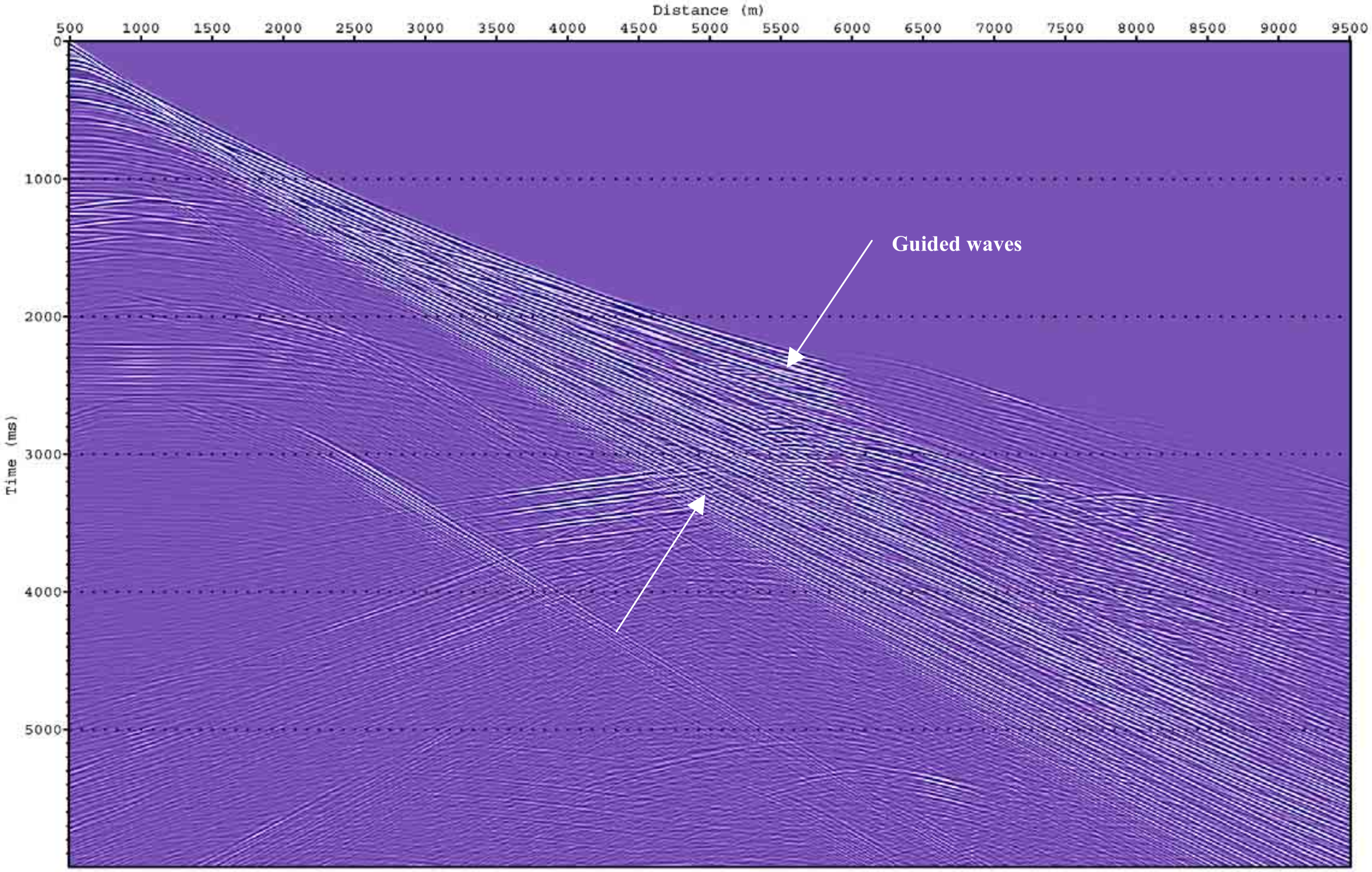

Figure 39. Shot 001, pressure, AGC=99. The extent and intensity of guided waves obstructing useful reflections. Compare with the figure 40, where guided waves were removed.

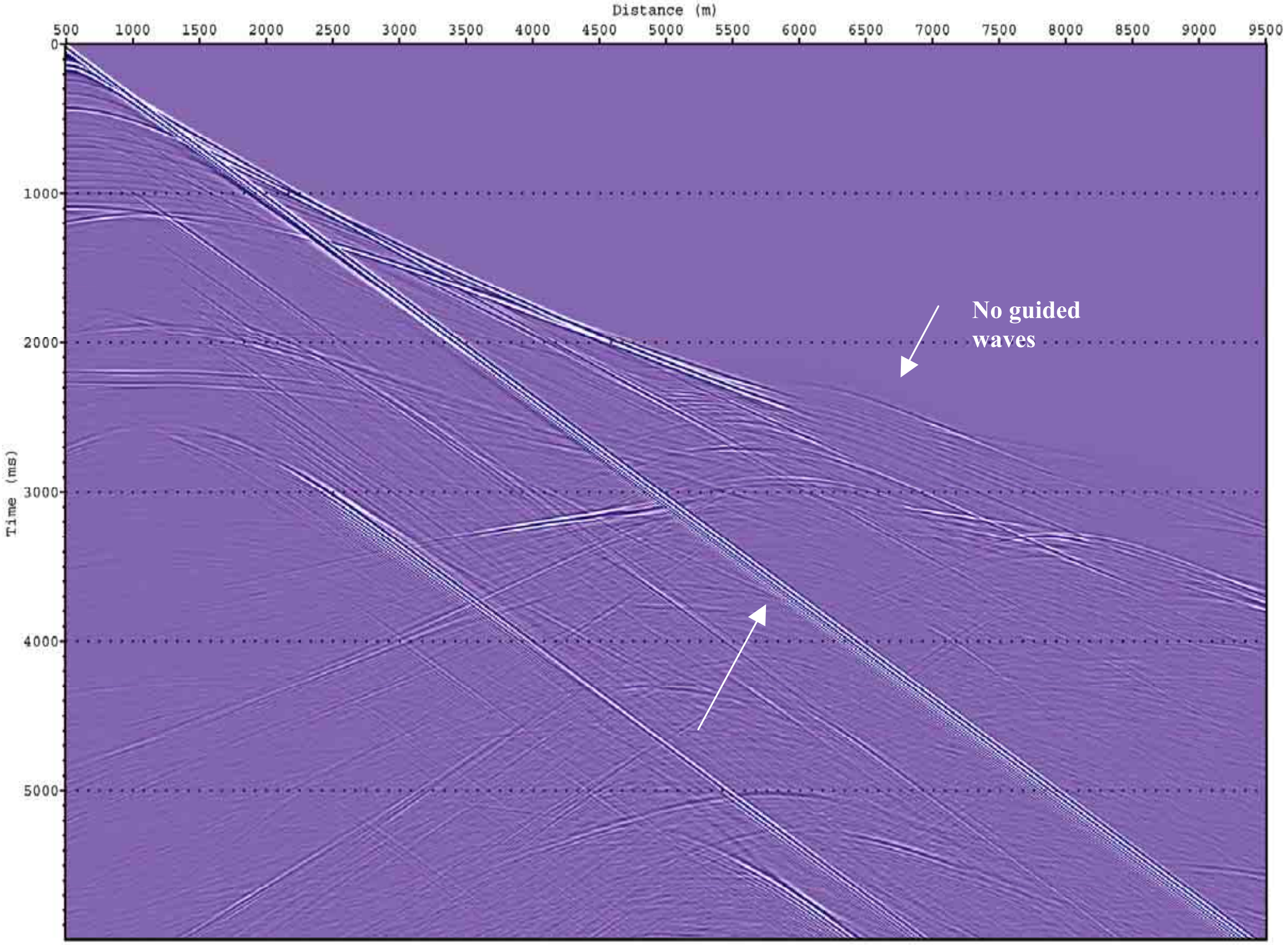

Figure 40. Shot 001, pressure, absorbing free surface, AGC=99. Guided waves are removed.

Multiple waves

Free surface multiples from the surface of the water are also an obstacle on our way to clearly image subsalt exploration targets. In the Figures 41-46 we illustrate the degree of influence of free surface peg-leg multiples on our data. Snapshots (Figures 47-48) demonstrate how free surface peg leg multiples interfere with target reflection from top P1a2 clastics. There are white areas on these shot gathers where the P-wave is not giving us any information about the morphology of the salt. The next section will consider the role of converted waves in the salt delineation. It is very important to remove multiples in order to be able to image subsalt target reflectors. The method of hydrophone and vertical geophone data summation to remove the water layer reverberations and receiver ghosts is also developed by Dr. Ikelle (Ikelle, 1999b).

Turning waves

The problem of near-diapir reflectors and the delineation of salt walls themselves can be resolved by exploding the seismic source far from salt diapirs (Figure 49).

Let us consider the case of positioning the explosion of the source away from top salt (wide aperture survey). P-waves would be able to approach diapir stems at angles less than critical. These waves would reflect off diapir stems as P-waves, hit the horizontal reflector near salt, reflect off that horizontal reflector, and record on a geophone or hydrophone. Thus the ray “returns” to the surface with information about the salt stem and about reflectors pinching out at the salt stem. The method of “turning waves” is developed by Dr. Ikelle (Ikelle, 2004). This is the way to image salt stems and

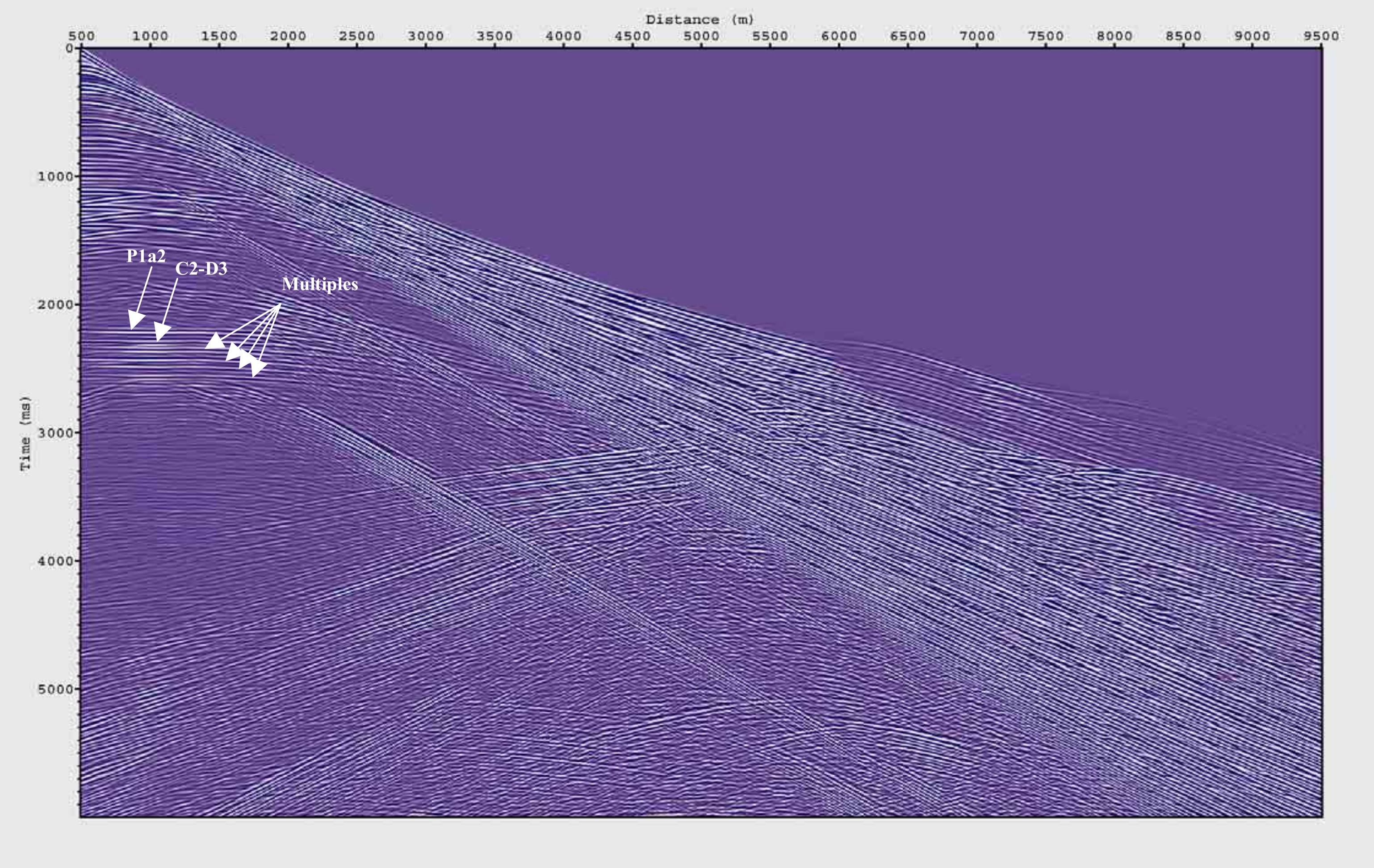

Figure 41. Shot 001, pressure. Exp. Gain, AGC=90. Shot gather with free surface and near surface multiples of target reflectors P1a2 and C2-D3.

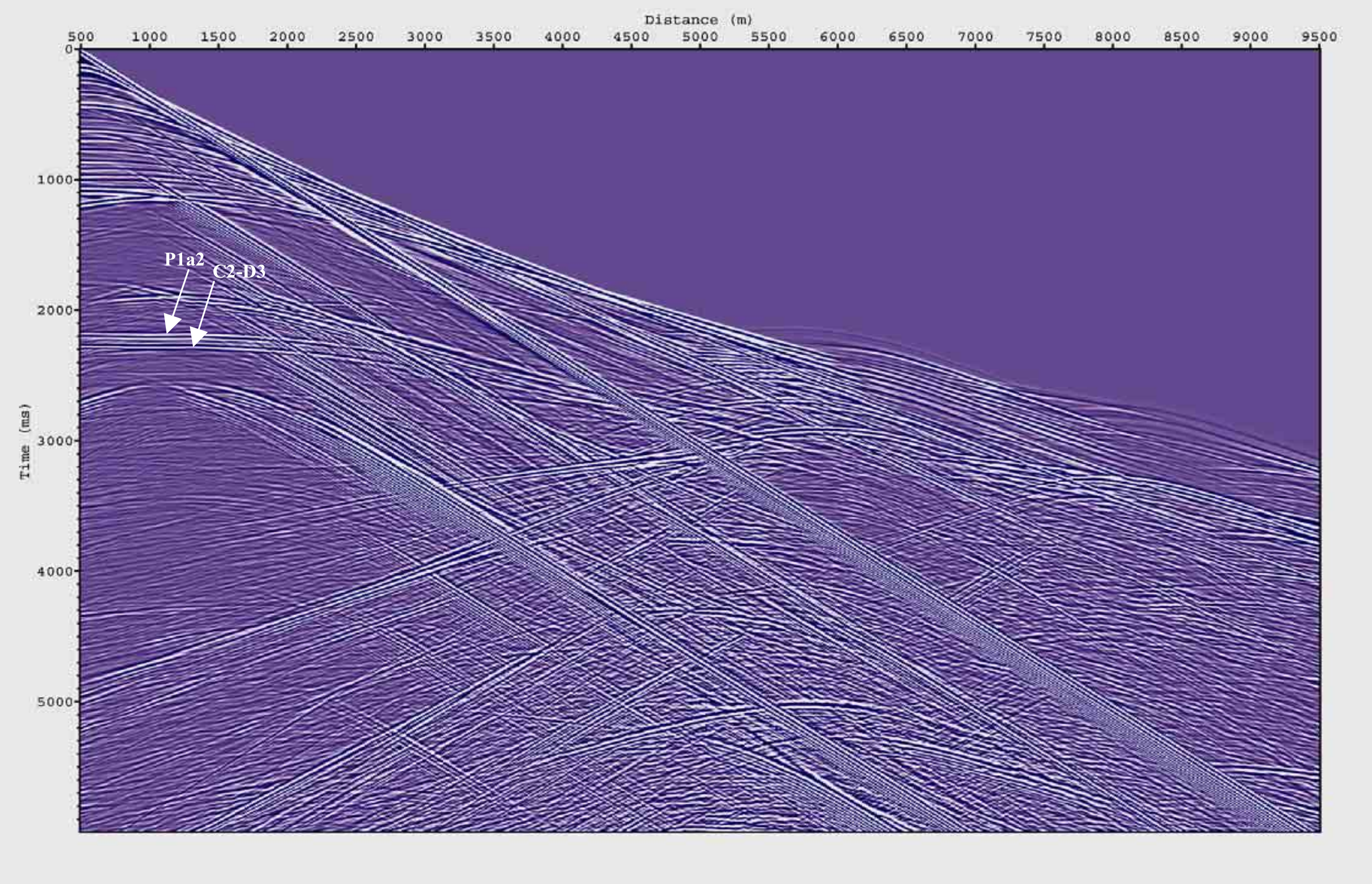

Figure 42. Shot 001, pressure. Exp. Gain, AGC=90. Shot gather with removed free surface and near surface multiples of target reflectors P1a2 and C2-D3.

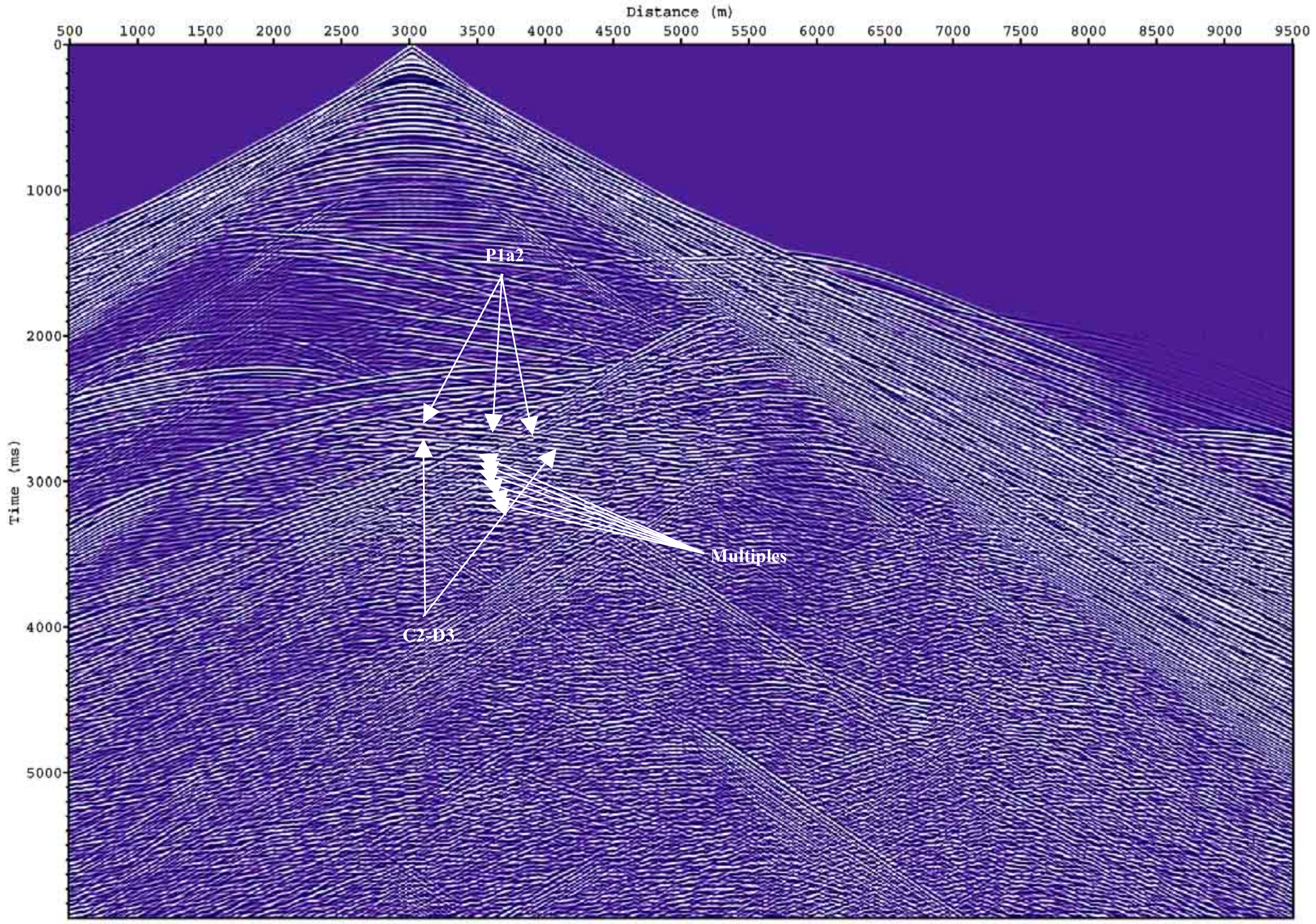

Figure 43. Shot 081, pressure. Exp. Gain, AGC=90. Shot gather with free and near surface multiples.

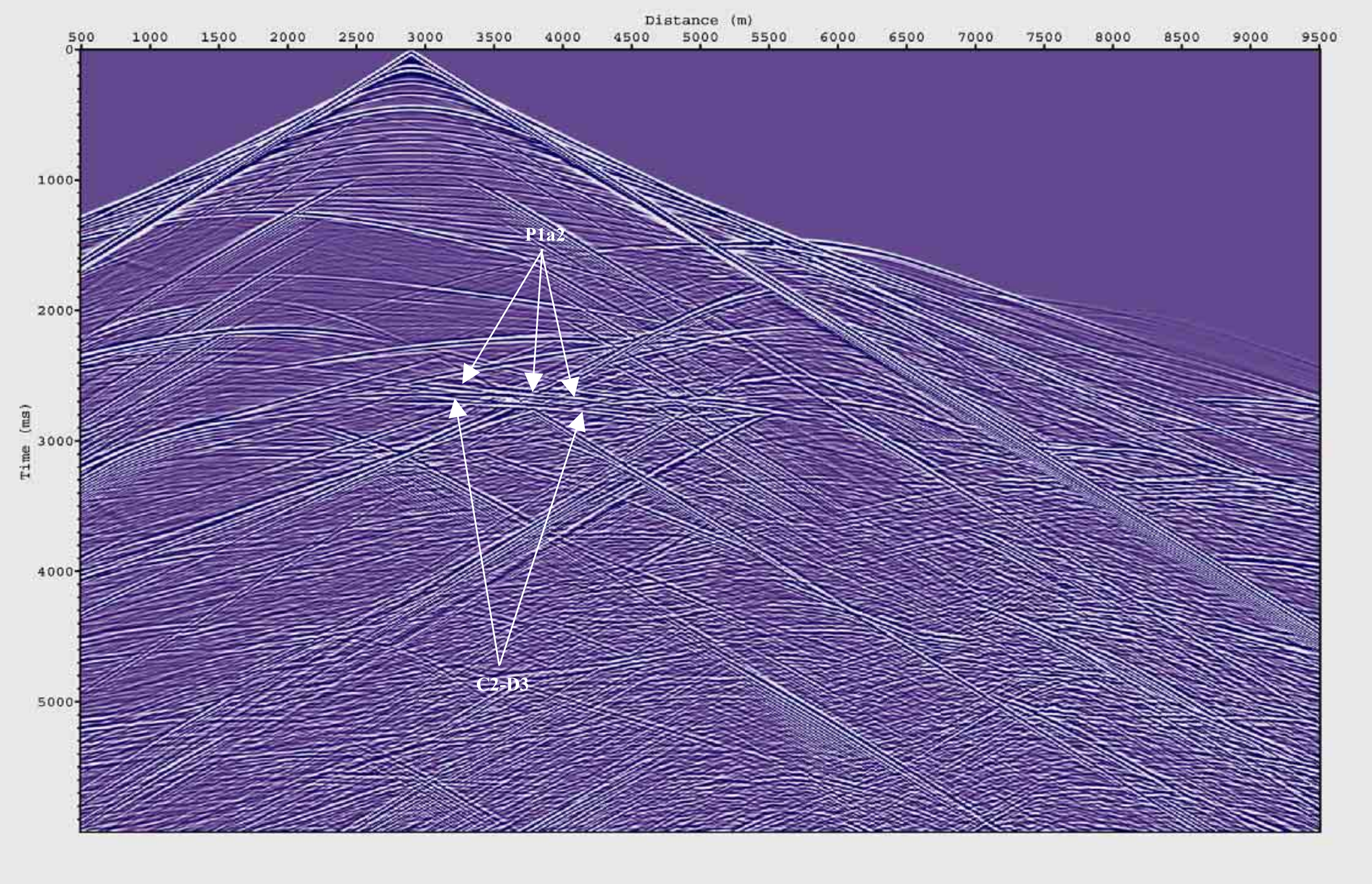

Figure 44. Shot 081, pressure. Exp. Gain, AGC=90. Shot gather without free surface and near surface multiples. Notice how much easier it is to see target reflectors P1a2 and C2-D3.

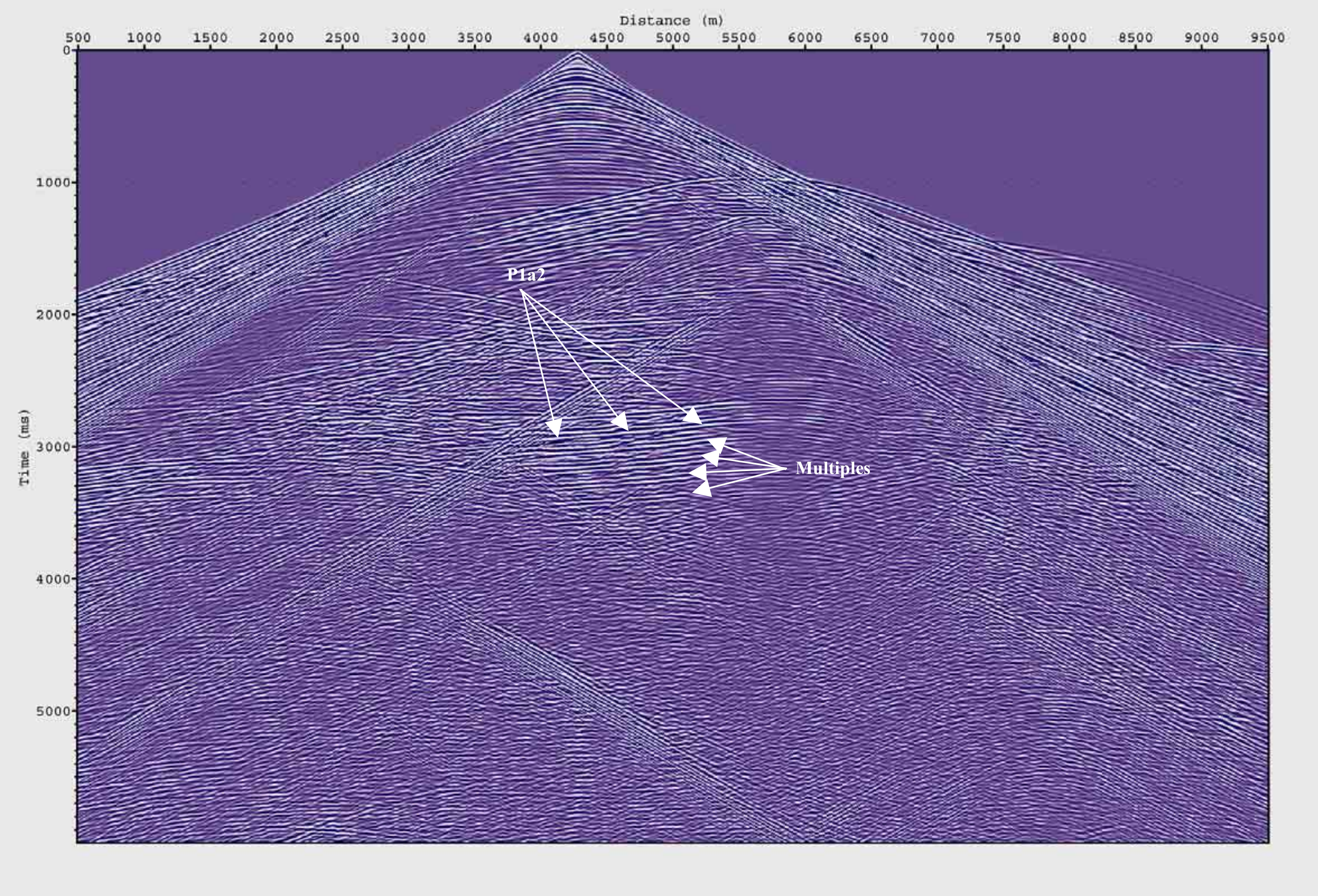

Figure 45. Shot 121, pressure. Exp. Gain, AGC=90. Shot gather with free surface and near surface multiples.

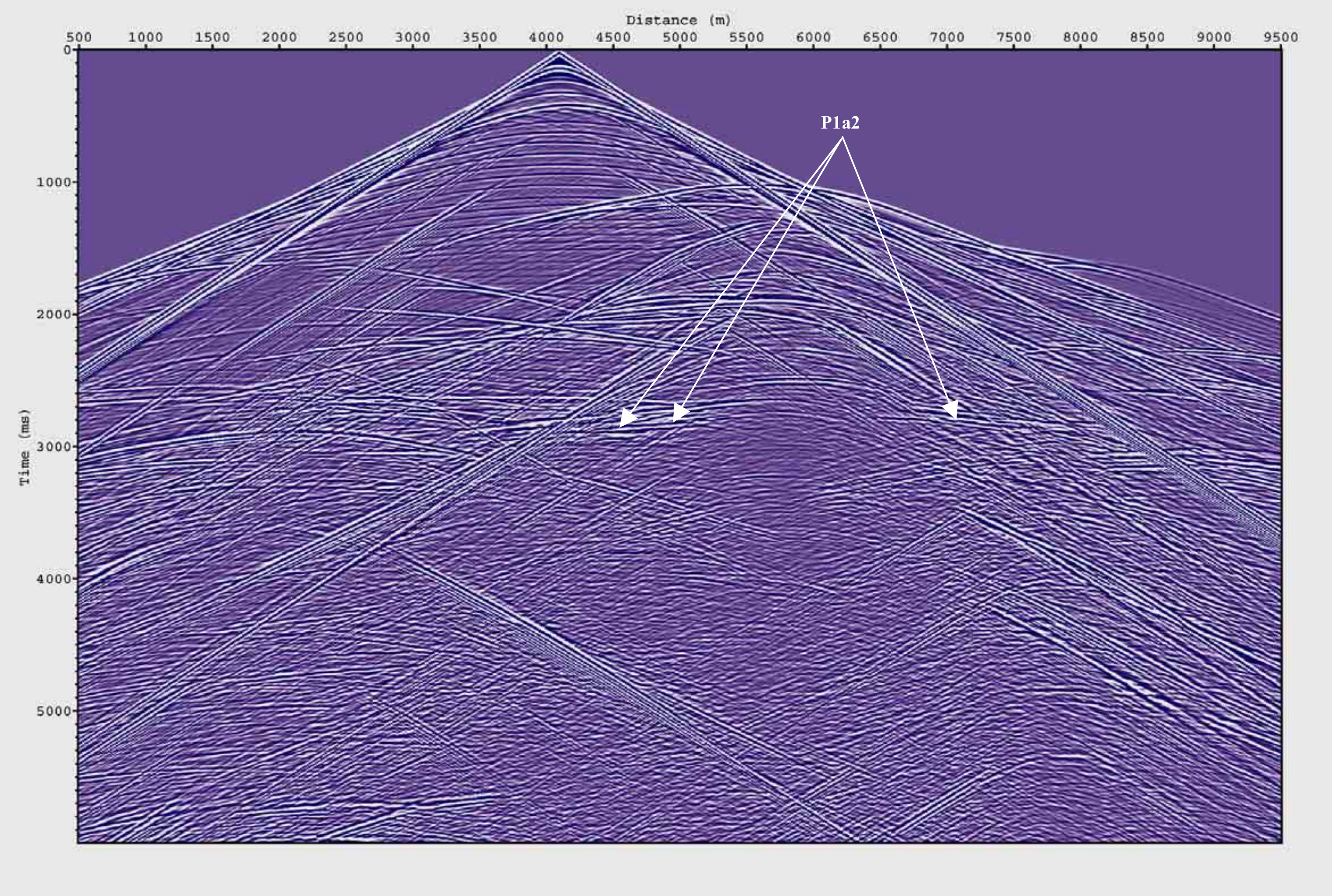

Figure 46. Shot 121, pressure. Exp. Gain, AGC=90. Shot gather with removed free surface near surface multiples.

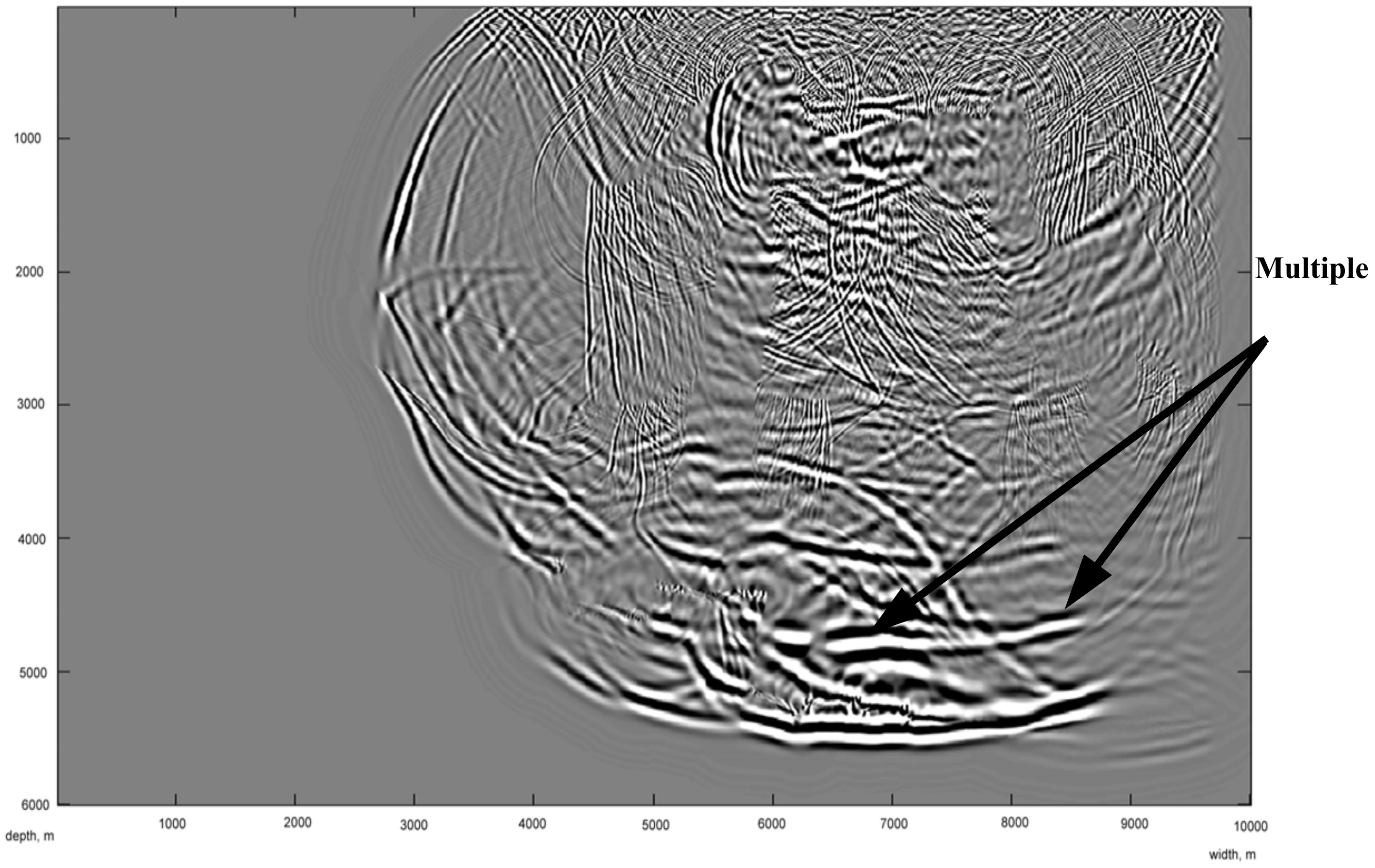

Figure 47. Snapshot at timestep 85. Free surface multiples interfering with reflections from target reflectors P1a2 and C2-D3.

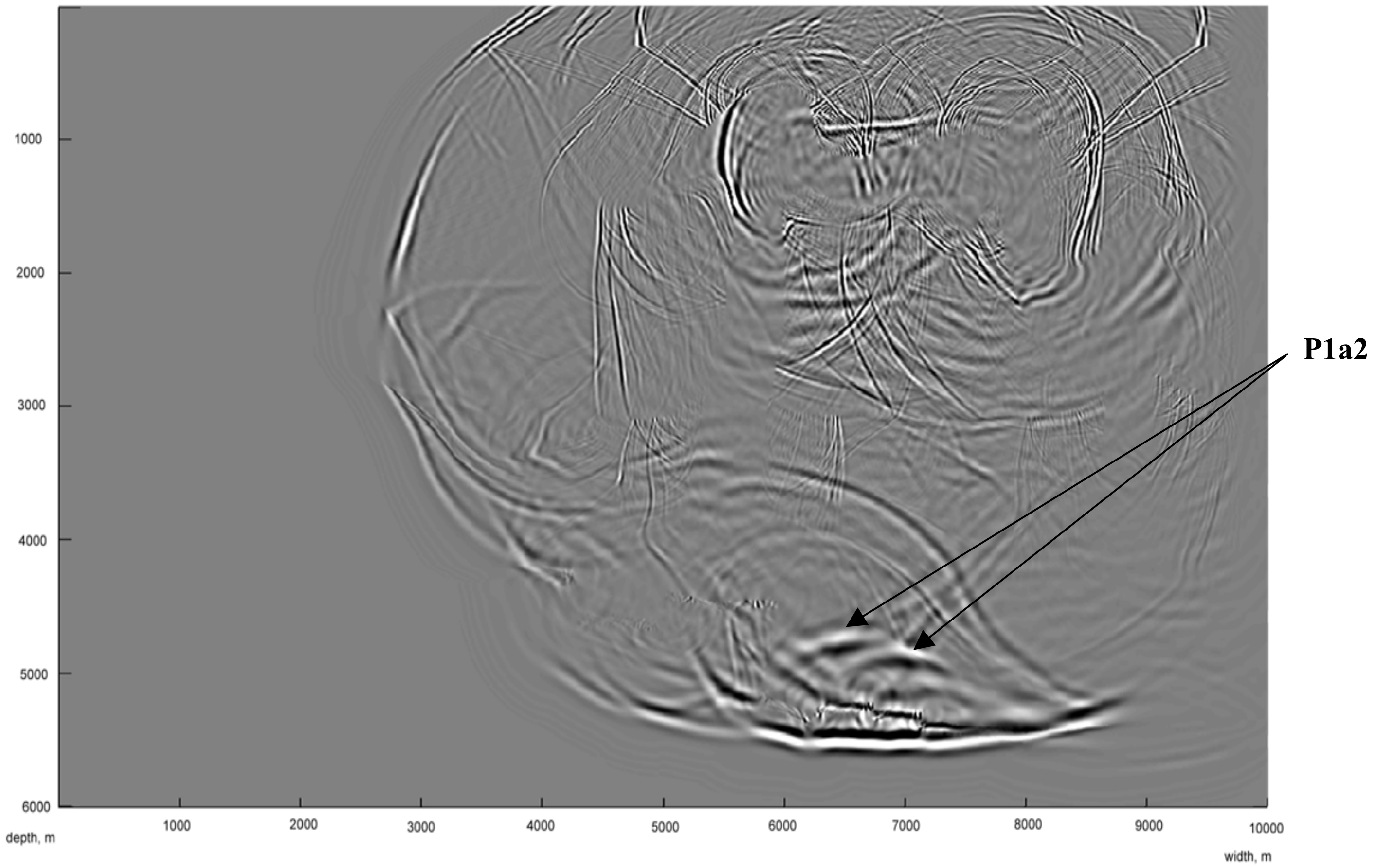

Figure 48. Snapshot at timestep 85 without free surface multiples shows clearly the target P and S reflections.

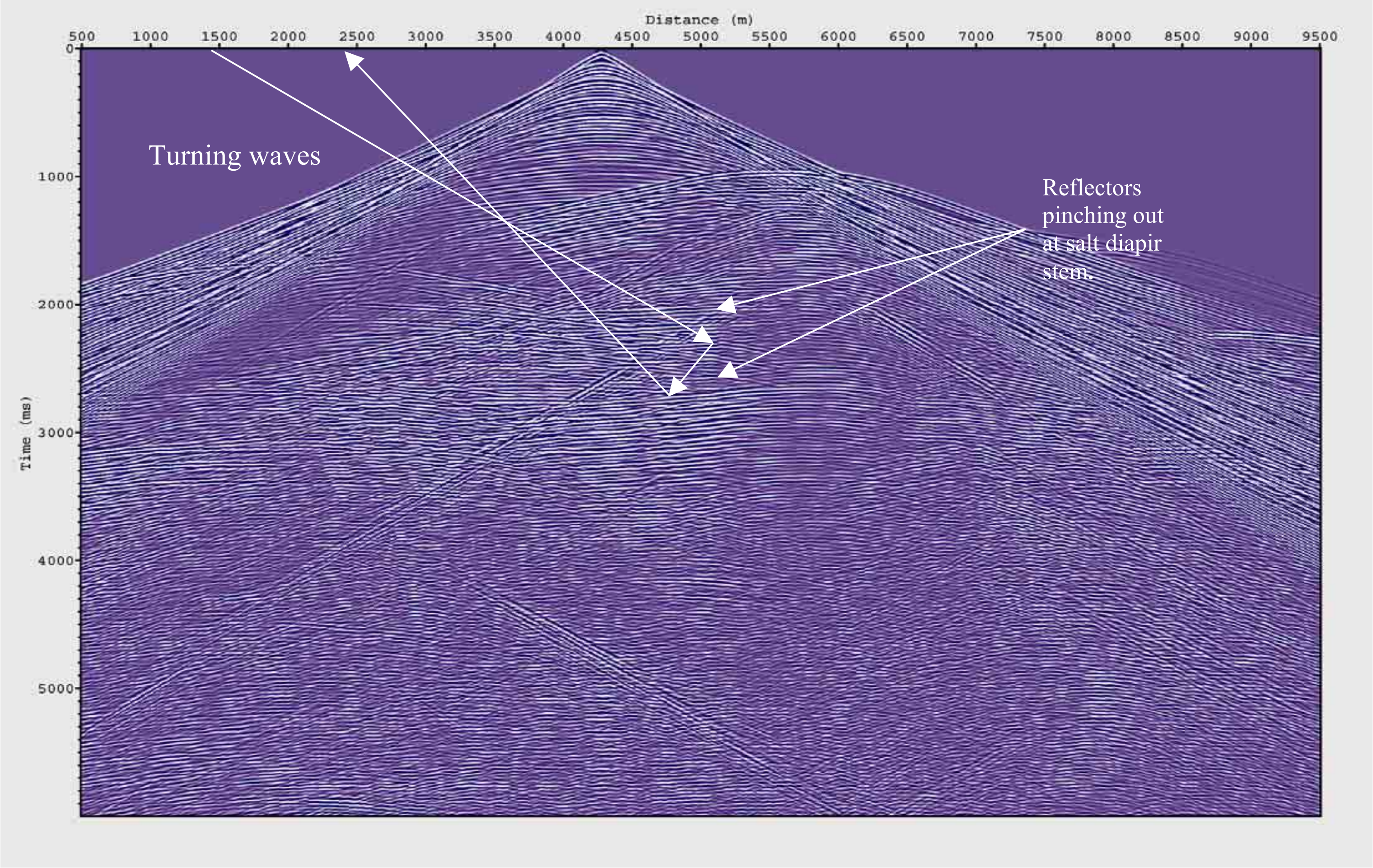

Figure 49. Shot 121, vertical component of velocity. Multiples and S-waves are not suppressed. Shooting near salt allows us to see reflectors pinching out at the stem of a salt diapir.

affiliated reservoirs with P-waves. A wide aperture is very important for imaging North Caspian salts because of the substantial depths.

Multicomponent waves

Our experiment is for elastic wave propagation in area with complex salt structures, namely, halite domes and diapirs. In addition to complexity of structures, we also have very high velocity contrasts. This situation is very prone to generation of S-waves, which are mainly a result of conversion from P-waves. (S-wave in our 2D case means SV-wave.) The conversion takes place when an incident P-wave falls onto a reflector at an angle greater than the critical angle of P-waves, and when the velocity contrast between two formations is high. Let us consider our situation. First, we have an abundance of steep salt dome and diapir slopes. That conditions the emergence of S-waves, because even in cases when an incident wave falls vertically onto steep slopes of salt, the angle between salt surface and an incident wave is well beyond critical angle of P-waves. Of course, the complexity of salt structures is going to contribute to the chaos of ray paths. Second, the velocity contrast range from 2160m/s (top halites/K2 clastics) to 3200m/s (anhydrites/P1a2 clastics). It is also a good condition for having P-waves converted into transmitted and reflected S-waves.

The degree to which P-wave energy turns into S-wave energy is evident from the shot gathers where there is a white cloud instead of a picture of a salt mass by P-waves. On the same gathers we see S-waves freely traveling through salt. Figures 50-53 illustrate an absence of P-waves and a presence of PS-type converted waves in salt.

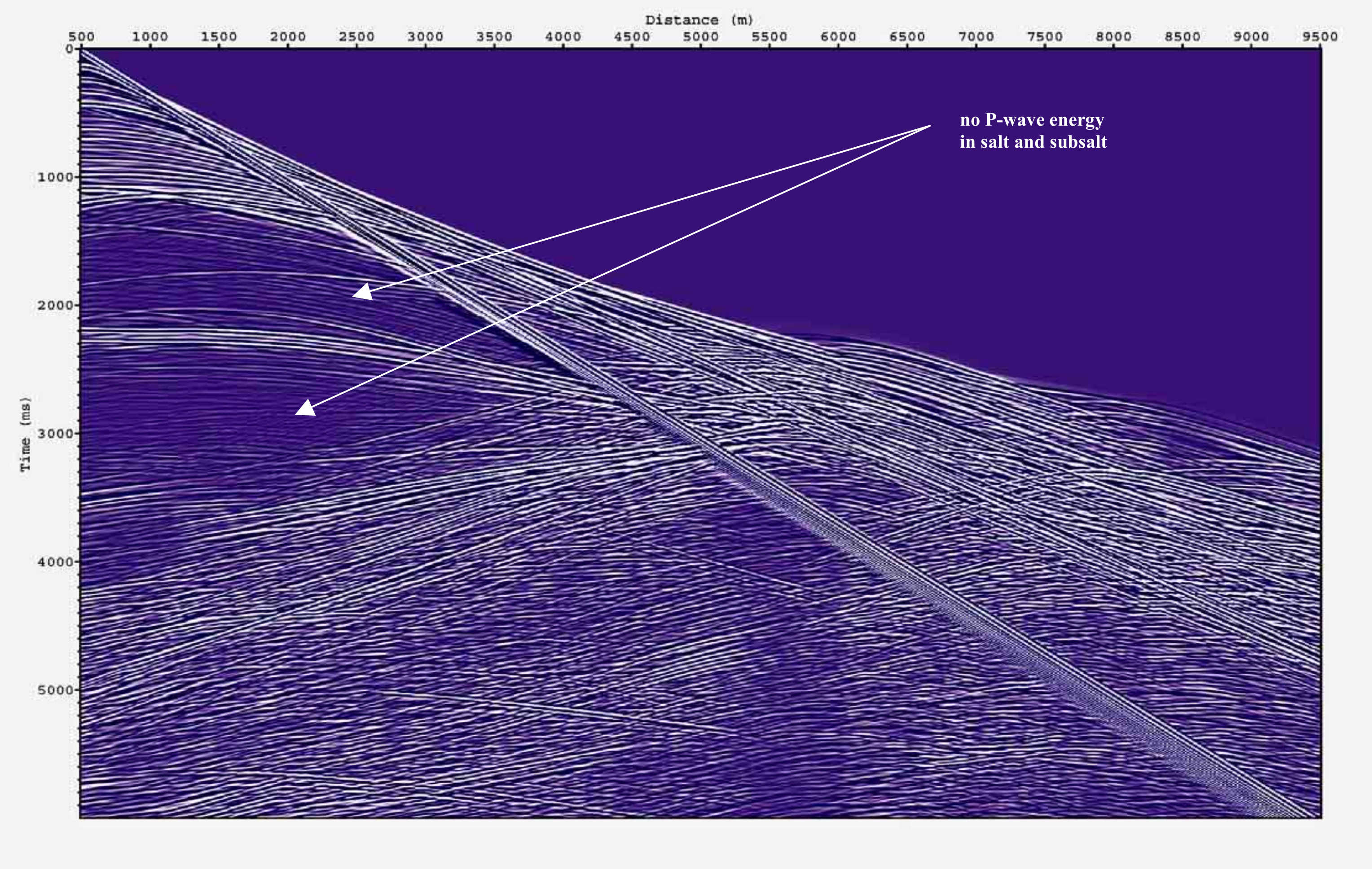

Figure 50. Shot 001, pressure. Exp. Gain, AGC=90, absorbing top boundary. Vs=0. P-wave amplitudes in salt are severely diminished.

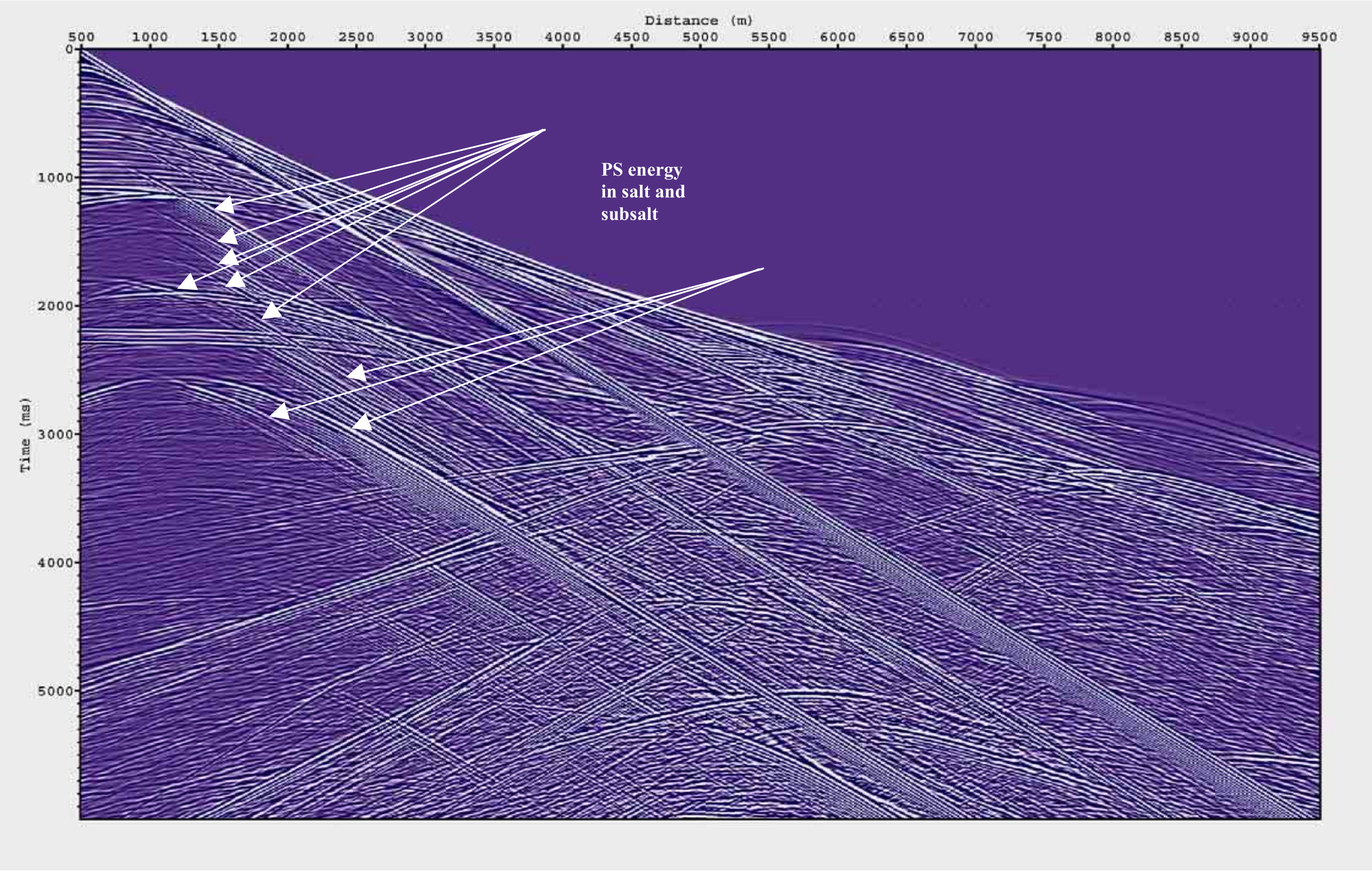

Figure 51. Shot 001, pressure. Exp. Gain, AGC=90, absorbing top boundary. S-wave amplitudes are not diminished in salt as P-wave amplitudes.

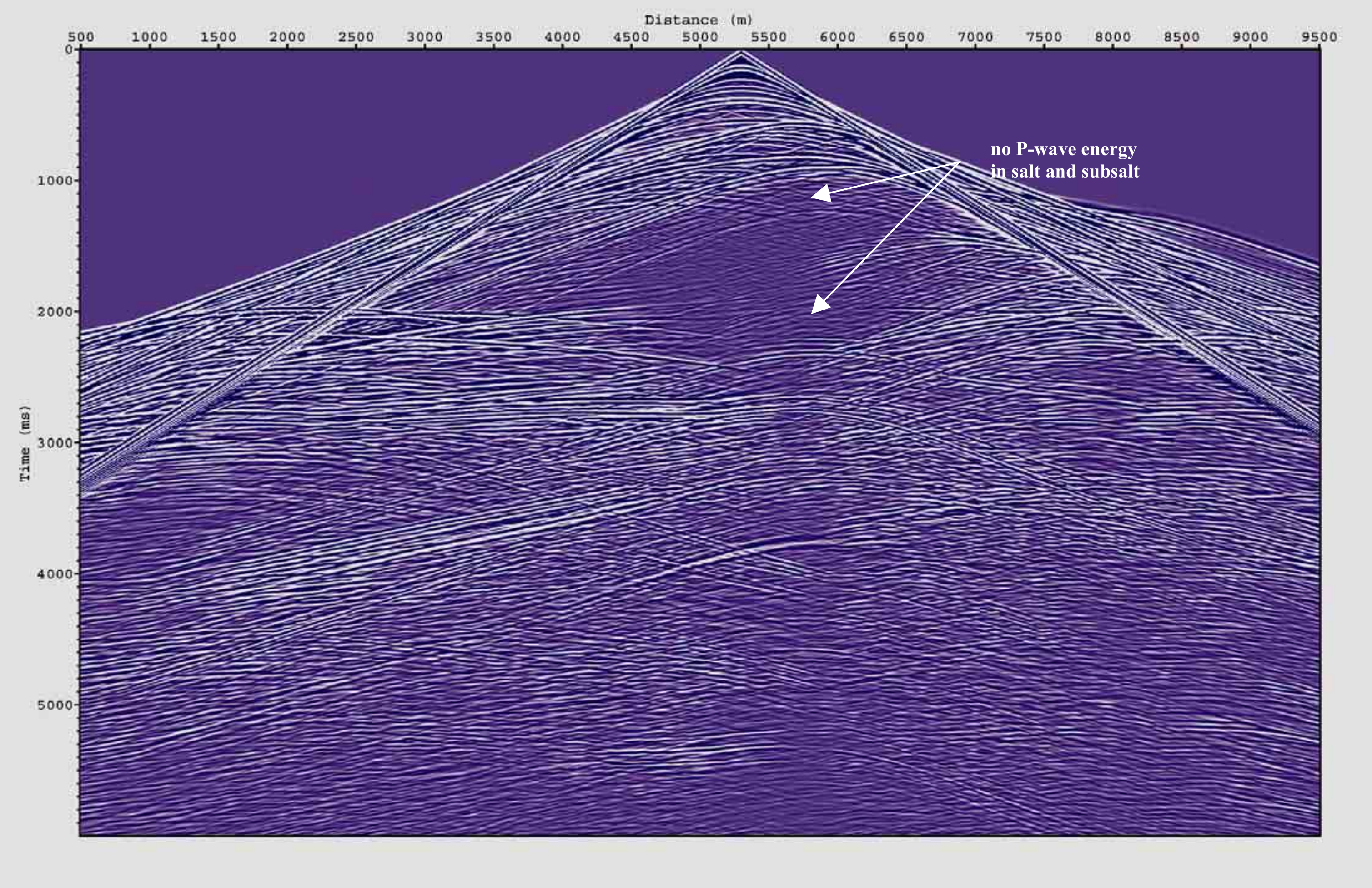

Figure 52. Shot 161, pressure. Exp. Gain, AGC=90, absorbing top boundary.Vs=0 . Very low amplitudes of P-wave in salt diapir.

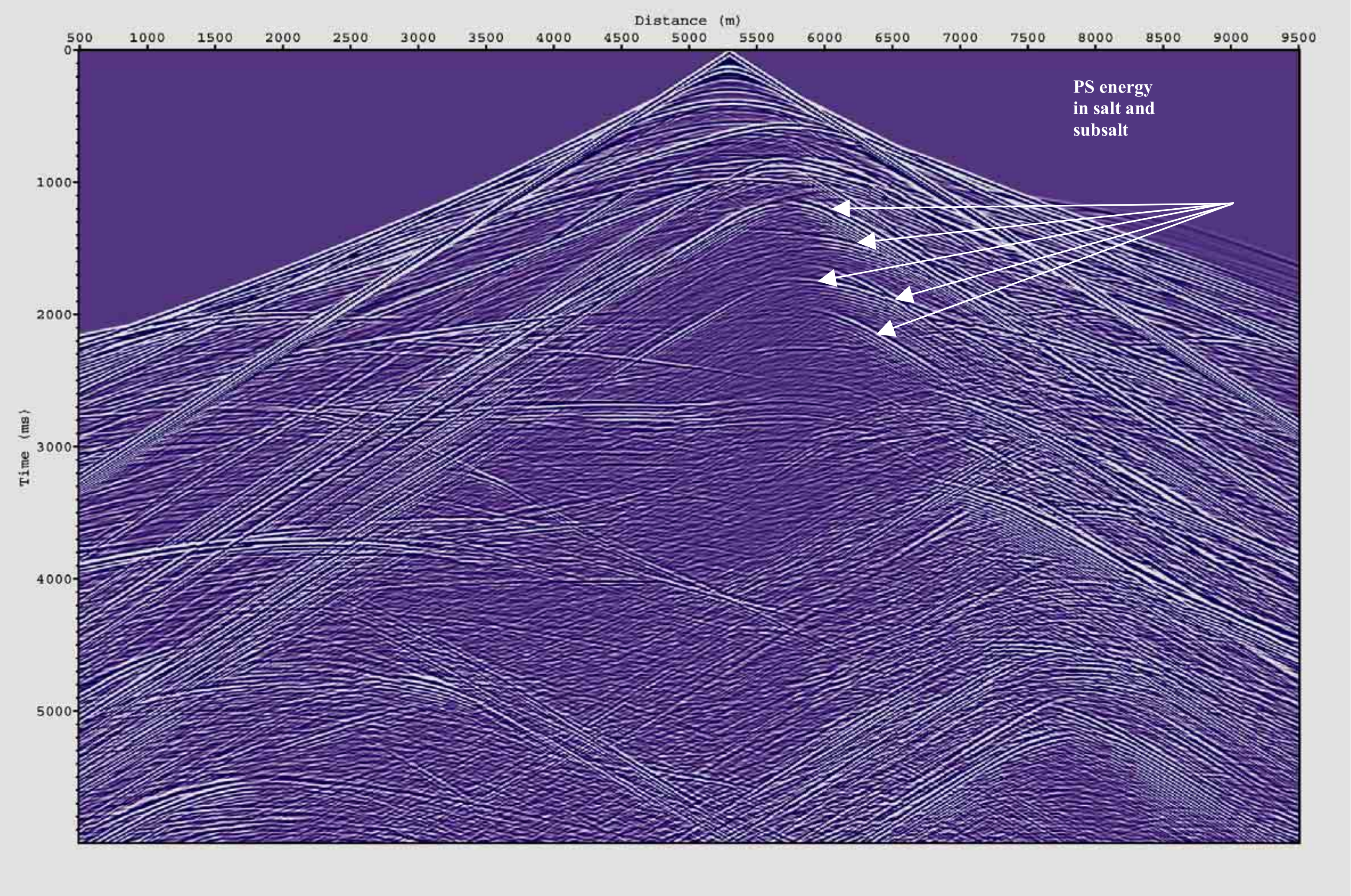

Figure 53. Shot 161, pressure. Exp. Gain, AGC=90, absorbing top. S-waves are abundant in salt.

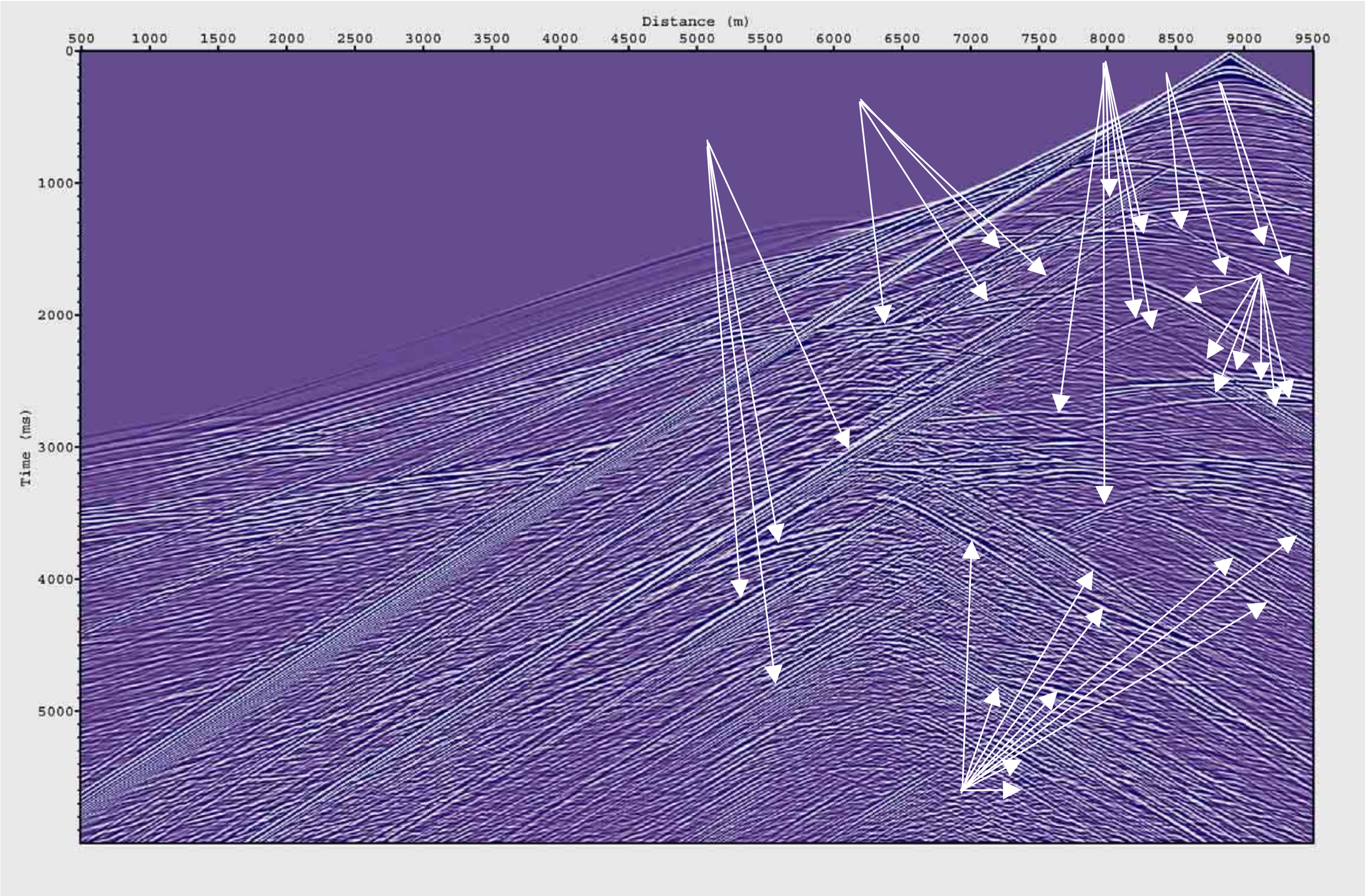

Figure 54. Shot 041, vertical component of velocity. Exp. Gain, AGC=90. S waves generated by salt diapirs.

Upon a general look at our shot gathers, we see that converted waves (PS, PSSP, PSPP, PPSP, etc.) are numerous and dominate our data (Figure 54). As we found by running different experiments, principally salts generate converted waves in our model. Figures 55-60 show the reflected P and S waves from the top of salts. The steeper slopes of salt flanks and the more vertical diapir stems are the more abundant are S-waves on shot gathers.

There is also evidence that converted waves (PSSP, etc.) easily can be mistaken for primary waves (Figure 61) and considered “bright spots” by interpreters.

Snapshots confirm the role of shear waves in delineating the salt bodies. Again, as we see on snapshot (Figure 62), converted waves delineate slopes and sides of salt diapirs very well, while P-waves alone are vague (Figure 63). In addition, shear waves have much better resolution because of their short wavelength.

While PS converted waves are better for steep slopes and stems of salt diapirs, it is impossible to image subsalt clastics and carbonates with them, because when S-waves go back up to the surface they go through two or three more salt bodies which converts them back to P-waves and dissipates them. On the snapshot in the previous section (Figures 36-38) we see that only the P-wave from top subsalt clastics travels back to the surface.

Looking at shot gathers, we conclude that our assumptions that hydrophone records always only P-wave, vertical geophone records mostly P-wave are wrong. Our hydrophone data has S-waves (Figures 28-35, 39-46, etc.) and vertical geophone data has S-waves too. (Figure 54).

S-waves on hydrophone data are converted waves of PSSP, PSPP, PPSP-type reflected from steep salt flanks. The first and last P-wave conversions take place as the S-wave approaches very shallow hydrophone in the water.

S-waves on the vertical geophone appear because converted PS reflection from the very steep slope of salt is approaching the geophone when the wavefront of the PS wave is still almost vertical. We can see that happening on the snapshot (Figure 64). Therefore we can conclude that the vertical component of particle velocity is important in imaging steep salt flanks, because it contains mostly the vertical component of rotational movement of particles, i.e. the S-wave component.

Therefore, here we can recommend for processing flow:

1. Identify and separate S-wave events (PSSP, PSPP, PPSP, etc) on hydrophone gathers, separate them from P-waves, and carry out PS-NMO and PS-prestack depth migration on S-waves to image steep salt flanks.
2. Identify and separate S-waves from vertical geophone data, move out, and migrate it as an S-wave reflected from very steep salt flank.

The concept and mathematical description of decomposition of a seismic wavefield into P and S waves developed in the book “An Introduction to Petroleum Seismology” (Ikelle and Amundsen, 2004).

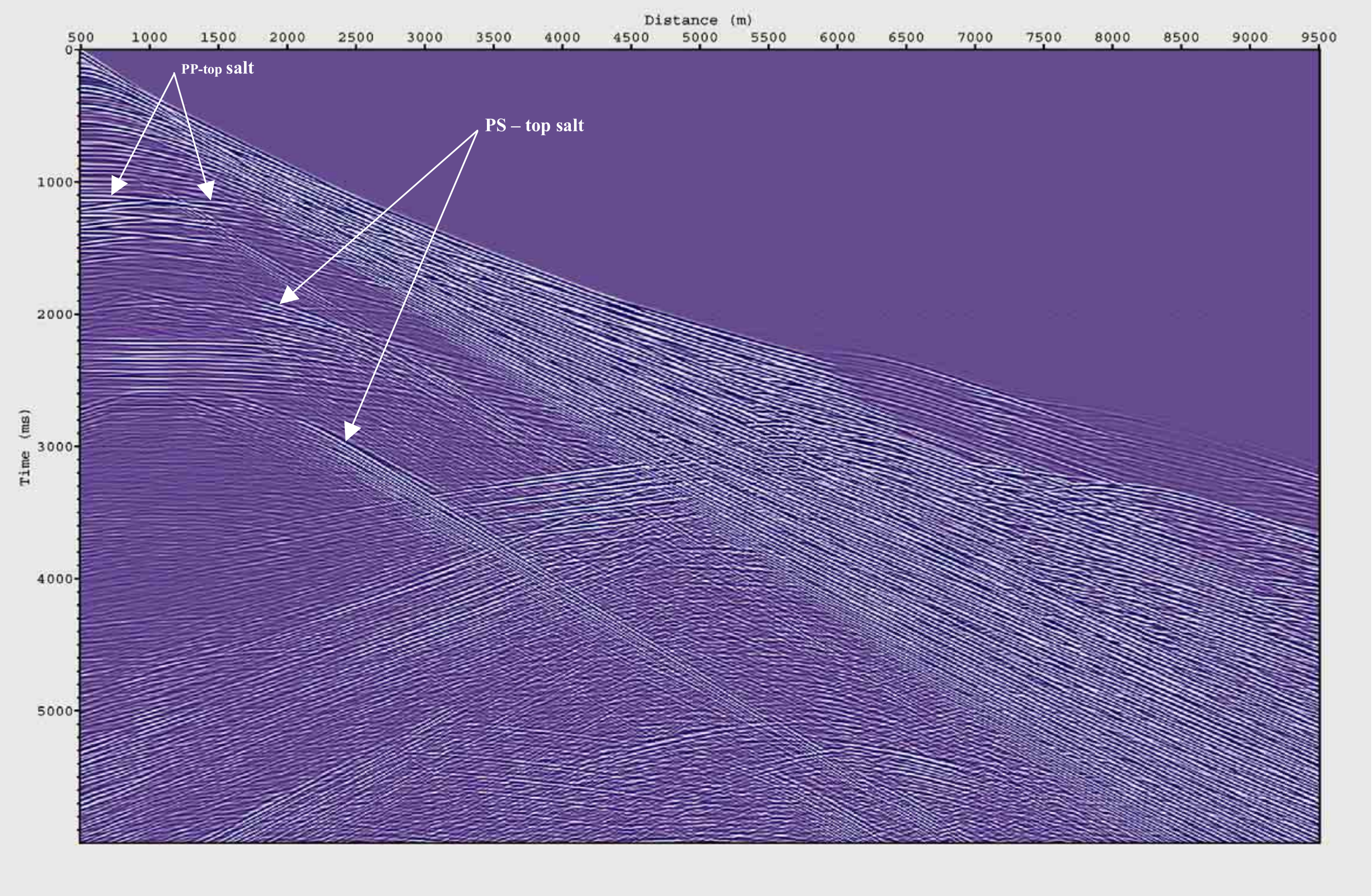

Figure 55. Shot 001, pressure. Exp. Gain, AGC=90. Top of salt P and S reflections.

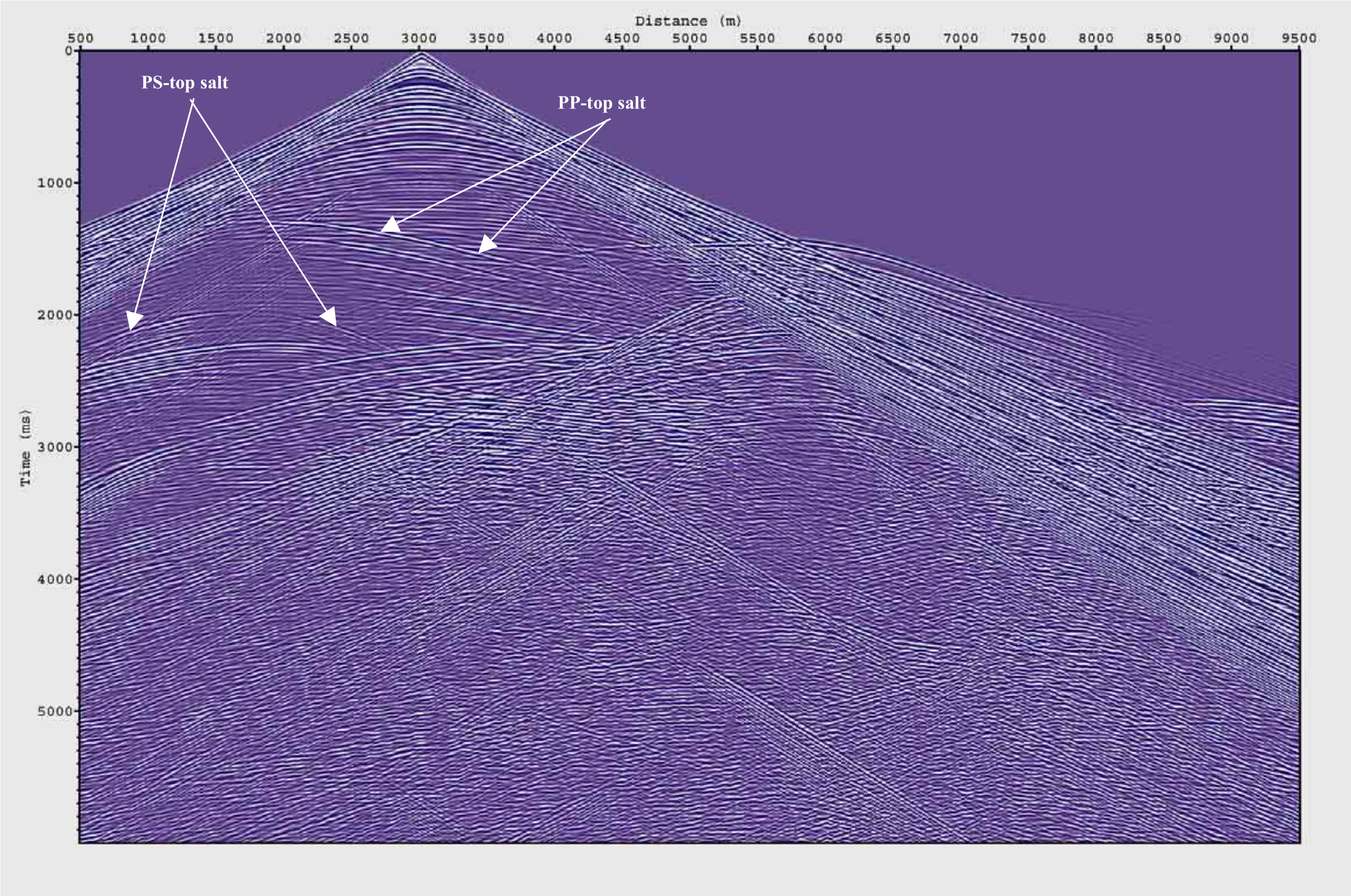

Figure 56. Shot 081, pressure. Exp. Gain, AGC=90. Top of salt P and S reflections.

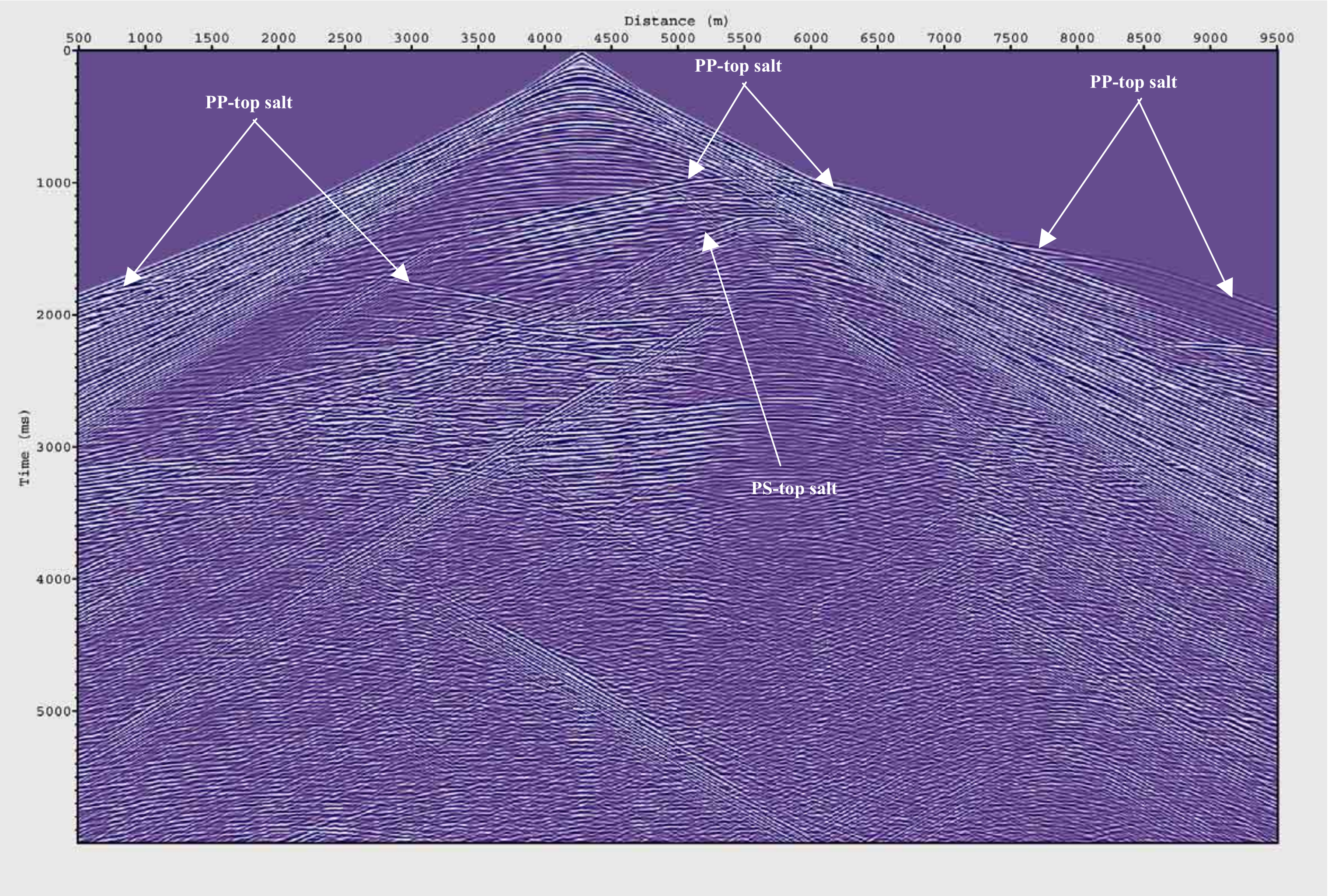

Figure 57. Shot 121, pressure. Exp. Gain, AGC=90. Top of salt P and S reflections.

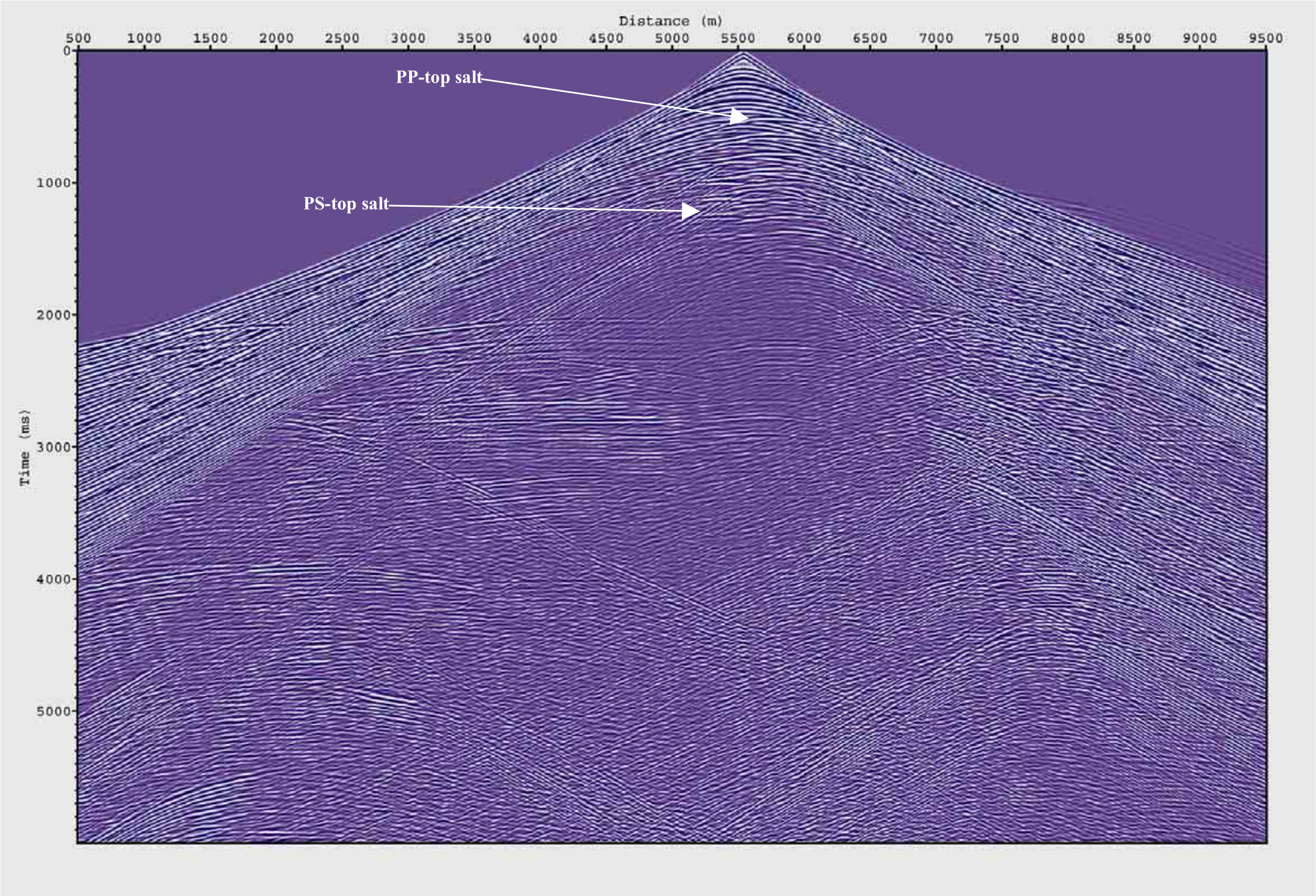

Figure 58. Shot 161, pressure. Exp. Gain, AGC=90. Top of salt P and S reflections.

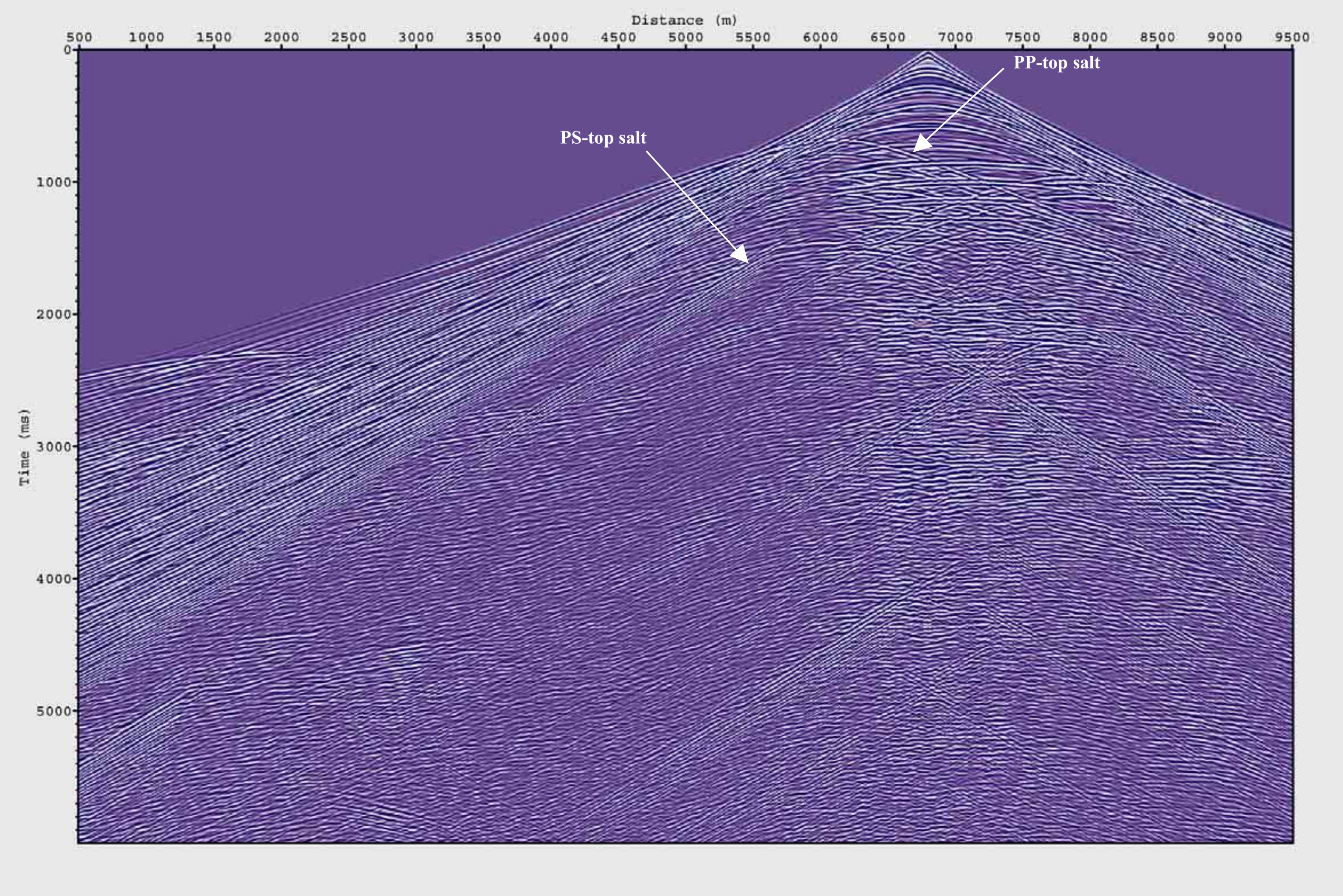

Figure 59. Shot 201, pressure. Exp. Gain, AGC=90. P and S reflections from top of salt.

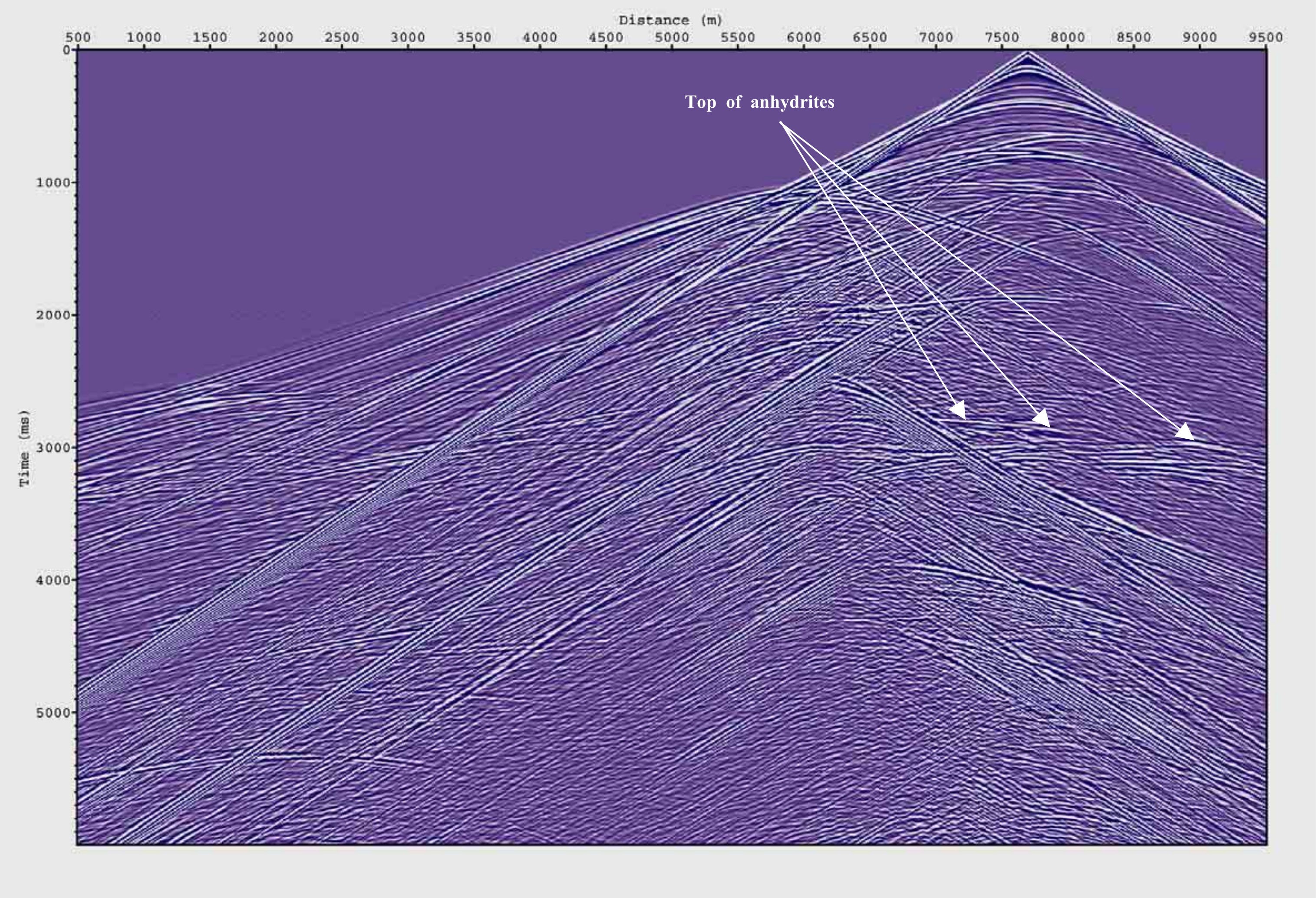

Figure 60. Shot 241, pressure. Exp. Gain, AGC=90, absorbing top boundary. Top of anhydrites P reflection.

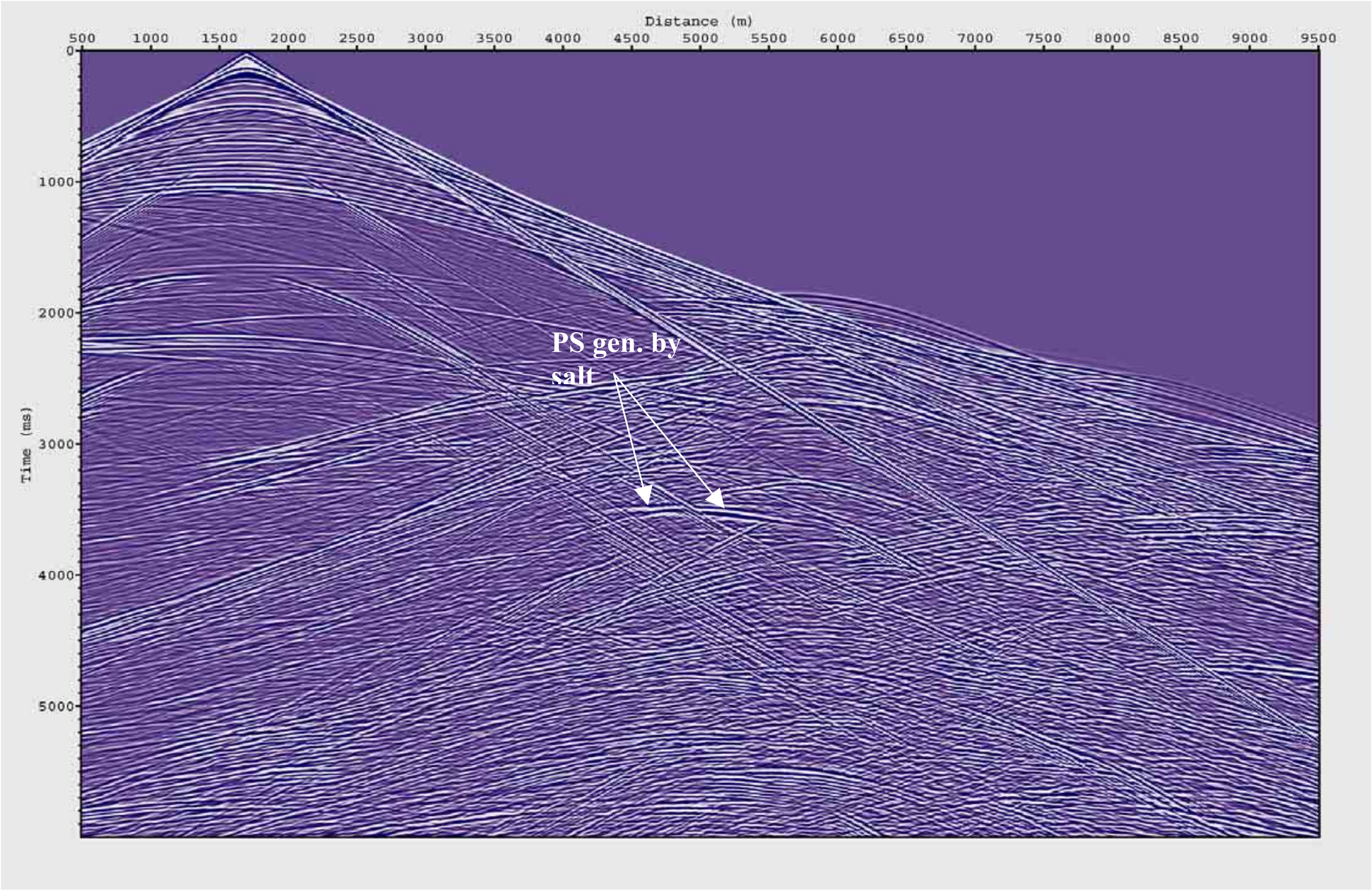

Figure 61. Shot 041, vertical velocity component. Exp. Gain, AGC=90. Example of an S-wave generated by salt, where it can be mistaken for a P-wave bright spot.

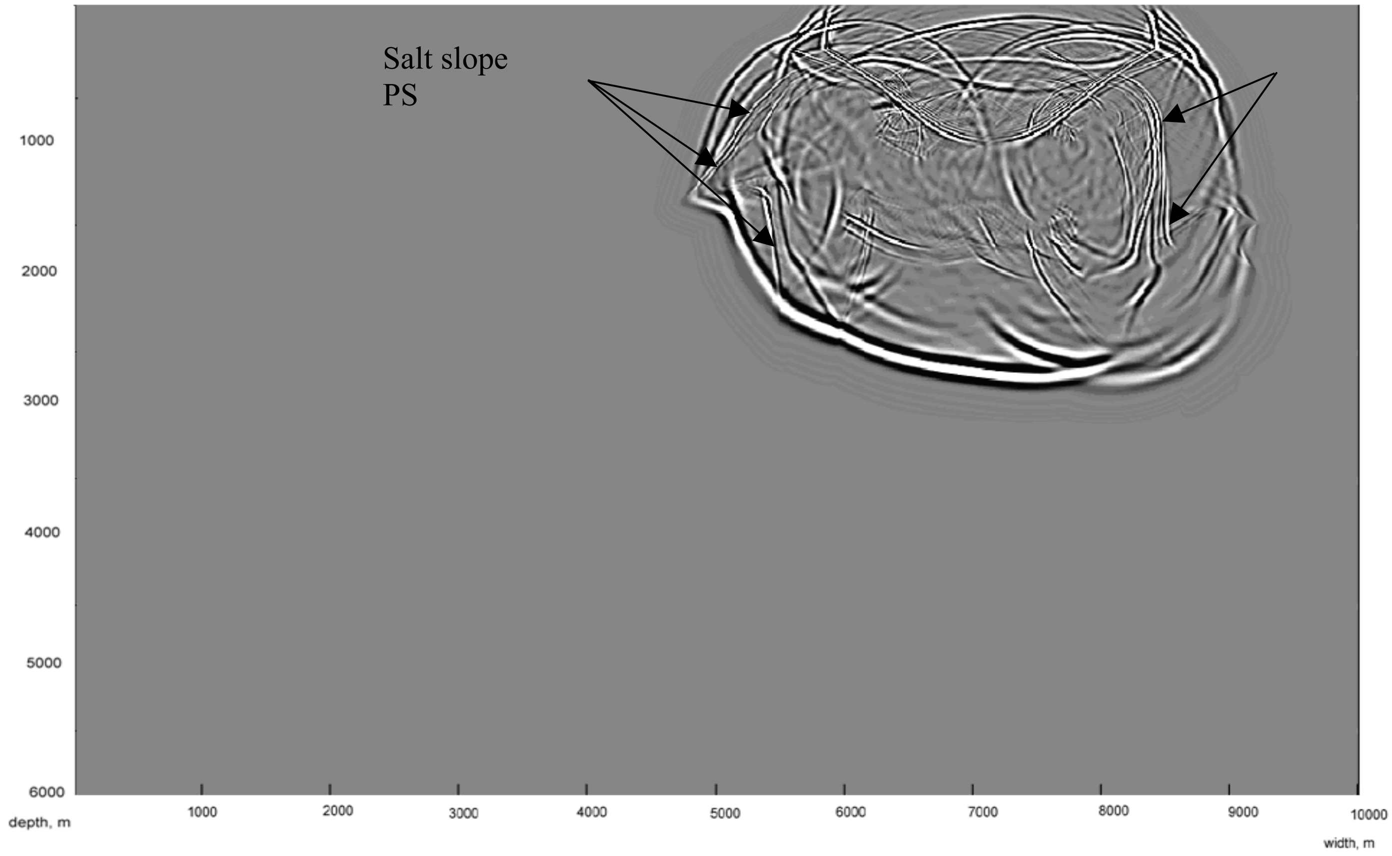

Figure 62. Snapshot showing clear delineation of steep salt diapir slopes by shear waves.

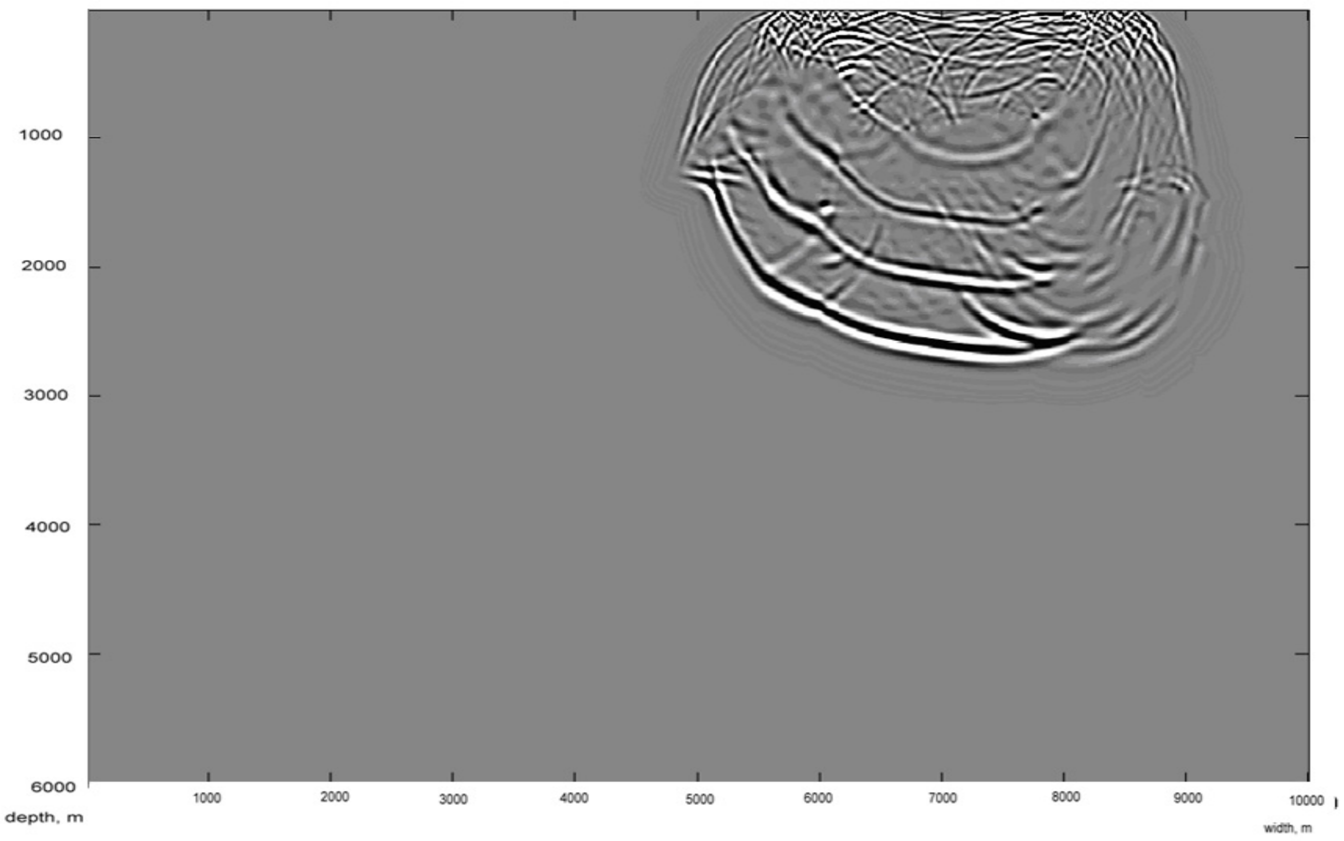

Figure 63. Snapshot with P waves only, which has no reflections from salt diapir steep slopes.

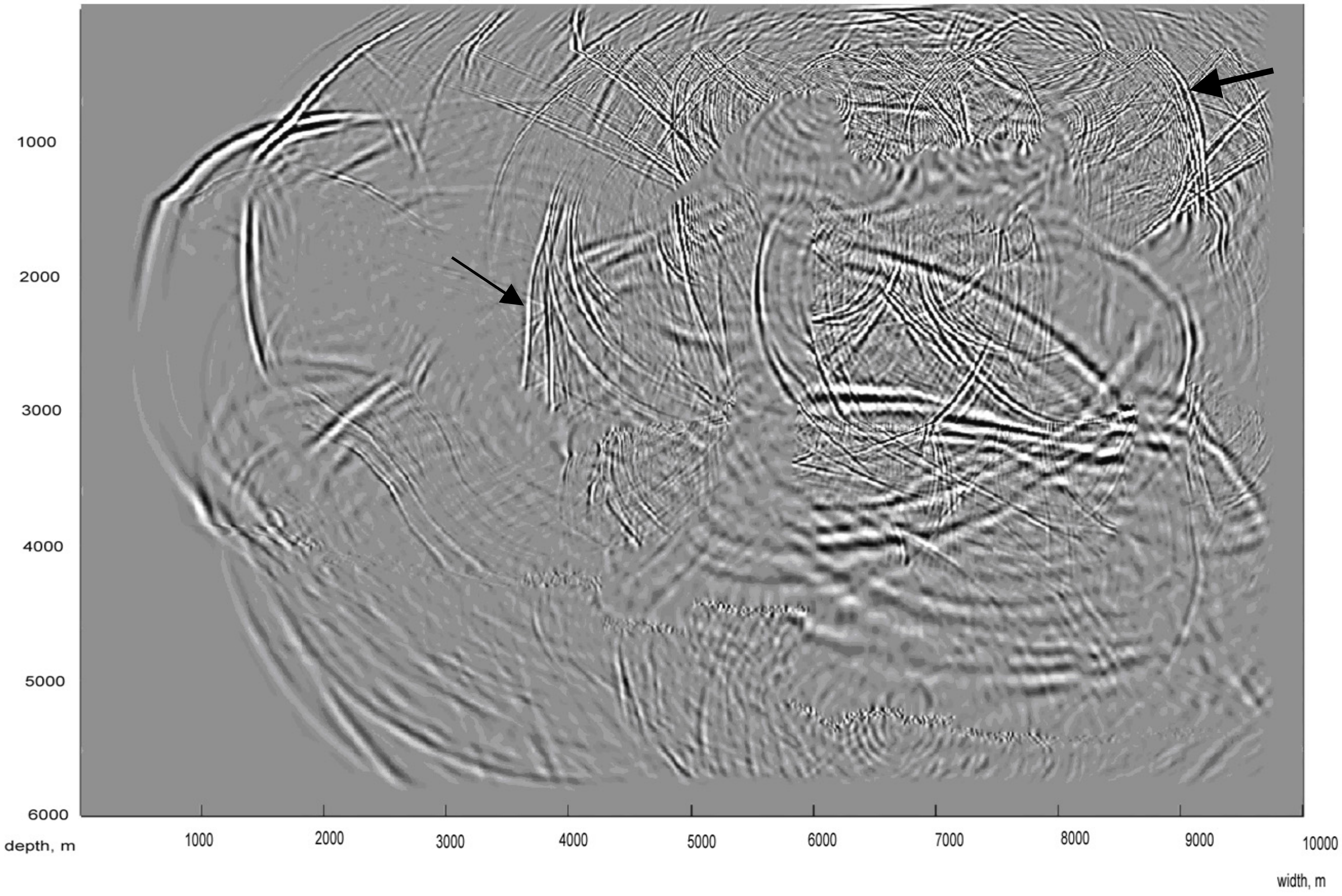

Figure 64. Snapshot of vertical geophone data, shot 222, absorbing top. Near vertical wavefront of the S-wave from a near vertical salt stem is approaching the geophone and being recorded as a vertical component of velocity.

CHAPTER V

CONCLUSIONS

Using 2D elastic finite-difference modeling we tried to find answers to the following questions affecting our ability to seismically image NCB subsalt, suprasalt, and nearsalt reservoirs:

- Can we see subsalt clastic and carbonate (reef) reservoirs through thick overburden? Can we image carbonates (reef) that are located under salt domes and diapirs, which blanket them from seismic energy?
- How do halites and anhydrites with their complex structure affect our ability to image target reflectors?
- Do the shallow waters (3-15 m) of the Caspian Sea shelf affect our ability to image reservoirs?

For the subsalt carbonate reservoir, we found that we can see its top everywhere, except when there is a thick (about 1000 m) anhydrite deposit and a tall halite diapir over the anhydrites, the energy of the seismic wave depletes before reaching subsalt carbonates. Anhydrites so dramatically increase wavelength that we cannot image top carbonates under anhydrites, we can only image top P1a2 clastics overlying carbonates. But that is close enough to the top carbonates. P and S reflections, refractions etc., produced by salt diapirs on the right side of our model, greatly interfere with reflection from top P1a2 clastics on top of the carbonate reservoir, whereas clastics and carbonates are clearly visible under the salt dome. Thus salt domes have less deteriorating impact on subsalt imaging than salt diapirs.

So we can conclude that seismic waves have enough energy to bring us the information about subsurface targets through the thick overburden in the NCB.

Halites and anhydrites present the biggest imaging challenge in the exploration for oil in the North Caspian Basin. Halite and anhydrite salts of the NCB mean complex structures, steep slopes, high velocities, and high velocity contrast with surrounding clastics and underlying reefs and carbonates. They create unpredictable seismic raypaths, and *converted*, diffracted, refracted, and reflected waves. They canalize and disperse seismic waves. All this impacts NMO, velocity analysis, and migration.

We found that the S-wave is a very important agent in delineating salt domes and diapirs.

Let us first consider the case of exploding the source directly over a salt diapir or dome. In this case the P-wave falls vertically onto a steeply dipping salt surface. Thus, the dip of the salt slope is the defining parameter in the rate of conversion of the incident P-waves into reflected S-waves, rather than the critical angle of the P-waves. (Of course, the impedance contrast is contributing to the partitioning of energy at the interfaces.) Thus, we can image only salt surfaces with dips *more* than the critical angle of the P-waves and *less* than the critical angle for the S-waves, i.e. in the window between two critical angles. In this case the S-wave will be recorded with the horizontal as well as the vertical component of particle velocity.

In the same case of a source exploding directly over a salt diapir, salt slopes with dips beyond the critical angle for S-waves (diapir stems, for example) would be possible to image too. In this case, we would use the fact that salt acts as a refracting lens for an

S-wave, which transmits from salt into surrounding clastics. That wave has the wavefront replicating the surface of a diapir stem. It propagates in the horizontal direction. But the velocity gradient eventually helps it to approach geophones. This way this S-wave will be recorded mostly on the vertical component of the geophone. For fully recording all the vertical wavefronts we would need a very long recording line.

After we have all records, the only way to image steep salt structures would be by, first, extracting S wave from all records – pressure, horizontal and vertical components of particle velocity, and, second, carrying out NMO and prestack depth migration for S-waves. The method for separating P and S-waves is developed by Dr. Ikelle (Ikelle and Amundsen, 2004).

Now let us consider the case of exploding the source away from top salt (wide aperture survey). P-waves would be able to approach diapir stems at angles less than critical. These waves would reflect off diapir stems as P-waves, hit the horizontal reflector near salt, reflect off that horizontal reflector, and record on a geophone or hydrophone. Thus the ray “returns” to the surface with information about the salt stem and about reflectors pinching out at the salt stem. The method of “turning waves” is developed by Dr. Ikelle (Ikelle, 2004). This is the way to image salt stems and affiliated reservoirs with P-waves. Wide aperture is very important for imaging North Caspian salts because of the substantial depths.

While the S-wave is very important for imaging steep salt, it was found that the P-wave is the best for imaging subsalt carbonates. Therefore, we would say, that the S-wave can help us to better locate suprasalt and nearsalt reservoirs and to safely drill well, while the P-wave can help us in imaging subsalt reservoirs.

The shallow waters (3-15 m) of the Caspian Sea shelf cause free-surface peg-leg multiples, guided waves, and require special acquisition techniques. As we have shown in the results chapter, it is very important to remove free-surface peg-leg multiples and guided waves in order to be able to image subsalt target reflectors. The method of hydrophone and vertical geophone data summation to remove water layer reverberations and receiver ghosts is also developed by Dr. Ikelle (Ikelle, 1999b).

Imaging algorithms need all three components: pressure, vertical and horizontal components of particle velocities. This demonstrates us the importance of using the Ocean Bottom Seismic when exploring North Caspian Basin offshore.

Our resulting dataset is composed of 314 shots. Each shot is recorded by 601 dual sensors, i.e. a geophone and a hydrophone. The hydrophone produces pressure data, the geophone produces two traces: vertical and horizontal component of media displacement velocity. The acquisition technique therefore is 3-component Ocean Bottom Seismic (3C OBS). Recording time is 6 seconds.

The synthetic dataset is converted into SEGY format and will be available on the website of CASP consortium (CASP Project, 2004) for anyone who would like to test their Prestack Migration algorithms.

This work demonstrated to us the tremendous value of 2D elastic finite-difference modeling of the propagation of seismic waves.

Future elastic modeling efforts shall use a 3D, finely gridded, large, oil and gas saturated, overpressured, anisotropic, fractured model for the subsalt reef reservoir.

REFERENCES

Baiuk, E. I. and Fomin, A. A., 1989, Deformational and reservoir properties of carbonate subsalt deposits of Tengiz oilfield: Geology of Oil and Gas, **5**, 30-35

Barde, J-P., Gralla, P., Harwijanto, J., and Marsky, J., 2002, Exploration at the eastern edge of the Pricaspian basin: Impact of data integration on upper Permian and Triassic prospectivity: AAPG Bulletin, **86**, 399-415

CASP Project, 2004, Center of Automated Seismic Processing at Texas A&M University. Available at http://casp.tamu.edu

Crain, E. R., 2004, Crain's Petrophysical Handbook. Available at http://www.spec2000.net/lcmain.htm

Dvorkin, J., Mavko, G., and Nur, A., 1999, Overpressure detection from compressional- and shear-wave data: Geophysical Research Letters, **26**, 3417-3420.

Fomin, A. A., Baiuk E, I., and Dyaur, N. I., 1992, Physical properties of subsalt rocks at high temperatures and pressures: Nedra, 101-116 (in Russian).

Graves, R. W., 1996, Simulating seismic wave propagation in 3d elastic media using staggered-grid finite differences: Bulletin of Seismological Society of America, **86**, 1091-1106

Ikelle, L. T., 1999a, Combining two seismic experiments to attenuate free-surface multiples in OBC data: Geophysical Prospecting, **47**, 179-193

Ikelle, L. T., 1999b, Using even terms of the scattering series for deghosting and multiple attenuation of ocean-bottom cable data: Geophysics, **64**, 579-592

Ikelle, L. T., and Amundsen, L., 2004, An Introduction to Petroleum Seismology: SEG Publishing, publication in preparation

Ikelle, L. T., Jungki M., and Spears, H., 2003, Multi-shooting method for simulating seismic surveys: Application to 3D finite-difference modeling: Report of Consortium for Automatic Seismic Processing, vol 1, Texas A&M University, Available at http://casp.tamu.ed

Kolosova, R. I., 1982, Velocities of salt bearing deposits of Pricaspian depression: Bulletin of Academy of Sciences of Kazakh SSR. Geological series, **1**, 65-68 (in Russian).

Kononkov. V. F., Bobynin, B. V., Butazov, V. V., Zhigalin, A. Y., Volgina, A. I., Pavlov, A. S., and Kozak, O. K., 1978, Study of rock density of the section of Pricaspian Depression by means of gravity logging: Oil and Gas Geology and Geophysics, **10**, 28-32 (in Russian).

Kunin, N. Y., Gatsolaeva, S. S., and Kosov, A. A., 1977, Zoning of physical properties of clastic rocks of the subsalt sediments of Pricaspian depression: Oil and Gas Geology, **1**, 7-10

Li, Y. and Downton, J., 2003, Recent applications of AVO to carbonate reservoirs in the Western Canadian Sedimentary Basin: The Leading Edge, **7,** 670-674

NASA, 2004, Visible Earth. Available at http://visibleearth.nasa.gov/

Pavlov, N. D., Salov, Y. A., Gogonenkov, G. N., Akopov, Y. I., Tolstyh, A. A., and Denisiuk, R. S., 1988, Geological-geophysical model of Tengiz oil-bearing paleoatoll by seismostratigraphic data: Bulletin of Academy of Sciences of USSR. Geological series, **10**, 137-150. (in Russian).

Shebaldin, V. P., Selenkov, V. N., and Akimova, A. B., 1988, Geological structure of Tengiz oil field by materials of geophysical investigations: Geology of Oil and Gas, **12**, 12-16 (in Russian).

Stoughton, D., Stefani, J., and Michell, S., 2001, 2-D elastic model for wavefield investigations of subsalt objectives, deep water Gulf of Mexico: 71st Ann. Internat. Mtg., Soc. Expl. Geophys., Expanded Abstracts, 1269–1272.

US DOE EIA, 2002, Caspian Sea Region Oil and Natural Gas Reserves. Available at http://www.eia.doe.gov

U.S.- Kazakhstan Business Association, 2004, About Kazakhstan. Available at http://uskba.net

UT Libraries, 2004, Commonwealth of Independent States. Available at http://www.lib.texas.edu/maps/

Volarovitch, M. P. (ed), 1988, Physical properties of minerals and rocks with high thermodynamic parameters: Nedra, 1-250 (in Russian).

Volozh, Y. A., Votsalevsky, E. S., Zhivoderov, A. B., Nurbaev, B. O., and Pilifosov, V. M., 1989, Problems of oil and gas prospectivity of supra-salt strata of Pricaspian depression: Bulletin of Academy of sciences of Kazakh SSR, Geological series, 4, 3-15.

Volozh, Y., Talbot, C., and Ismail-Zadeh, A., 2003, Salt structures and hydrocarbons in the Pricaspian basin: AAPG Bulletin, **87**, 313-334.

Zholtaev, G. Z., 1996, Geodynamic model of Pricaspian Syneclize in Paleozoic: Kazakhstan Geology, **5**, 41-55 (in Russian).

Zholtaev, G. Z., 1989, Structure of Pre-Kungurian strata of Pricaspian syneclize: Soviet Geology, **5**, 74-83 (in Russian).

VITA

Zhanar Alpysbaevna Bailey was born in Almaty, Kazakh S.S.R., U.S.S.R. She graduated from Physical-Mathematical Specialized School at Novosibirsk State University. She received the Diploma in geophysics from Kazakh National Technical University. She worked for Schlumberger GeoQuest and Kaznedra in Kazakhstan. She was awarded an International Petroleum Geosciences Scholarship from the American Geological Institute and a group of USA oil companies for non-degree studies in Texas. Following work on the non-degree program, she entered the M.S. program in geophysics at Texas A&M University, working at Exxon, the Ocean Drilling Program, TAMU, Schlumberger Geco-Prackla, and Occidental Oil and Gas. Her current address: 401 Stasney St., Apt 224, College Station, TX, 77840, USA. Email: zhanar_bailey@yahoo.com.